Äspö Hard Rock Laboratory

In-situ failure test in the research tunnel at Olkiluoto

Jorma Autio

Erik Johansson

Timo Kirkkomäki

Saanio & Reikkola Consulting Engineers

Matti Hakala

Gridpoint Finland OY

Esa Heikkilä

Helsinki University

March 2000

SKB

**Äspö Hard Rock
Laboratory**

Äspö Hard Rock Laboratory

In-situ failure test in the research tunnel at Olkiluoto

Jorma Autio

Erik Johansson

Timo Kirkkomäki

Saanio & Reikkola Consulting Engineers

Matti Hakala

Gridpoint Finland OY

Esa Heikkilä

Helsinki University

March 2000

SAMMANFATTNING

Ett brottstest, som är lämpligt att genomföra i Forskningstunneln i Olkiluoto, har planerats för att studera brott i berg in situ. Syftena med brottstestet är att utvärdera användbarheten av numeriska modellkoder och metoder för att studera bergbrott och sammanhängande sprickpropagering liksom att utveckla en ny teknik för att bestämma bergets hållfasthet in situ. Syftet med här redovisad studie var att genomföra en preliminär planering av brottstetstet, utvärdera testets tekniska möjlighet och att lämna underlag till ytterligare numerisk modellering av testet. Utformningen av testet rapporteras och preliminära modellresultat redovisas. Underlaget till ytterligare modellering inkluderar bergets egenskaper, sprickpropagering i berg, in situ spänning och utveckling av teknik för användning av expanderande material för att skapa det artificiella spänningsfältet. Studien visade att mekaniska egenskaper såsom hållfasthet hos gnejsisk tonalit, den huvudsakliga bergarten i forskningstunneln, beror starkt på orienteringen av skiffrigheten. Brottstestet in situ visades vara tekniskt möjligt och ett tillräckligt högt artificiellt spänningsfält för att skapa brott kan åstadkommas med hjälp av ett lämpligt expanderande materia och lämplig design.

ABSTRACT

An failure test suitable for execution in the Research Tunnel at Olkiluoto has been planned to study the failure of rock in-situ. The objectives of the in-situ failure test is to assess the applicability of numerical modelling codes and methods to the study of rock failure and associated crack propagation and to develop a novel technique to be used to determine the strength of rock in-situ. The objective of this study was to make a preliminary design of the failure test, assess the technical feasibility of the test and to give input information for further numerical modelling of the test. The design of the failure test is reported and results of preliminary modelling are given. The input information for future modelling includes a study of rock properties, fracture propagation in rock, in-situ stresses and the development of techniques for using the expanding agent to produce artificial stress field. The study showed that mechanical properties such as strength of gneissic tonalite, the main rock type in the Research Tunnel, depends highly on the orientation of schistocity. The in-situ failure test was shown to be technically feasible and a state of stress high enough to cause failure can be created artificially by using a proper expansive agent and design.

EXECUTIVE SUMMARY

Experience has shown that even if the conventional testing and modelling methods indicate that rock will fail, failure may well be a fairly localised phenomenon. It has been found in many cases, that even extensive failure and deformation of the underground space has a tendency to find a proper stable state and shape. Experience from deep underground facilities have proved that it is still feasible to construct undergound facilities even if rock failure occurs, given the condition that the deformation of rock reaches a stable state.

To be able to design stable underground spaces in environments where there is possibility for localized high stress concentrations we have to understand the mechanisms and processes that result in fracture generation, propagation and rock failure. The key factor in assessing the stability of an excavated opening in case of rock failure is to define whether the deformation of the rock can be controlled, and whether it reaches a stable state by seeking a favourable shape for the opening - something that has been observed on many occasions in the field - or whether it turns out to be the worst case, a violent rock burst. In all cases, fracturing of the rock must occur for the rock to be damaged and therefore a significant component of progressive failure is fracture propagation. Modelling of progressive failure should therefore include a mechanism for simulating fracture propagation.

The development of computers and associated modelling programs has led to a situation in which it is possible to model fracture propagation. The general objective of an in-situ failure test is to assess the applicability of numerical modelling codes and methods to the study of rock failure and associated crack propagation. One of the main tasks in an in-situ failure test is to carry out the modelling of rock failure by using both a conventional method of modelling without fracture propagation and a more sophisticated method capable of modelling the fracture propagation process. The observed failure patterns and the results obtained from the computer model are compared and evaluated. One prerequisite set has been that the computer programs used are currently available commercial products and that no development work on the actual program code shall be carried out.

Preliminary design of the failure test reported here is the first phase of the in-situ failure test which shall be followed by the modelling of the test by using a program which is capable of simulating fracture propagation and the actual in-situ field failure test. The objectives of the in-situ failure test are to assess the applicability of numerical modelling codes and methods to the study of rock failure and associated crack propagation and to develop a novel technique to be used to determine the strength of rock in-situ. The objective of this study was to make a preliminary design of the failure test, assess the technical feasibility of the test and to give input information for further numerical modelling of the test.

The site planned for execution of the in-situ failure test is one of the experimental full-scale deposition holes in the Research Tunnel at Olkiluoto, which is a favourable location since the rock properties are already well known, the state of stress is low and will result in only minor deformation as a result of stress release, and because the extent of the excavation-disturbed zone adjacent to the walls of the full-scale holes is insignificant from the testing point of view.

The design of the failure test is reported and results of preliminary modelling are given in this report. The input information for future modelling includes a study of rock properties, fracture propagation in rock, in-situ stresses and the development of techniques for using the expanding agent to produce artificial stress field. The study showed that mechanical properties such as strength of gneissic tonalite, the main rock type in the Research Tunnel, depends highly on the orientation of schistocity.

The modelling presented provides an estimation of the distribution of stresses when the state of stress is less than the strength of the rock. After failure appears and fractures start to propagate the results of modelling are not valid and a description of the fracturing can be obtained from the results of reported laboratory tests of similar size of circular openings. The failure patterns associated with primary and spalling fractures in the in-situ test are expected to be very similar but it is possible that remote fractures will not be not generated.

Since the rock in the in-situ test has a clear orientation and the orientation also clearly affects the strength properties of the rock, it is evident that the generation of fractures and failure patterns will be guided by the most favourable orientation for crack propagation. The most favourable direction for primary tensile fractures is along the schistocity planes. The best orientation for the test hole is parallel to the schistocity plane and therefore the experimental arrangement is as close to two dimensional as possible which reduces the number of parameters in the analysis of results.

The in-situ failure test was shown to be technically feasible and a state of stress high enough to cause failure can be created artificially by using a proper expansive agent and design. The main result predicted by the work described is that failure will occur around the central hole of the test configuration in the form of primary tensile fractures and sidewall spalling.

LIST OF SYMBOLS

E	Young's modulus (Pa)
$\varepsilon_{1,2,3}$	strains corresponding to major, intermediate and minor principal stresses (m/m)
ε	strain (m/m)
ε_v	volumetric strain (m^3/m^3)
ϕ	friction angle (degrees)
$\sigma_{1,2,3}$	major, intermediate and minor principal stress (Pa)
σ_{ucs}	unconfined compressive strength (Pa)
σ_{c50}	uniaxial compressive strength of 50 mm diameter specimen (Pa)
$\sigma_{ci,}$	crack initiation stress (Pa)
$\sigma_{cd,}$	crack damage stress (Pa)
σ_p	uniaxial compressive strength (Pa)
σ_t	tensile strength (Pa)
v	Poisson's ratio

TABLE OF CONTENTS

1 INTRODUCTION

1.1 General

An failure test suitable for execution in the Research Tunnel at Olkiluoto has been designed to study the failure of rock in-situ. Failures in rock and rock mechanical properties related to the mechanical stability of rock intended for use as a deep underground repository for spent nuclear fuel in the Finnish bedrock have been the subject of previous studies from a variety of points of view (Johansson et al. 1991, Hakala et al. 1993, Tolppanen et al. 1995, Hakala & Heikkilä 1997 and Hakala 1998). These studies have promoted the general understanding for evaluating rock stability. The repository for spent fuel shall be designed on the basis that there shall not be fracture propagation resulting in significant uncontrolled rock failures and thefore it is important to develop proper tools for assessing the possibility for failures.

Experience has shown that even if the conventional testing and modelling methods indicate that rock will fail, failure may well be a fairly localised phenomenon. It has been found in many cases, that even extensive failure and deformation of the underground space has a tendency to find a proper stable state and shape. Experience from deep underground facilities such as the Underground Research Laboratory (URL) in Manitoba or deep mines in crystalline rock have proved that it is still feasible to construct undergound facilities even if rock failure occurs, given the condition that the deformation of rock reaches a stable state. Examples from URL with respect to large holes reported by Read&Martino (1996) and mine-by experiment reported by Chandler et al. (1996) indicate that extensive breakouts don't result in significant failures and rock stability problems and from the constructability point of view, it is possible to excavate tunnels effciently even if breakouts occur. Chandler et al. (1996) demonstrated in the mine-by experiment that excavations with little observable damage can be created in highly-stressed rock providing that they are properly designed.

To be able to design stable underground spaces in environments where there is possibility for localized high stress concentrations we have to understand the mechanisms and processes that result in fracture generation, propagation and rock failure. The key factor in assessing the stability of an excavated opening in case of rock failure is to define whether the deformation of the rock can be controlled, and whether it reaches a stable state by seeking a favourable shape for the opening - something that has been observed on many occasions in the field - or whether it turns out to be the worst case, a violent rock burst. In all cases, fracturing of the rock must occur for the rock to be damaged and therefore a significant component of progressive failure is fracture propagation which is also practically always caused by all drill and blast excavation at some extent. Modelling of progressive failure should therefore include a mechanism for simulating fracture propagation.

The development of computers and associated modelling programs has led to a situation in which it is possible to model fracture propagation in three dimensional geometries by using programs such as the Particle Flow Code (PFC) by Itasca. The sizes of such models are quite limited and most of methods of this type are today used for research purposes. Examples of the modelling work carried at URL in the Mine-by tunnel strongly imply that as computers become more efficient and the knowledge of methods and applications becomes wider, the modelling of fracture propagation around underground openings will become more feasible.

The general objective of an in-situ failure test is to assess the applicability of numerical modelling codes and methods to the study of rock failure and associated crack propagation. One of the main tasks in an in-situ failure test is to carry out the modelling of rock failure by using both a conventional method of modelling without fracture propagation and a more sophisticated method capable of modelling the fracture propagation process. The observed failure patterns and the results obtained from the computer model are compared and evaluated. One prerequisite is that the computer programs used are currently available commercial products and that no development work on the actual program code shall be carried out.

Preliminary design of the failure test reported here was the first phase of the in-situ failure test. The objective was to assess the feasibility of the test and to provide input information for the modelling process. The first step in the design phase was the modelling of the failure test in three dimensions (3D) by using Flac^{3D} code (Itasca 1995b), and a complementary modelling using a modified test geometry. These steps are reported in this paper. Other design tasks included in the work were the study of rock properties, the study of in-situ stresses and the development of techniques for using the expanding agent. The design of the failure test will be finalised after the completion of a field trial and further detailed modelling.

The site planned for execution of the in-situ failure test is one of the experimental full-scale deposition holes in the Research Tunnel at Olkiluoto, which is a favourable location since the rock properties are already well known, the state of stress is low and will result in only minor deformation as a result of stress release, and because the extent of the excavation-disturbed zone adjacent to the walls of the full-scale holes is insignificant from the testing point of view.

1.2   The Research Tunnel

The Research Tunnel is located at a depth of 60 m in the VLJ-repository, which is an underground disposal facility for the low- and medium-level waste generated by the Olkiluoto nuclear power plant. The repository is located 1 km from the Olkiluoto 1 and 2 powerplants on Olkiluoto island on the southwest coast of Finland. The repository began operating in 1992. The Research Tunnel is 47 m long and between 4 and 7 m high. It was excavated using conventional drill and blast techniques.

The VLJ-repository has been excavated in an east-west striking tonalite formation surrounded by mica gneiss. The rock types found in the Research Tunnel are gneissic tonalite and pegmatite. The tonalite is usually slightly-foliated, medium-grained,

massive and sparsely-fractured. Besides the gneissic tonalite, which is referred to as anisotropic tonalite or gneissic tonalite, a fine-grained, homogeneous tonalite variant is also met. Pegmatite is found as veins and is non-foliated, coarse-grained, massive and sparsely-fractured (Äikäs & Sacklén 1993).

The main rock type found in the full-scale holes is gneissic tonalite. Minor sections consisting of pegmatite are also found. In addition, a small section consisting of homogeneous tonalite is found in full-scale hole Number 3 (see Fig.1.2-1) between the pegmatite and anisotropic tonalite. The orientation of fractures in the Research Tunnel can be divided into four different groups. The set of steeply-dipping fractures (dip direction east-west) is dominant.
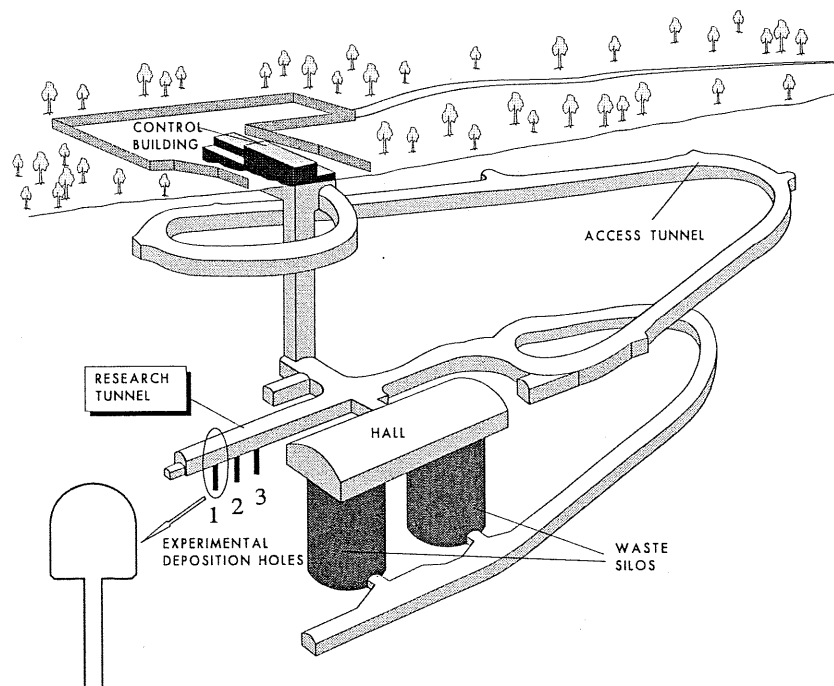

Figure 1.2-1. The Research Tunnel at Olkiluoto showing the full-scale experimental deposition holes.

2 DESCRIPTION OF THE IN SITU FAILURE TEST

The geometry for the in-situ failure test consists of a horizontally-oriented hole with identical slots positioned vertically above and below it, see Figure 2-1. The preliminary diameter and length of the central hole are 200 mm and 500 mm respectively. The closest distance from the axis of the borehole to the surface of each slot is about 350 mm.
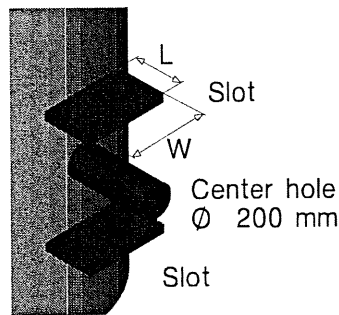

Figure 2-1. Basic geometry of the failure test.

The stress around the centre hole is created by filling the slots shown in Figure 2-1 with an expanding agent. The expansion pressure is multiplied around the centre hole because of the test geometry, which makes it possible to break the rock by using swelling pressures which are smaller than the compressive strength of the rock. Failure occurs around the central hole when the stress surrounding it becomes higher than the strength of the rock.

The test programme includes three phases: design, execution and analysis. After completion of the design phase the feasibility of the test will be evaluated before proceeding to the experimental (i.e. execution) phase which includes the following steps.

Preparation:
1. Coring of the test geometry
2. Instrumenting the test zone
3. Installation of the expanding agent and support structures.

Failure generation:
4. Monitoring
5. Pressure unloading.

Characterisation:
6. Mapping of failures
7. Impregnation of test hole
8. Sampling.

3   ROCK MECHANICAL PROPERTIES OF GNEISSIC TONALITE

3.1   General

A summary of all the previously-obtained rock mechanical properties of gneissic tonalite, which is the rock type in the area where the failure test is to be executed, are shown in Table 3.1-1. The strength values have been taken from (Johansson & Autio 1995) and are slightly higher than values obtained at an earlier date (Johansson & Autio 1993). The tensile strength of the gneissic tonalite, 9 MPa, and its deformation properties (Young's modulus of 58 GPa) are typical values for granitic rocks. Some of the properties are shown in Figures 3.1-1 and 3.1-2 with respect to common rock types.

The gneissic tonalite exhibits clear shistocity and it is therefore likely that the mechanical properties are oriented. The strength properties, Young's modulus and Poisson's ratio for gneissic tonalite were therefore studied in detail with respect to orientation and sample diameter using new samples taken from the experimental full-scale deposition holes at the Resaerch Tunnel at Olkiluoto.

Table 3.1-1.   Summary of the average rock mechanical properties of the gneissic tonalite in the Research Tunnel. The density of the gneissic tonalite is 2804 kg/m³ and porosity 0.15%.

σ_{ucs}[MPa]	σ_{cd}[MPa]	σ_{ci}[MPa]	σ_t[MPa]	E [GPa]	DRI	ν	CAI	Q-cont[%]	JF[pcs/m]
92	81	37	9,4	58	55	0,25	3,8	15-20	1

σ_{ucs}, σ_{cd}, σ_{ci} and σ_t are uniaxial compressive, crack damage, crack initiation and tensile strengths respectively. E is Young's modulus, ν is Poisson's ratio, DRI is drillability index, CAI is Cerchar abrasiveness index, Qis quartz content and JF is joint frequency.
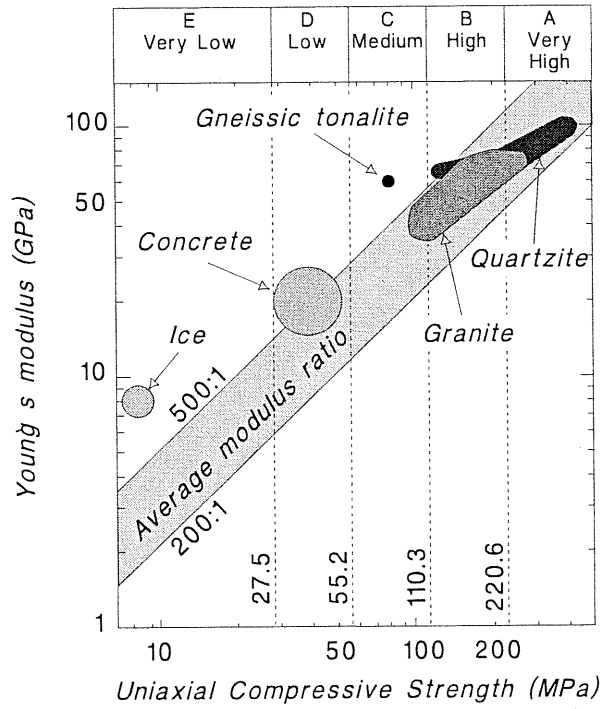
Figure 3.1-1. The position of gneissic tonalite in Deere's classification system.
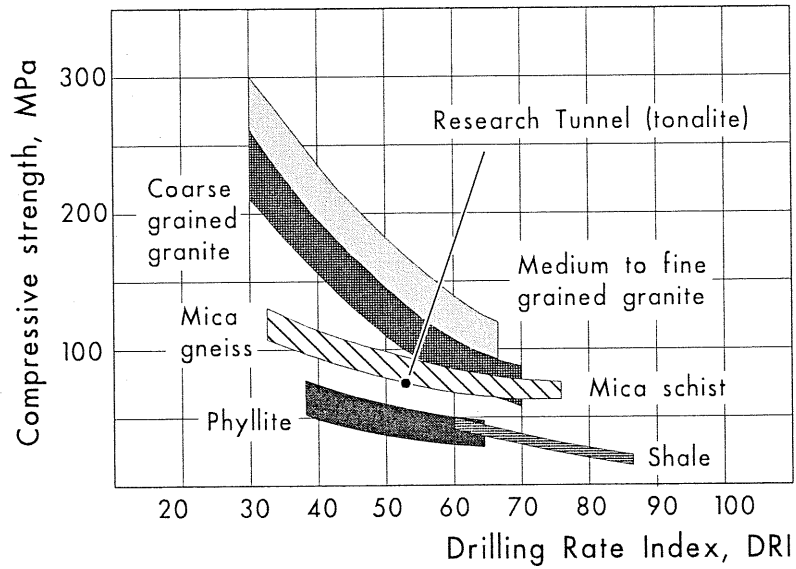

Figure 3.1-2. Relation between Drilling Rate Index, DRI and compressive strength in granitic rocks and in the Research Tunnel (Johansson 1994).

3.2 Test samples

The test samples were cored from the full-scale experimental deposition holes in the Research Tunnel at Olkiluoto. The coring process has been described by Autio et al. (1996). The diameter of the original core samples was 98 mm. Three size of specimens with nominal diamaters 41 mm, 54 mm and 98 mm were prepared from these original samples. The purpose behind testing the different sizes was to determine the scale dependency of the rock mechanical parameters. The sizes of the samples were determined so that the difference in the ratio of surface area to volume (a description of geometrical similarity) of the samples was distinct and as equal as possible. The nominal sizes and surface area to volume ratios of the samples is shown in Table 3.2-1.

Table 3.2-1. Nominal sizes of the samples (**S is the surface area and V is the volume of the sample). S/V describes the violation of geometric similarity, see Andreev,1995, p. 371 for additional information.

Diameter, D [mm]	Length, L [mm]	L/D	S/V** [mm^{-1}]
41	106	2.6	0.11
54	142	2.6	0.08
99	255	2.6	0.04

Details of the sample preparation and precise sample sizes have been given by Heikkilä (1997). The 54 mm samples with orientation of approximately 45 degrees were divided into four different groups: a) normal test-room conditioned samples to be tested using the normal loading rate of 0.75 MPa/s: b) same as a) but to be tested using a slower loading rate of 0.0075 MPa/s; c) totally water saturated samples; and d) totally-dry samples. The dried and saturated samples were prepared at the Technical Research Center of Finland and a detailed description of the procedures has been given by Pirhonen & Laaksonen (1997). Three additional 98 mm diameter samples were also tested using the lower loading rate.

3.3 Test equipment and procedure

The rock mechanical properties of the samples were determined at the Laboratory of Rock Engineering at the Helsinki University of Technology by using the MTS 815 Rock Mechanics testing system shown in Figure 3.3-1. The testing procedure was similar to the procedure presented by Hakala and Heikkilä (1997). Uniaxial loading was controlled by adjusting the radial strain rate to give two corresponding loading rates close to 0.75 MPa/s and 0.0075 MPa/s, depending on the sample group (see Chapter 3.2), in the linear part of the stress - deformation curve, see Figure 3.3-2.

One example of a stress-strain curve, volumetric strain and a definition of some of the rock mechanical parameters and regions of the behaviour of brittle rock under axial loading which are of importance are shown in Figure 3.3-3. Details of the test

procedure, data processing and determination of the rock mechanical parameters has been given by Hakala & Heikkilä (1997).

Axial deformations of the specimens were measured with MTS direct contact extensometers. The actuator displacement was also recorded. A circumferential chain extensometer ring encircling the centre of the sample (see Fig. 3.3-4) was used to measure the radial strain. There appears to be hysteresis in the strain values measured by the circumferential chain extensometer which is greater at large sample diameters. This is caused by friction (Hakala 1996, p 21) and the fact that the chain requires a minimum deformation before it starts to function correctly. The influence of the hysteresis on the results was studied by making three reference measurements with three 30 mm long radial strain gauges and the circumferential chain extensometer (see Figure 3.3-4 and 3.3-5). On the basis of the results of the reference measurements the strain gauges function more accurately at the beginning of loading when strains are small. As the strains grow larger (at higher loads) the chain extensometer functions more accurately than strain gauges. On the basis of the reference measurements a correction procedure was established to obtain proper radial strain values from the chain extensometer measurements. The radial strains measured by using the chain extensometer are valid as long as the sample has not suffered fracture.
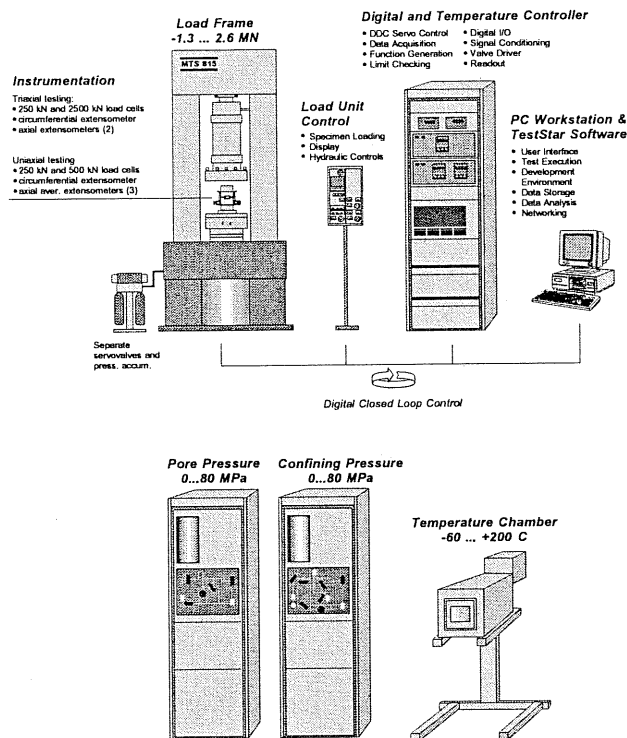

Figure 3.3-1. MTS 815 Rock Mechanics Test System at the Laboratory of Rock Engineering at the Helsinki University of Technology
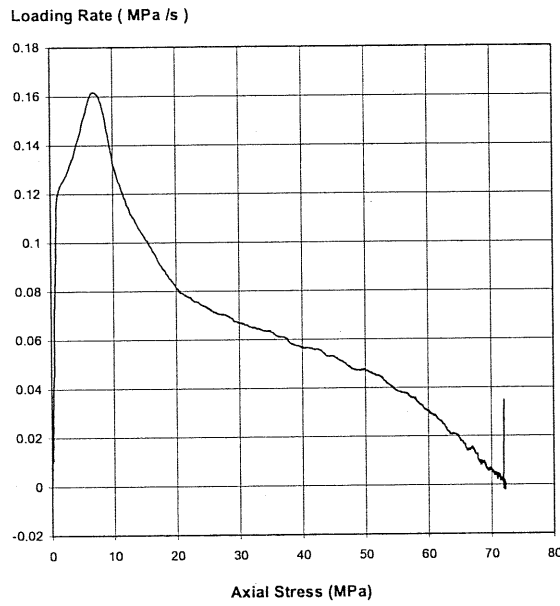
Loading Rate (MPa /s)

Axial Stress (MPa)

Figure 3.3-2. *Example of a measured loading rate versus axial stress for a 41 mm diameter sample.*

Axial Stress (MPa)

Onset of post-peak region V

Peak Strength σ_p
- temporary hardening

Unstable crack IV growth

Stable crack III growth

Crack Damage Stress σ_{cd}
- true peak strength

Elastic region II

Crack Initiation Stress σ_{ci}
- beginning of damage

Crack closure I

Radial Strain (%)

Tensile Strength σ_t

Axial Strain (%)

Volumetric Strain (%)

Measured total volumetric strain

Axial Stress
Axial Strain

Radial Strain

New Crack Volume

Crack Closure

Calculated Crack Volumetric Strain

Natural Microcracks
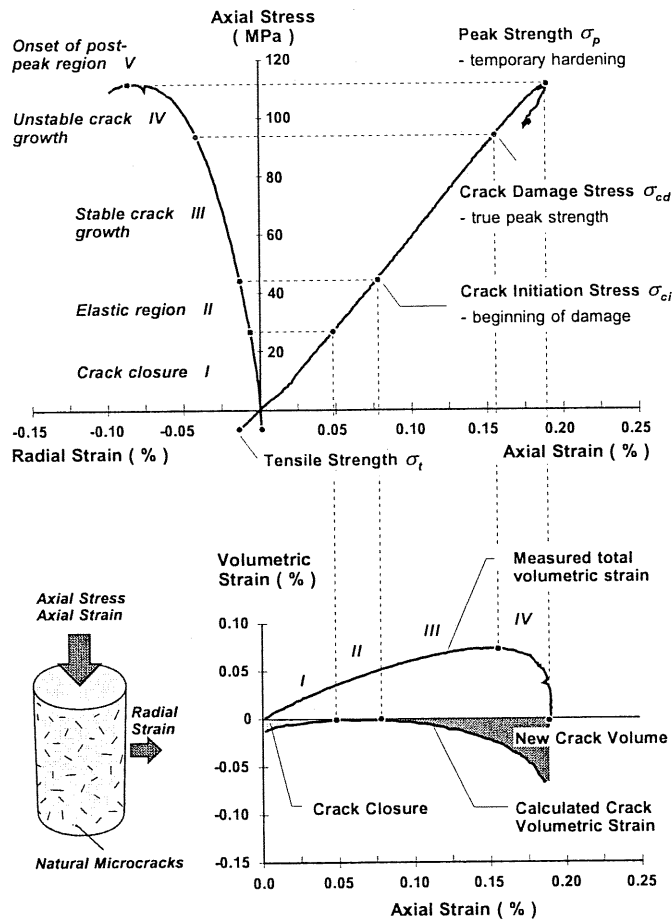
Axial Strain (%)

Figure 3.3-3. *Different regions of the behaviour of granitic rock at Olkiluoto under axial loading in terms of different strength parameters and volumetric strain modified by Hakala&Heikkilä (1997) after Martin (1994).*
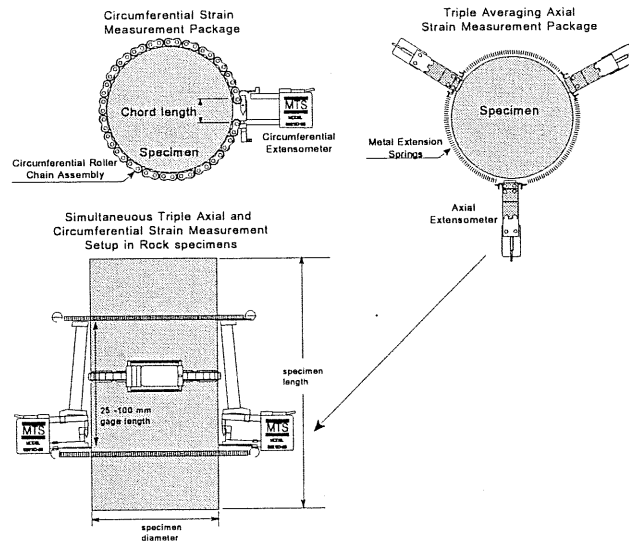
Figure 3.3-4. *The radial chain extensometer and direct contact extensometers arrangement. Hakala&Heikkilä (1997).*
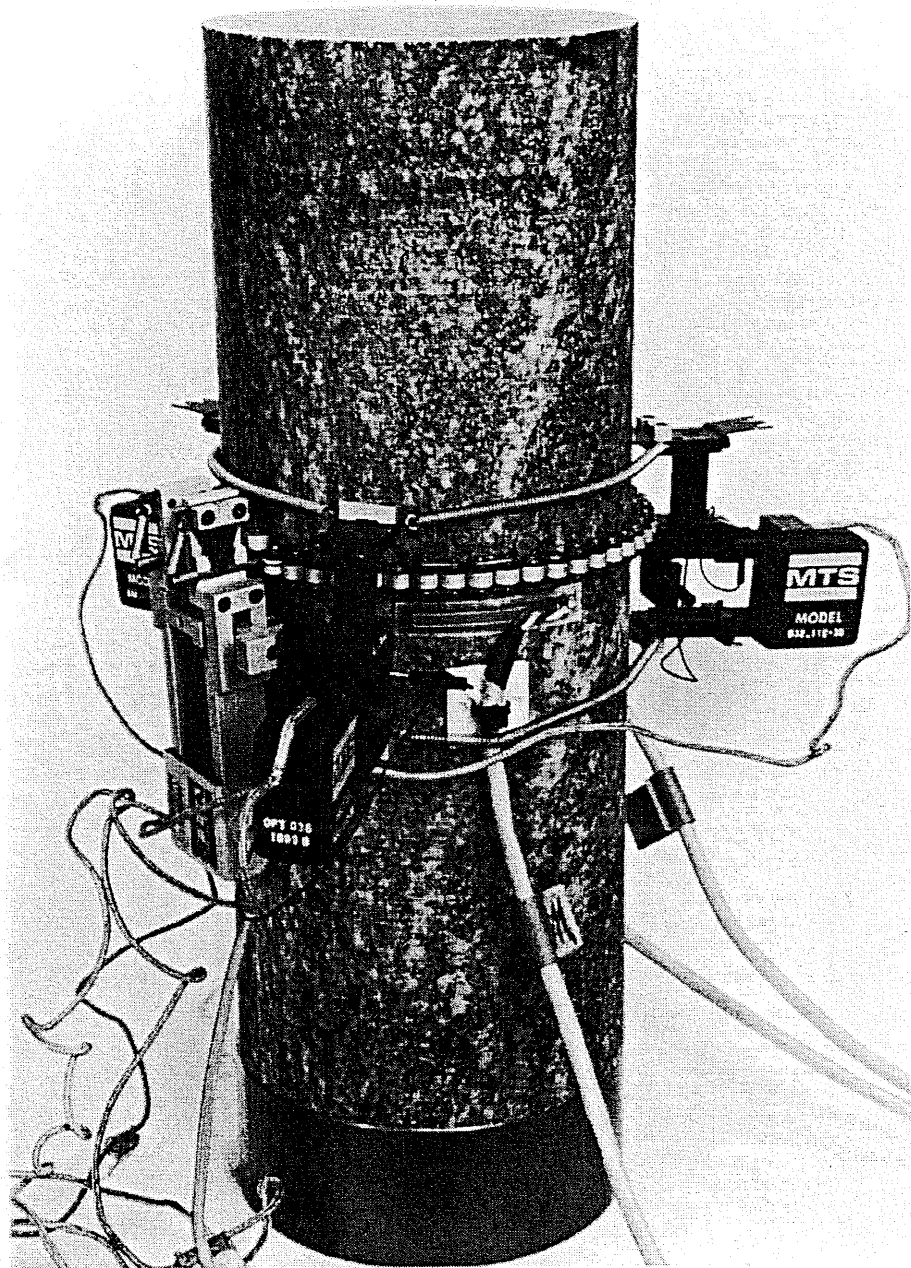
Figure 3.3-5. Strain gauge arrangement.

3.4 Results

3.4.1 Strength as a function of specimen orientation

Measurements of rock strength are presented in Tables 3.4-1 and 3.4-2. The uniaxial compressive strength as a function of the specimen size and rock orientation is shown in Figure 3.4-1. Orientation is defined as the angle between the axis of the sample and the schistocity planes, and is 0 degrees if the schistosity is oriented parallel to the axis of the sample. The orientations have been determined visually and the estimated maximum error, based on repetitive determinations, is in the range ±10 degrees and normally distributed.

A curve of second order was fitted to all the results obtained using normal loading and sample conditions. The measured data points and curve fits for the uniaxial crack initiation strength σ_{ci}, crack damage strength σ_{cd} and compressive strength σ_p of the 54 mm diameter samples obtained using normal loading and sample conditions are presented in Figure 3.4-2. The corresponding graphs for the 41 and 99 mm diameter samples are presented in Figures 3.4-3 and 3.4-4. The average Young's modulus of all the sample groups obtained using normal loading and sample conditions are presented in Figures 3.4-5 for the different orientation groups and sample diameters. The Young's modulus of all samples are presented in Figures 3.4-6, 3.4-7 and 3.4-8 for the different sample sizes. The average Poisson's ratios of all the sample groups obtained using normal loading and sample conditions are presented in Figure 3.4-9 for the different orientation groups and sample diameters The Poisson's ratios of all the samples obtained using normal loading and sample conditions are presented in Figures 3.4-10, 3.4-11, and 3.4-12.
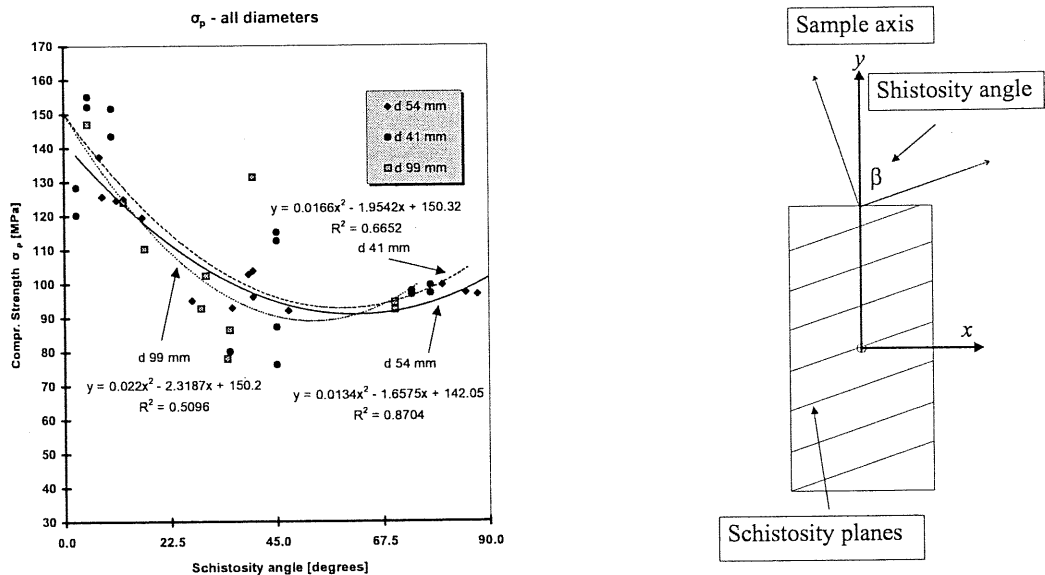

Figure 3.4-1. Definition of schistosity angle β, compressive strengths of all samples and second-order curve fit obtained using normal loading and sample conditions.

Table 3.4-1. The average strengths for different orientation groups of normally-tested samples. Orientation is the average orientation of the shistocity (i.e. deviation from the direction of the sample axis) for that group of samples.

Diameter [mm]	Orientation [Deg.]	E (Gpa)	σ_{ci} (Mpa)	σ_{cd} (Mpa)	σ_p (Mpa)
41	5.8	78.2	69.4	118.7	141.8
	43.0	61.4	48.6	76.9	94.2
	75.5	59.4	50.7	81.5	97.8
54	11.1	74.6	61.1	101.3	126.4
	38.6	66.0	51.7	81.0	97.1
	84.2	66.3	52.6	82.1	97.8
99	11.5	77.2	63.2	107.3	127.1
	33.7	68.1	58.8	85.5	98.1
	70.0	62.0	55.2	82.5	93.4

Table 3.4-2. The ratios of average strengths with respect to the strength of diagonally-oriented samples for different groups of normally-tested samples. Orientation is the average orientation of shistocity (i.e. deviation from the direction of the sample axis) for that group of samples.

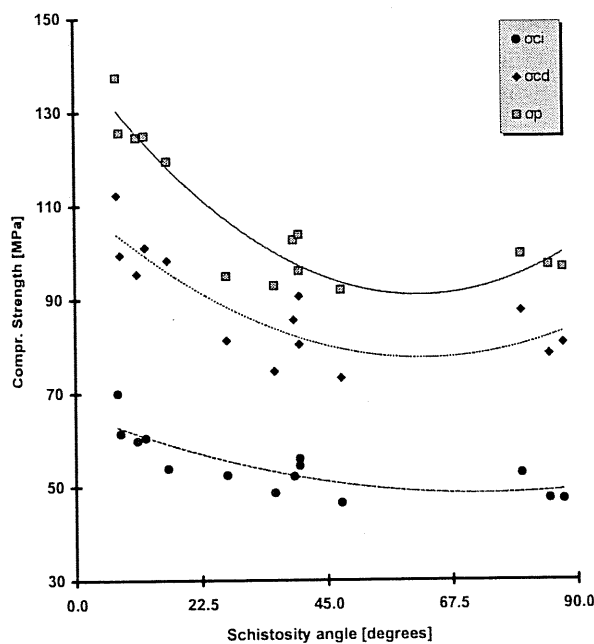| Diameter [mm]	Orientation [Deg.]	$E/E_{diag.}$	$\sigma_{ci}/\sigma_{ci\text{-}diag.}$	$\sigma_{cd}/\sigma_{cd\text{-}diag.}$	$\sigma_p/\sigma_{p\text{-}diag.}$
41	5.8	1.27	1.43	1.54	1.51
	43.0	1.00	1.00	1.00	1.00
	75.5	0.97	1.04	1.06	1.04
54	11.1	1.13	1.18	1.25	1.30
	38.6	1.00	1.00	1.00	1.00
	84.2	1.01	1.02	1.01	1.01
99	11.5	1.13	1.07	1.25	1.30
	33.7	1.00	1.00	1.00	1.00
	70.0	0.91	0.94	0.96	0.95

Figure 3.4-2. Crack initiation strength σ_{ci}, crack damage strength σ_{cd} and compressive strength of the 54 mm diameter samples obtained using normal loading and sample conditions.

Figure 3.4-3. *Crack initiation strength σ_{ci}, crack damage strength σ_{cd} and compressive strength of 41 mm diameter samples obtained using normal loading and sample conditions.*
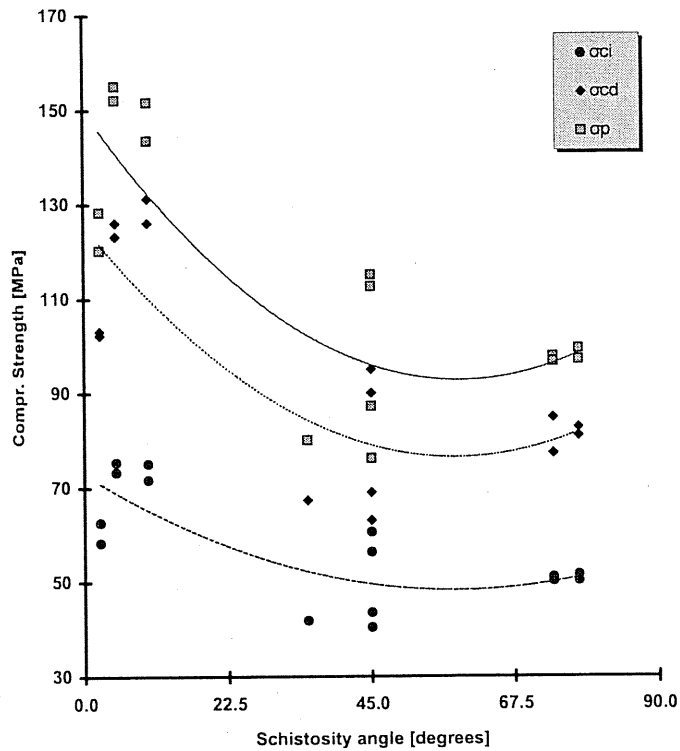

Figure 3.4-4. *Crack initiation strength σ_{ci}, crack damage strength σ_{cd} and compressive strength of 99 mm diameter samples obtained using normal loading and sample conditions.*
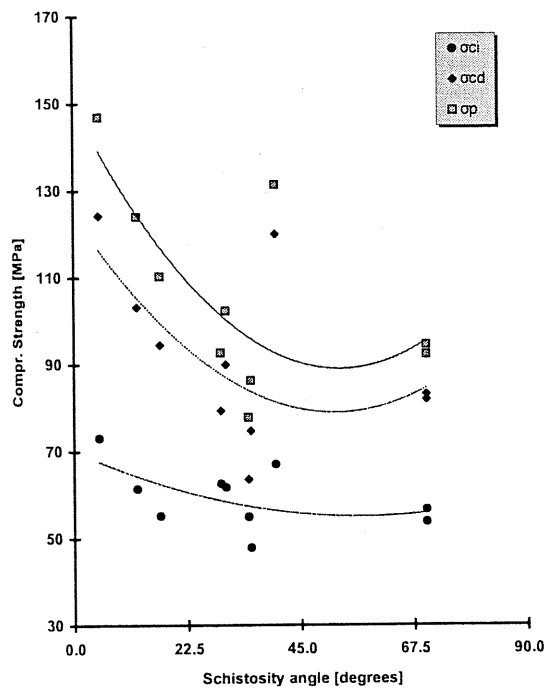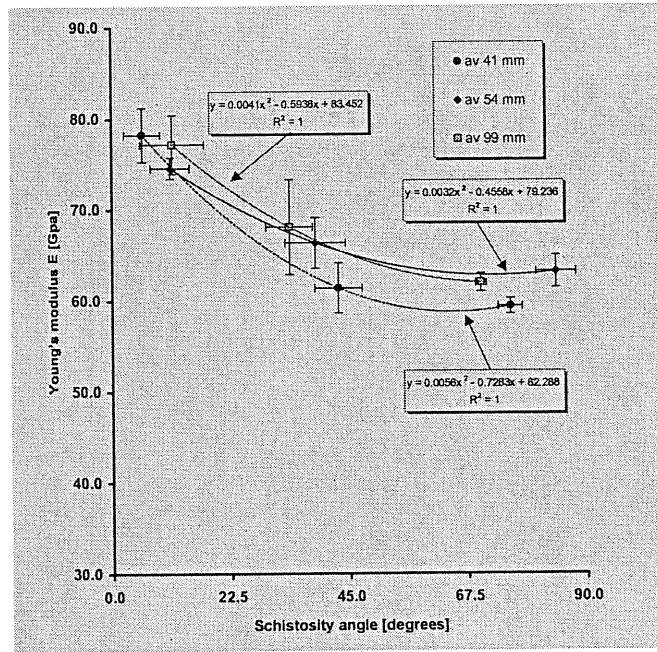
Figure 3.4-5. *Average Young's modulus E and second-order polynomial curve fit for all sample groups obtained using normal loading and sample conditions.*
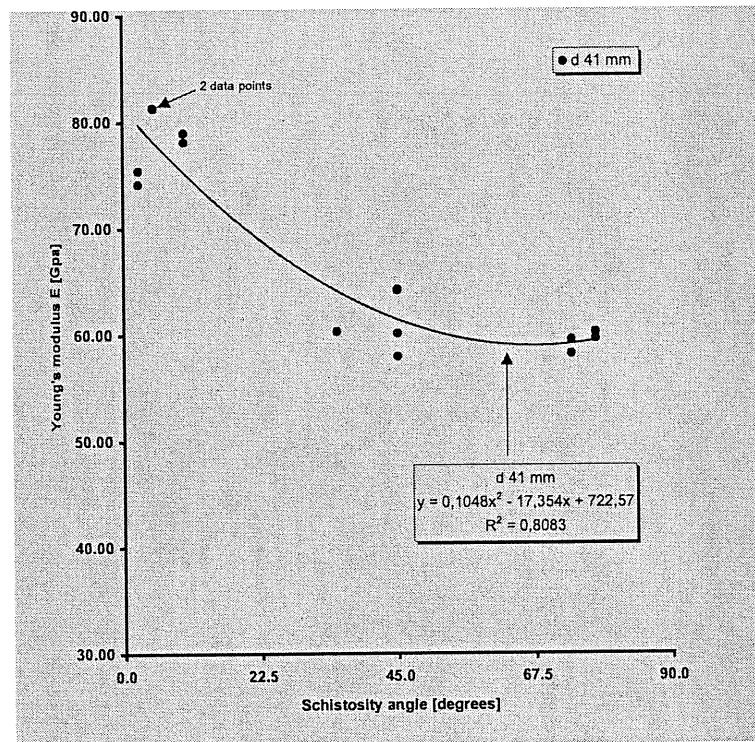

Figure 3.4-6. *Young's modulus E and second-order polynomial curve fit for diameter 41 mm samples obtained using normal loading and sample conditions.*

Figure 3.4-7. *Young's modulus E and second-order polynomial curve fit of diameter 54 mm samples obtained using normal loading and sample conditions.*
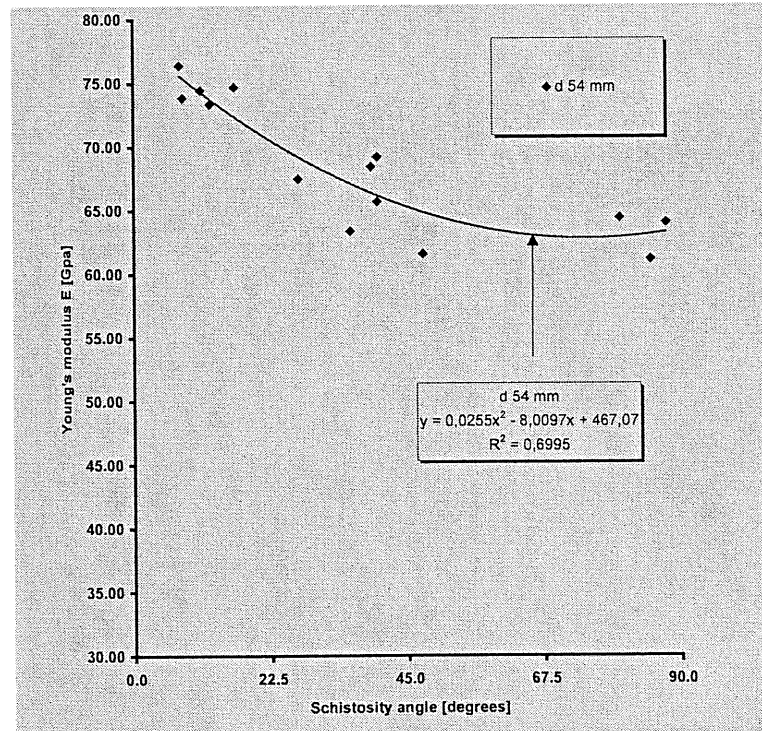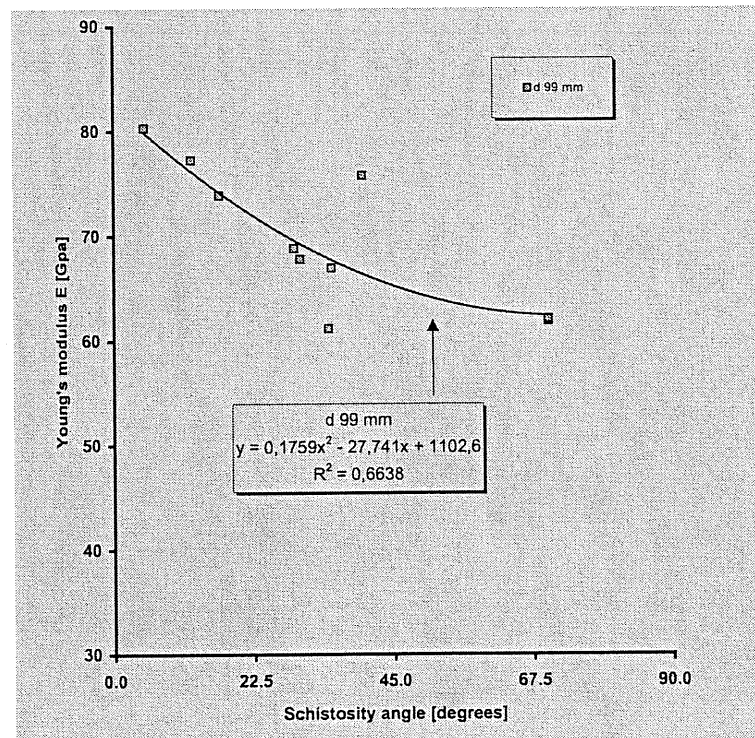

Figure 3.4-8. *Young's modulus E and second-order polynomial curve fit of diameter 99 mm samples obtained using normal loading and sample conditions.*
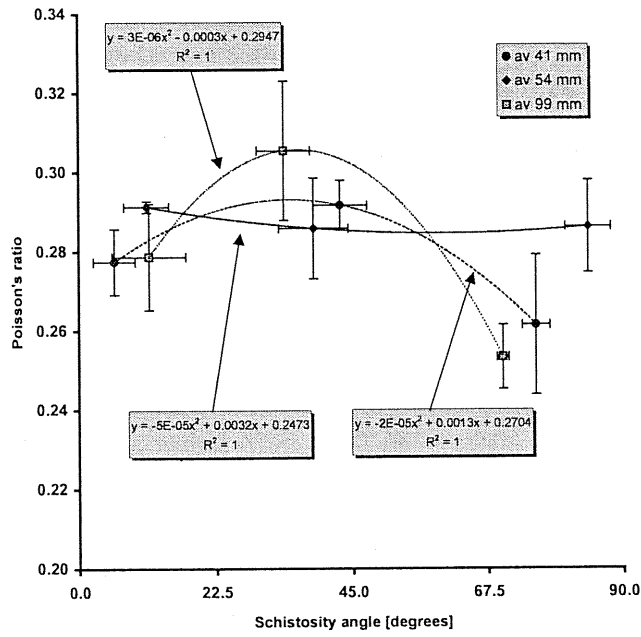
Figure 3.4-9. *Average Poisson's ratios for all samples obtained using normal loading and sample conditions.*
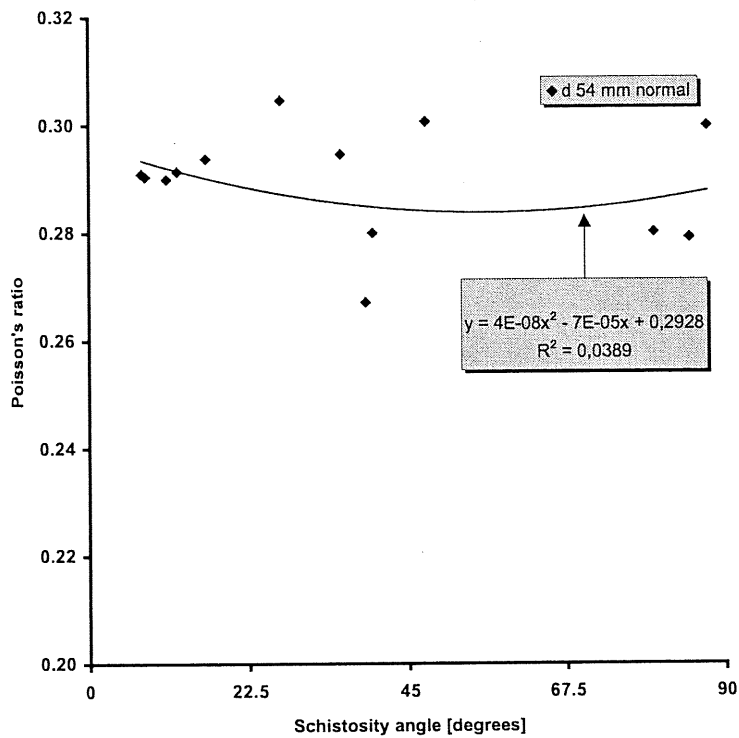

Figure 3.4-10. *Poisson's ratios for 54 mm diameter samples.*
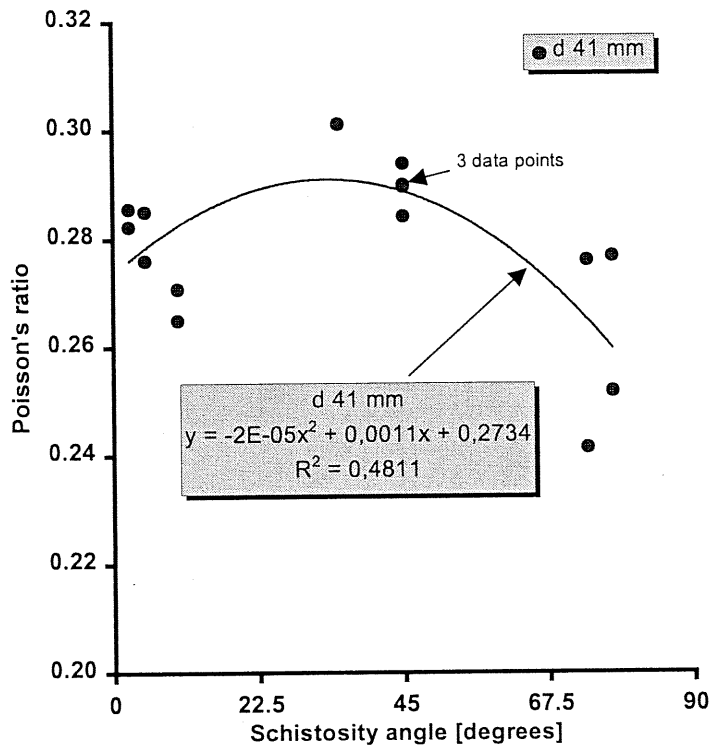
Figure 3.4-11. Poisson's ratios for 41 mm diameter samples.
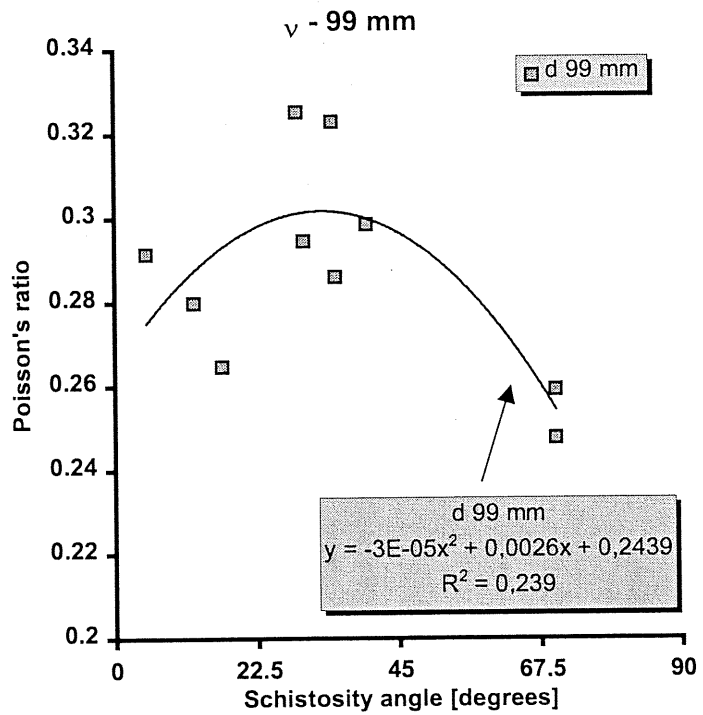

Figure 3.4-12. Poisson's ratios for 99 mm diameter samples.

On the basis of the results obtained it is obvious that rock strength and Young's modulus depend on rock orientation, while the effect of orientation on Poisson's ratio is not evident even though the results obtained with the 41 and 99 mm samples clearly suggest that Poisson's ratio is larger when the samples are oriented at a diagonal to the schistocity plane than in other directions. The scatter in the values obtained for Poisson's ratio using 54 mm samples was too large to draw any conclusions regarding this matter.

Young's modulus is at a maximum when the sample is oriented parallel to the schistocity plane and falls to about 20% of the maximum value when the orientation of the sample is approximately perpendicular to the schistocity plane.

The uniaxial compressive strengths shown in Figures 3.4-1, 3.4-2, 3.4-3, 3.4-5 and 3.4-13 are 23-50% larger than in samples which are parallel to the direction of the schistocity plane than in samples which are diagonal to it. The strength of samples which are oriented perpendicular to the schistocity plane are almost same (within 4%) as values obtained from samples which are diagonally oriented. The same considerations apply in principle to crack damage and crack initiation strengths.

The main conclusions from these results which characterise the behaviour of gneissic tonalite are:

1. The uniaxial compressive strength is at a maximum when the rock sample is directed parallel to the schistocity plane.

2. The uniaxial compressive strength is significantly lower, close to the minimum or at a minimum when the orientation of the rock samples is directed perpendicular to schistocity plane.

3. The values obtained from rock samples directed at an angle of 38-43 degrees to the schistocity plane do not differ significantly from the values obtained from samples directed perpendicular to the schistocity plane.

4. The variation in terms of the standard deviation of the measured strengths is smallest when the direction of the schistocity plane is perpendicular to the axis of the rock sample (see Fig. 3.4-13).

The result of this study conforms with the findings presented in the literature (Hoek&Brown 1980, Amadei 1983, Donath 1964) stating that the minimum value of rock strength occurs when the orientation of the schistocity plane is at an angle of between 30 and 40 degrees to the direction of sample axis, the angle being most commonly about 30 degrees. These results represent sandstones, slates and shales which are evidently different to granitic rocks. The main difference when compared to the behaviour presented in the literature is that the strength of the rock did not exhibit a clear increase when the orientation of schistocity approached a direction perpendicular to the sample axis. No corresponding studies were found in the literature in which the effect of the orientation of the schistocity plane in granitic rocks has been studied in detail.
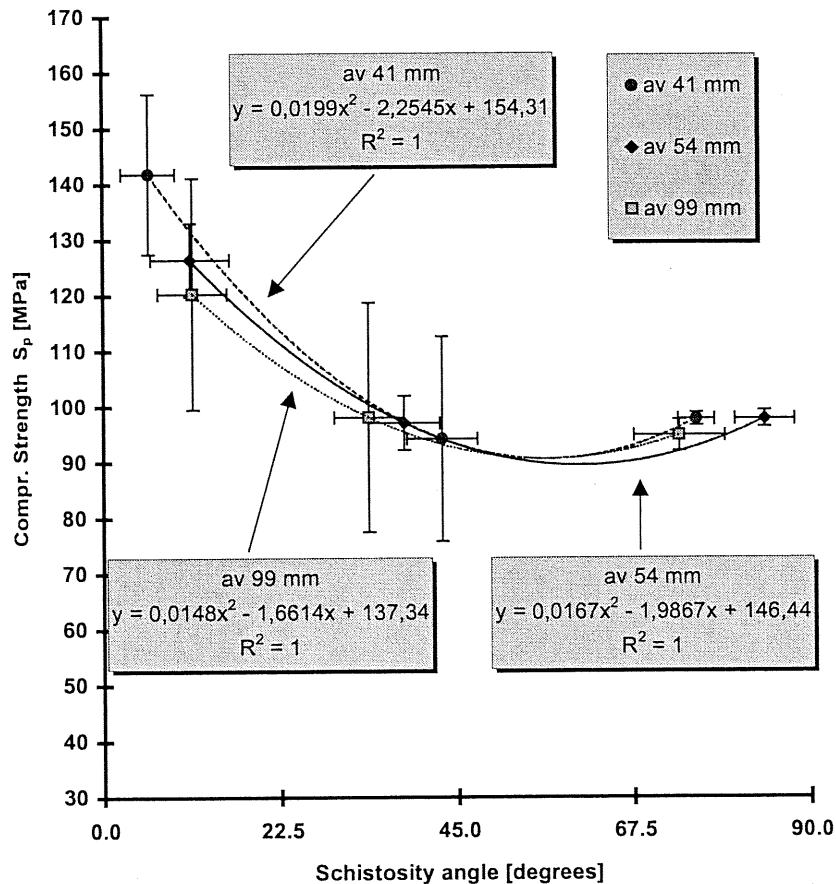
Figure 3.4-13. Uniaxial compressive strength rock samples, stardard deviation and second-order curve fit obtained using normal loading and sample conditions and calculated by using average values calculated for the three sample groups with different orientations.

3.4.2 Strength as a function of specimen diameter

The average strength values for the three different sample orientation groups and three different sample sizes were calculated (see Table 3.4-3 and Figure 3.4-13). The average crack initiation strength σ_{ci}, crack damage strength σ_{cd} and uniaxial compressive strength σ_p are shown in Figures 3.4-14 and 3.4-15 with corresponding curve fits. The average orientations of the different sample groups shown in Table 3.4-3 were different and the results were therefore made comparable by interpolating the strengths to represent the same orientation using two different formulae and are presented in Table 3.4-4. The first of these formulae corresponded to the second-order polynomial fit to the average values shown in Figure 3.4-13. The second formula corresponded to the second-order polynomial fit to all the data points shown in Figure 3.4-1. As can be seen from Table 3.4-4, the strength of the 41 mm and 99 mm diameter samples is within ±5% of the strength of the 54 mm diameter samples without any evidence of a systematic trend between the different orientation groups.

Table 3.4-3. The average compressive strength at different orientations with respect to the strength of 54 mm diameter samples. Orientation indicates the average orientation of the schistocity (i.e. the deviation from the direction of the sample axis) for that group of samples.

Diameter [mm]	Orientation [Deg.]	σ_p (Mpa)	$\sigma_p/\sigma_{p\text{-diag.}}$
Orientation 1			
41	6	141.8	1.12
54	11	126.4	1.00
99	12	127.1	1.01
Orientation 2			
41	43	94.2	0.97
54	39	97.1	1.00
99	34	98.1	1.01
Orientation 3			
41	76	97.8	1.00
54	84	97.8	1.00
99	70	93.4	0.95

Table 3.4-4. Average uniaxial compressive strengths with respect to the strength of the 54 mm diameter samples. The values have been made comparable by interpolating them to represent the same orientation by using the curve fits shown in Figures 3.4-13 for average data (values in the columns marked 1) in the table) and in Figure 3.4-1 for all data points (values in the columns marked 2) in the table).

Diameter [mm]	Orientation [Deg.]	1) σ_p (MPa)	1) $\sigma_p/\sigma_{p\text{-54 mm}}$	2) σ_p (MPa)	2) $\sigma_p/\sigma_{p\text{-54 mm}}$
Orientation 1					
41	11	132	1.04	131	1.04
54	11	127	1.00	125	1.00
99	11	121	0.95	127	1.02
Orientation 2					
41	39	97	1.02	100	1.02
54	39	95	1.00	98	1.00
99	39	95	1.01	93	0.95
Orientation 3					
41	70	94	1.05	95	1.03
54	70	89	1.00	92	1.00
99	70	94	1.05	96	1.04

Taking into consideration the standard deviations (as shown in Figure 3.4-13) it is clear that the differences between the values obtained from different diameter samples are insignificant. The observed differences between the different size samples in uniaxial compressive strength and other strength parameters (see Figures 3.4-5 and 3.4-9 for Young's modulus and Poisson's ratio) with respect to sample diameter are well within the standard deviations of the data (see Fig. 3.4-13) and are therefore not significant (at a length/diameter ratio of 2.6) even though there is a slight decrease in strength when the sample diameter is increased from 41 to 54 mm. The observation that the dependency of strength on sample diameter shown in Figures 3.4-17 and 3.4-18 is insignificant in the 41 to 99 mm diameter range is similar to the result obtained at URL (Lau et al. 1996) for grey granite in the 41 to 99 mm diameter range and shown in Figure 3.4-19, but differs from the relationship shown in Figure 3.4-16 which was obtained by Hoek&Brown (1980).
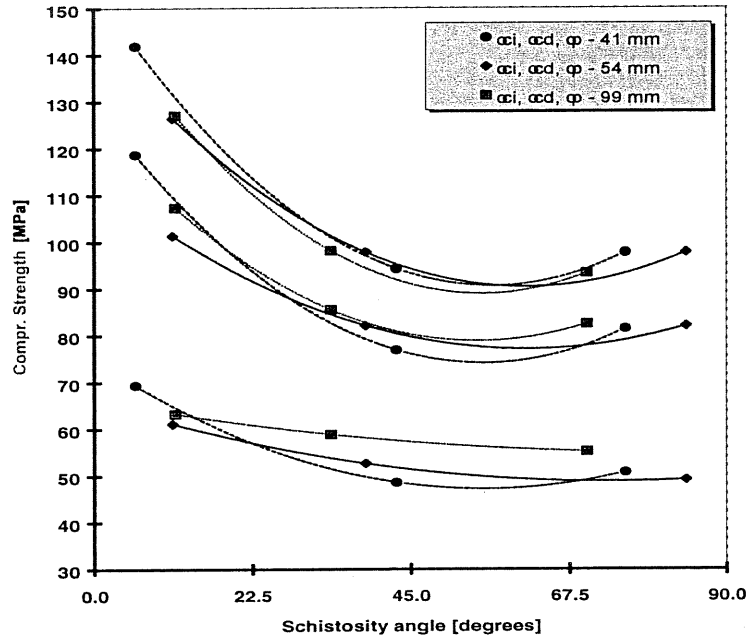
Figure 3.4-14. *Average crack initiation strength σ_{ci}, crack damage strength σ_{cd} and uniaxial compressive strength σ_p as a function of the sample orientation. This graph was calculated using average values for the three different sample orientation groups.*

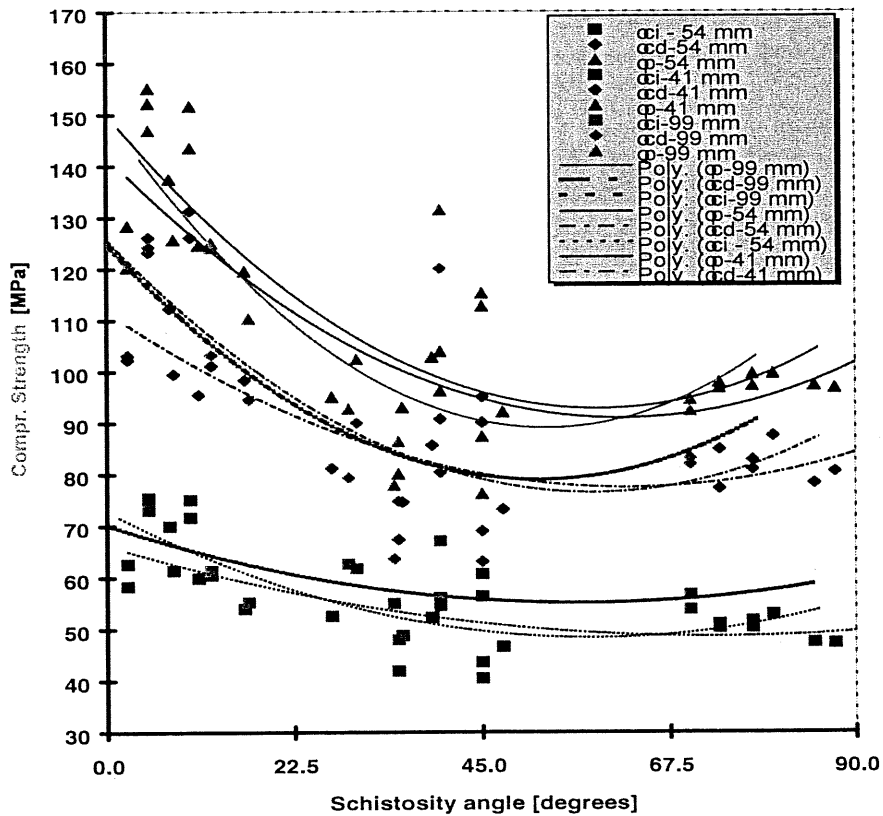**Figure 3.4-15.** *Crack initiation strength σ_{ci}, crack damage strength σ_{cd} and uniaxial compressive strength σ_p as a function of the sample orientation. The original curve fit (a second-order polynomial) for each data set is shown.*

The curve in the figure is labeled with the equation:

$$\frac{\sigma_c}{\sigma_{c50}} = \left(\frac{50}{d}\right)^{0.18}$$
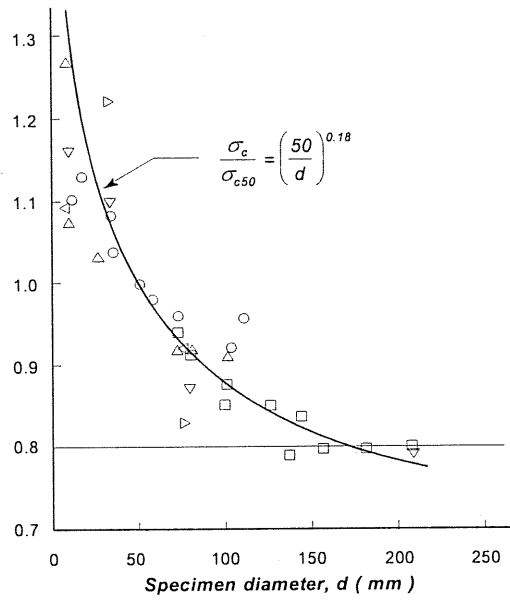
Axis label: Specimen diameter, d (mm)

Figure 3.4-16. *The effect of sample size on uniaxial compressive strength after Hoek & Brown (1980) and the average uniaxial compressive strength σ_p of gneissic tonalite at different orientations.*

Legend:
- 11 deg./1
- 39 deg./1
- 70 deg./1
- 11 deg./2
- 39 deg./2
- 70 deg./2

Axis labels: Compressive strength (vertical), Diameter (mm) (horizontal)
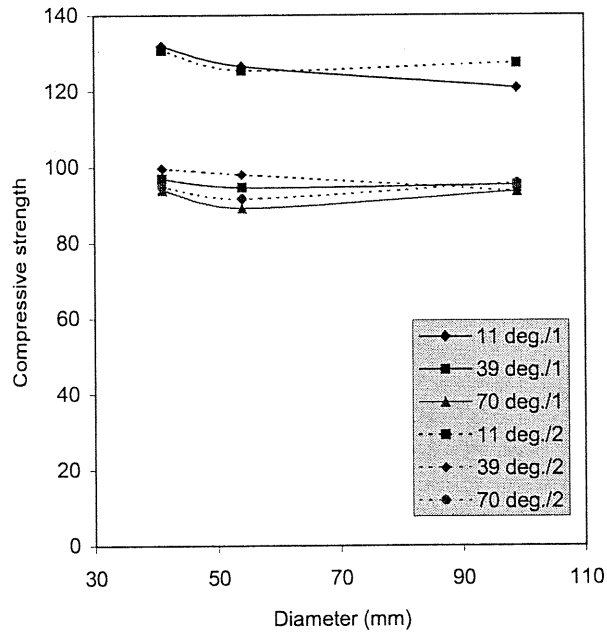
Figure 3.4-17. *The uniaxial compressive strength σ_p as a function of sample diameter for three different orientations. The values marked /1 have been interpolated to the same orientation using the curve fits shown in Figures 3.4-13 for average data. The values marked /2 have been interpolated to the same orientation using the curve fits shown in Figure 3.4-1 for all data points.*

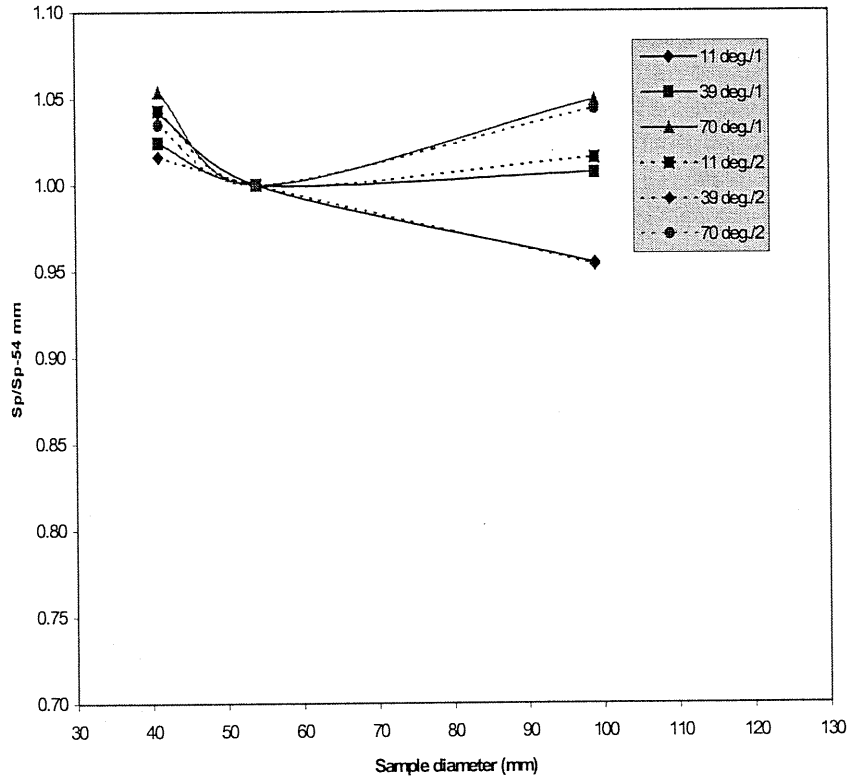**Figure 3.4-18.** *The same data as shown in Figure 3.4-17 shown in terms of the compressive strength S_p divided by the compressive strength of 54 mm samples S_p-54. See Figure 3.4-17 for explanation.*
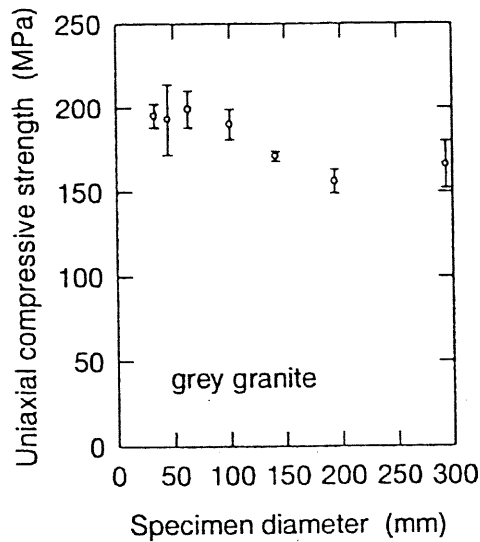

Figure 3.4-19. *Effect of sample size on the uniaxial compressive strength of grey granite at the Atomic Energy of Canada's Underground Research Laboratory in Manitoba after Lau et al. (1996).*

3.4.3 The effect of loading rate on strength

Loading rate has effect on rock strength and this was tested by using two different rates of loading. Loading was controlled by the radial strain when this exceeded 0.01%, so that loading rates in the post-peak deformation region (see Fig. 3.3-2) were close to 0.75 MPa/s (normal) and 0.0075 MPa/s (slow). Details of the test procedure can be found in Section 3.3. The results of the measurements obtained are presented in Table 3.4-5 and in Figures 3.4-20 and 3.4-21. According to these results, the uniaxial compressive strength is about 5% greater at the normal loading rate than at the slow loading rate. The reduction in strength observed was not as great as that found in URL gray granite (Lau et al. 1996) and shown in Figure 3.4-22.

Table 3.4-5. Uniaxial compressive, crack damage and crack initiation strengths for 54 mm diameter samples at loading rates of 0.75 MPa/s (normal) and 0.0075 MPa/s (slow). The schistocity of the samples is almost parallel to the axis of the samples (Orientation Group 1, direction of schistocity almost parallel (11°) to the axis of the sample.

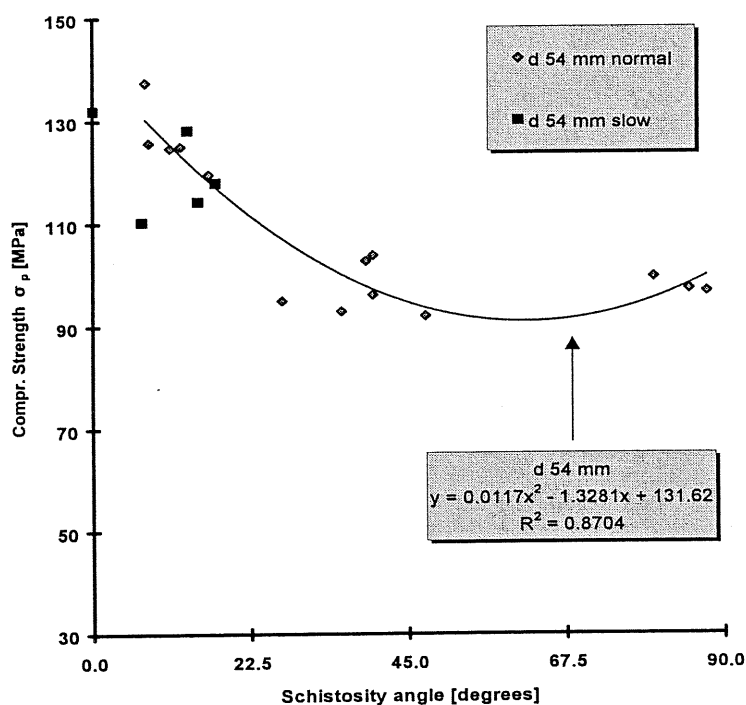| Loading rate		E (Gpa)	v	σci (Mpa)	σcd (Mpa)	σp (Mpa)
Slow	Average	75.8	0.3	57.7	99.6	120.5
	stdev	2.0	0.0	3.7	9.5	9.2
Normal	Average	74.6	0.3	61.1	101.3	126.4
	stdev	1.2	0.0	5.8	6.4	6.6
Normal/slow ratio		0.98	0.99	1.06	1.02	1.05

Figure 3.4-20. The uniaxial compressive of 54 mm diameter samples measured at loading rates of 0.75 MPa/s (normal) and 0.0075 MPa/s (slow). Details of the test procedure can be found in Section 3.3.
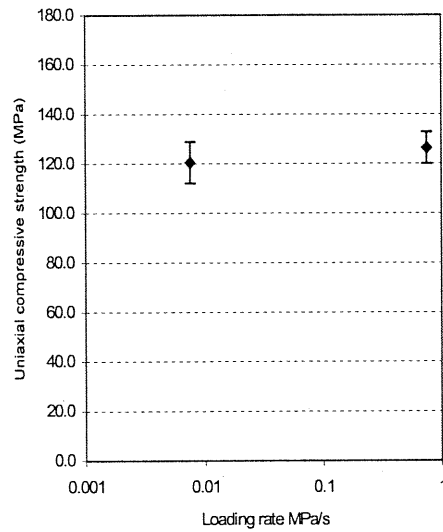
Figure 3.4-21. The uniaxial compressive strength and standard deviation of gneissic tonalite at different loading rates. The schistocity plane of the samples was at 11° to the sample axis.
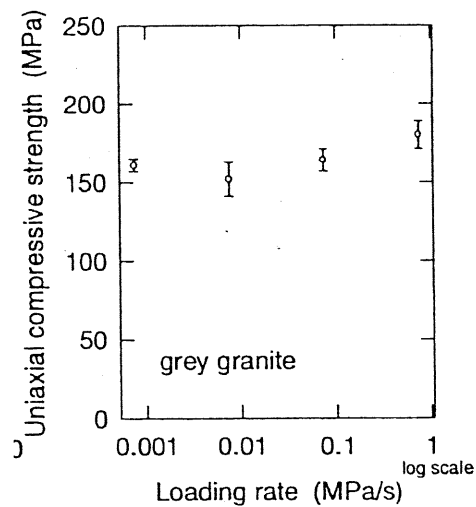
Figure 3.4-22. Effect of loading rate on the uniaxial compressive strength strength of grey granite as determined by the Atomic Energy of Canada's Underground Research Laboratory in Manitoba (Lau et al. 1996).

3.4.4 The effect of saturation state on strength

The water content of the test room conditioned (no drying or saturation) samples of average porosity 0.15% was 30-40% by volume and 0.014-0.024% by weight. To study the effect of saturation on rock strength, part of the samples were dried and part were totally saturated using a vacuum-immersion technique. The uniaxial compressive strengths obtained for the normal test room-conditioned samples, the dried samples and

the totally-saturated samples are shown in Figure 3.4-23. The average uniaxial compressive strength of the dried samples is close to the strength of test room samples and clearly higher than that of the totally-saturated samples. The average values obtained are shown in Table 3.4-6.

Table 3.4-6. **Uniaxial compressive, crack damage and crack initiation strengths of totally-saturated, dry and test room-conditioned 54 mm diameter samples. The orientation of the schistocity of the samples is approximately diagonal (30-40°) to the sample axis.**

Loading rate		E (Gpa)	v	σci (Mpa)	σcd (Mpa)	σp (Mpa)
Dry	Average	66.3	0.3	52.5	86.7	104.0
	stdev	3.5	0.0	4.6	5.1	7.3
Normal	Average	66.3	0.3	52.6	82.1	97.8
	stdev	2.8	0.0	3.4	6.6	4.9
Wet	Average	63.8	0.3	43.5	67.9	84.6
	stdev	7.8	0.0	5.8	8.3	10.4
Dry/Wet ratio		1.04	0.88	1.21	1.28	1.23

Legend:
◇ d 54 mm normal
◆ d 54 mm Wet test
● d 54 mm Dry test

d 54 mm
$y = 0.0117x^2 - 1.3281x + 131.62$
$R^2 = 0.8704$

y-axis: Compr. Strength σ_p [MPa]
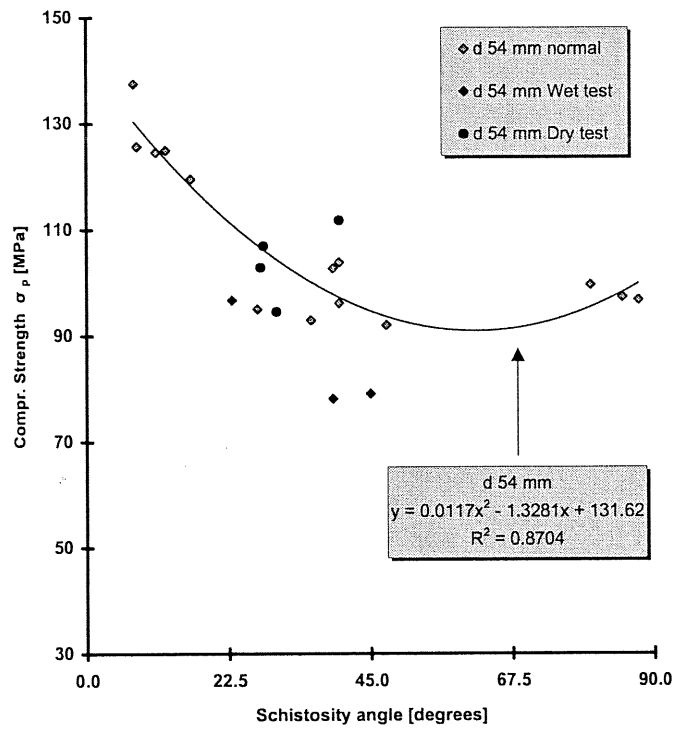x-axis: Schistosity angle [degrees]

Figure 3.4-23. *Uniaxial compressive strengths of totally-saturated (wet), dried (dry) and test room -conditioned (normal) 54 mm diameter samples. Details of the test procedure can be found in Section 3.3.*
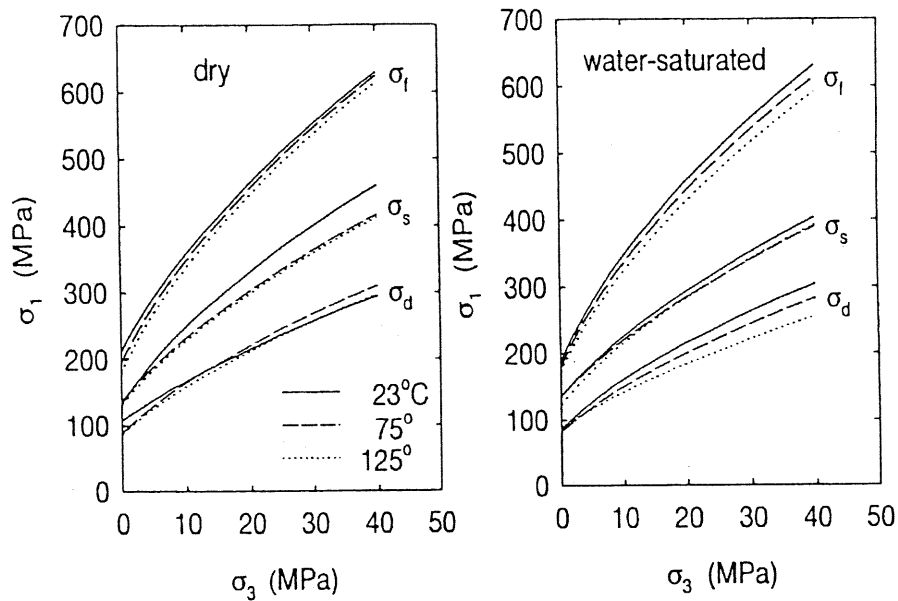
Figure 3.4-24. Hoek-Brown envelopes for dry and water-saturated pink granite at three temperatures by Lau et al. (1996). σ_f stands for peak strength.

These results show that the strength of dry samples is approximately 23% higher than that of totally-saturated samples. The results obtained differ from the results presented by Lau et al (1996) (Figure 3.2-24), by Lajtai et al. (1987) and by Martin (1994, p. 52), which show a difference of less than 5% in the compressive strength of dry and wet samples.

3.5 Mineralogy and petrography of gneissic tonalite

The main minerals in the anisotropic tonalite are quartz (15.6%), plagioclase (45.3%), biotite (26.4%) and hornblende (8.2%), and these four minerals constitute approximately 96% of the total mineral content as shown in Table 3.5-1 and Figure 3.5-1. The mafic minerals, especially the oblong grains of biotite and hornblende, are oriented, as seen in Figure 3.5-2. Grains are subhedral and the alteration to secondary minerals is insignificant.

The grain size of the quartz in the Research Tunnel at Olkiluoto is 0.3-0.5 mm, even though the size of the quartz clusters is 1-2 mm. The grain size of the plagioclase is larger, with the largest grains observed being between two and three millimetres in size. The anorthic content of the plagioclase is 31-32%. Biotite occurs as clusters of flaky grains with a typical size of between one and three millimetres.

Table 3.5-1. The average mineralogy of gneissic tonalite.

All samples Mineral	Average vol.-%
Quartz	15.6
Plagioclase	45.3
Potassium feldspar	-
Biotite	26.4
Hornblende	8.2
Sericite/Muscovite	0.9
Chlorite	0.4
Calsite/Carbonate	-
Epidote	0.3
Apatite	1.6
Sphene	0.6
Zircon	-
Opaque	1.0
Total	100
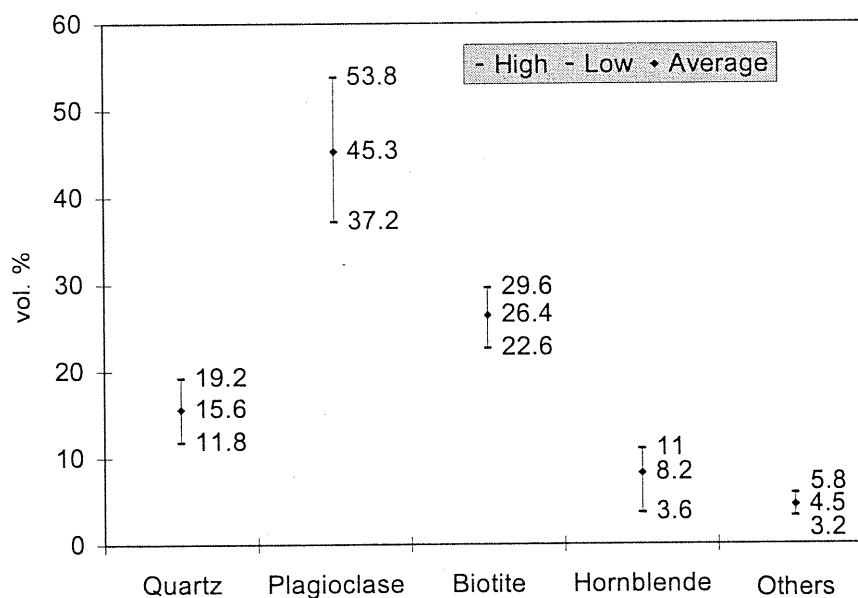
Figure 3.5-1. The mineral composition of gneissic tonalite.

According to results obtained using the ^{14}C-PMMA method and investigation by scanning electron microscope (SEM), the undisturbed rock matrix is solid and intragranular fissures are sparse. This observation is supported by the results obtained by examination using an optical microscopic. According to the ^{14}C-PMMA autoradiograms and optical microscope examination, the properties of the rock matrix are characterised by oriented clusters of mafic minerals with higher porosity. This can be seen in Figure 3.5-2 and Figure 3.5-3, both of which represent the same section. The

mineralogical content of the gneissic tonalite in the Research Tunnel and the basis for specification are shown together with the general classification of plutonic rocks in Figure 3.5-4.
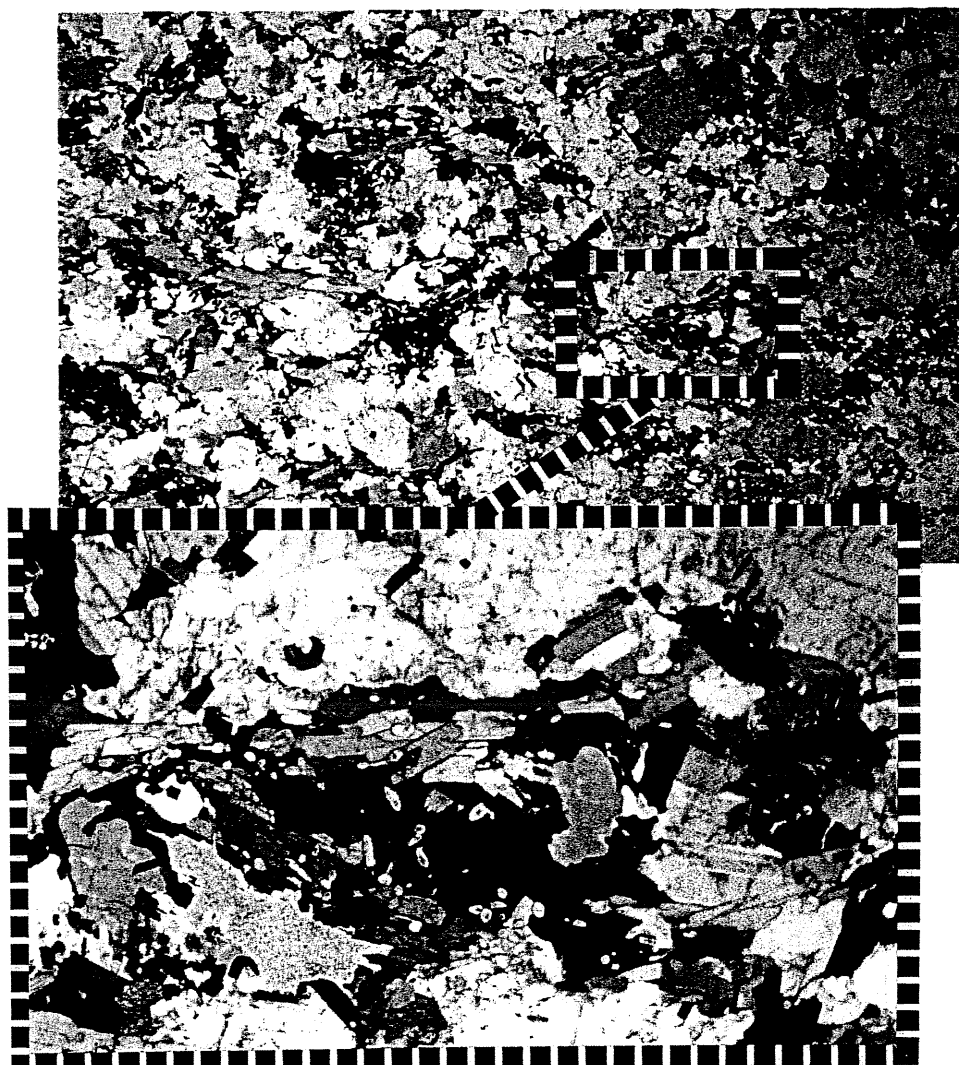
Figure 3.5-2. Photographs of a thin section of tonalite (sample B4.111, parallel nicols). The upper image is at a magnification of 5x and corresponds to the autoradiograph in Figure 3.5-3. The lower image shows a section of the upper image at a magnification of 25x. The quartz is mainly clear, the plagioclase is greyish and lamellar, the biotite is different shades of brownish-green, and the hornblende is darkish-green.

Figure 3.5-3. *Audioradiogram of the section of rock sample B4 shown in Figure 3.2-1 as a thin section. The darker, fracture-like features are areas of increased porosity.*

Figure 3.5-4. *The Q-A-P content of the gneissic tonalite in the large holes and the general classification of igneous rocks.*

3.6 Porosity and density
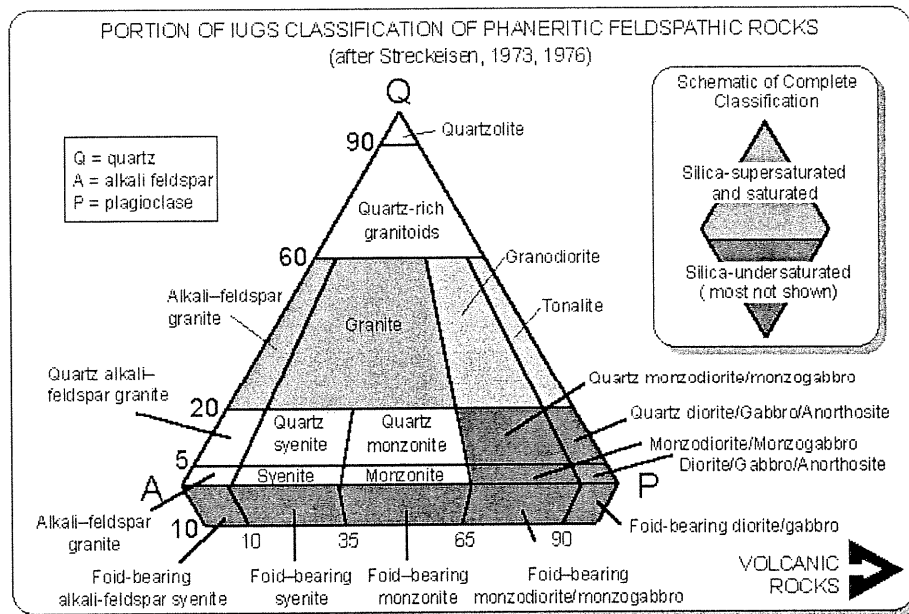
The average dry density of the gneissic tonalite is 2810 kg/m^3. The average porosity of the gneissic tonalite in the 54 mm diameter test samples determined using vacuum drying and water immersion (VTT-YKI) was 0.09-0.17% (by volume) with the average value obtained being 0.15%. The results of reference porosity determinations using smaller 27 mm diameter samples of gneissic tonalite and different techniques is presented in Figure 3.6-1. Porosities varied from 0.25 to 0.55% depending on the technique employed. It is considered that the real porosity of the 54 mm diameter test samples determined by the vacuum drying and water immersion technique (which was chosen to avoid heating the samples) should have been closer to the value 0.25% and that the difference was primarily caused by insufficient drying, even though the drying times used exceeded one and half months.
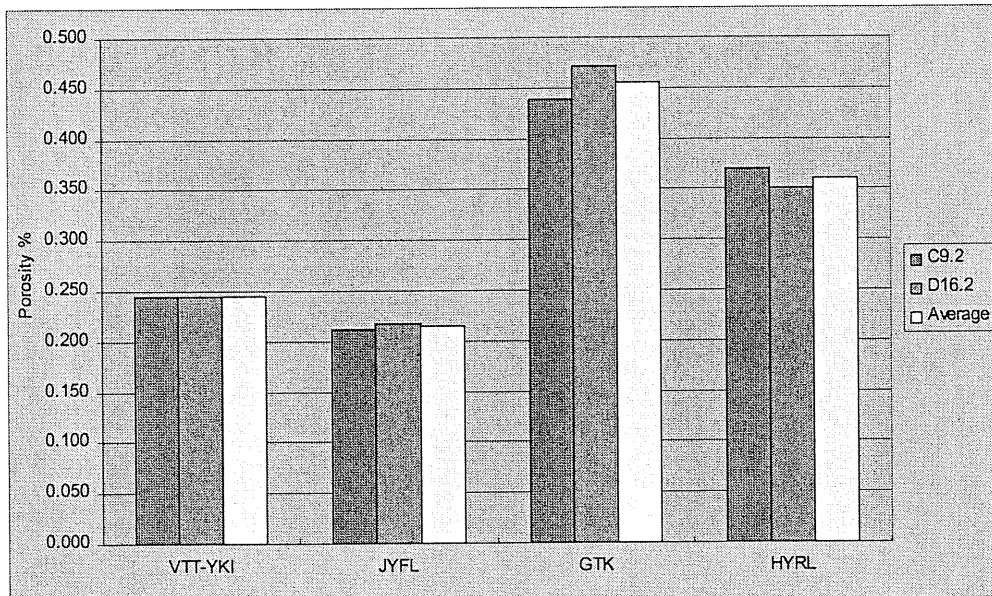

Figure 3.6-1. *Porosities of reference samples as obtained by different laboratories. VTT-YKI is the Technical Research Centre of Finland, JYFL is the University of Jyväskylä, GTK is the Geological Survey of Finland and HYRL is the University of Helsinki.*

3.7 Properties of tonalite forming minerals

The main minerals in the gneissic tonalite, which represent approximately 96% of the total mineral content, are plagioclase, biotite, quartz and hornblende. As shown in Table 3.7-1 these minerals have different values for stiffness and Poisson's ratio. The stresses caused by external forces such as tool indentation during boring are therefore distributed unevenly in the rock. Quartz and hornblende are the stiffest minerals and these both accept and transmit higher forces than the less-stiff minerals such as plagioclase and biotite. In general, plagioclase grains are stiffer than grains of biotite but the difference is not great and depends to a certain extent on the source of information employed (see

Table 3.7-1). One major difference between these last two minerals is that the anisotropy of biotite is large since the grains exhibit monoclinic perfect single cleavage and usually appear as clusters of flaky crystals.

Another significant difference is that the grains of plagioclase are much harder than the grains of biotite, as shown in Table 3.7-2 and Figure 3.7-1. Quartz is the hardest mineral in this composition. It should be kept in mind that even though some degree of correlation does exist, hardness is not the same as strength. It is a general trend that harder minerals exhibit more brittle behaviour than softer minerals.

Table 3.7-1. The main minerals in the gneissic tonalite and their stiffness parameters.

Mineral	Composition	Average vol.- %	ρ^{**} g/cm^3	υ^{**}	E^{**} GPa	ρ^{***} g/cm^3	υ^{***}	E^{***} GPa
Plagioclase (An$_{53}$)	Na-Ca-Al silicate	45	2.54	0.3	88.7	2.68	0.30	106.4
Biotite	K-Fe-Mg silicate	26	3.1	0.3	69.7	3.05	0.27	96.2
Quartz	SiO$_2$-β- type	16	2.53	0.2*	99.6	2.53	0.20	179.3
Hornblende	Ca-Fe-Mg silicate	8	3.17	0.3	146.0	3.12	0.29	184.0

E=Young's modulus; υ= Poisson's ratio; ρ=density
*   Poisson's ratio 0.08 has been presented for α-type quartz by Landolt&Börnstein 1982 and Zalesski
**   Zalesski 1964
*** Landolt&Börnstein 1982

Table 3.7-2. The main minerals in the gneissic tonalite and their hardness parameters.

Mineral	Composition	Average vol.- %	VHN* kg/mm^2	Hardness M
Plagioclase (An$_{53}$)	Na-Ca-Al silicate	45	800	6
Biotite	K-Fe-Mg silicate	26	110	2.5
Quartz	SiO$_2$-β-type	16	1060	7
Hornblende	Ca-Fe-Mg silicate	8	600	6

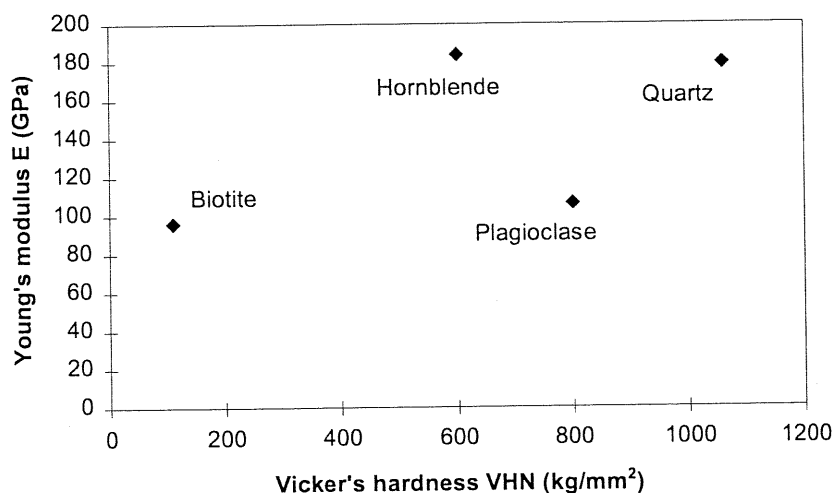VHN= Vicker's hardness; M= Mohs' hardness
* Salminen&Viitala 1985

Figure 3.7-1. Values for hardness and Young's modulus of the main minerals in the gneissic tonalite.

As shown in Table 3.7-3 and Figure 3.7-2, the velocity of compression waves is clearly higher in the hornblende, quartz and plagioclase than in the biotite and the same is true of the velocity of shear waves. The impedance of a mineral directly affects the reflection of stress waves at grain boundaries. Impedance values for biotite and quartz are quite similar but clearly smaller than those for quartz and hornblende. This dynamic mismatch and the difference in the velocity of elastic waves in plagioclase and biotite, the most common minerals in the gneissic tonalite, are clear and may have some effect upon the opening of grain boundaries during stress-wave propagation.

In addition to the properties of the individual mineral grains, deformation of the grain structure also depends on the degree to which the structure is heterogeneous and the precise nature of the intergranular bonding, which is in turn a function of intergranular porosity, microcracks and flaws in the bonds. When considering the deformation of the grain structure in the excavation-disturbed zone, it should be remembered that in this zone, both radial and tangential stress gradients adjacent to the open surface of the hole are high.

Table 3.7-3. The main minerals of the gneissic tonalite, their wave velocities and their impedances.

Mineral	Composition	Average vol.- %	v_c* m/s	v_s* m/s	I kg/sm^2
Plagioclase (An$_{53}$)	Na-Ca-Al silicate	45	6600	3540	1.77E+07
Biotite	K-Fe-Mg silicate	26	5350	3000	1.63E+07
Quartz	SiO$_2$-β-type	16	6635	4043	1.68E+07
Hornblende	Ca-Fe-Mg silicate	8	6810	3720	2.12E+07

v_c=velocity of compressive waves; v_s= velocity of shear waves; I= impedance
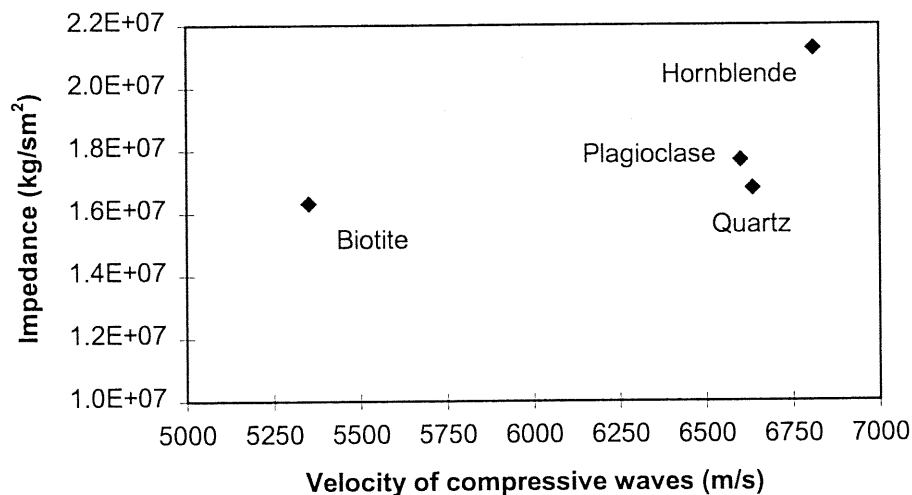* Landolt&Börnstein 1982

Figure 3.7-2. The velocity of compression waves and the impedance of the main minerals in the gneissic tonalite.

3.8 Observed failure patterns in uniaxial compressive testing

3.8.1 Uniaxial compressive strength

Three 54 mm diameter samples A2 (A2.2A), G6 (G6.2A) and E4 (E4.2A) representing three different orientations were studied using the ^{14}C-PMMA method. These samples had previously been tested for compressive strength and the rock mechanical properties of the samples are presented in Table 3.8-1 and Figure 3.8-1. The stress-strain deformation curves of the samples are shown in Figure 3.8-2.

Table 3.8-1. Samples used to study the fracturing caused by uniaxial compressive testing.

Sample	α	E (GPa)	v	σci (Mpa)	σcd (Mpa)	σp (Mpa)
a2	15	75	0.29	54	98	120
e4	45	62	0.30	47	73	92
g6	80	64	0.28	53	87	100

α is the angle between the sample axis and schistocity plane
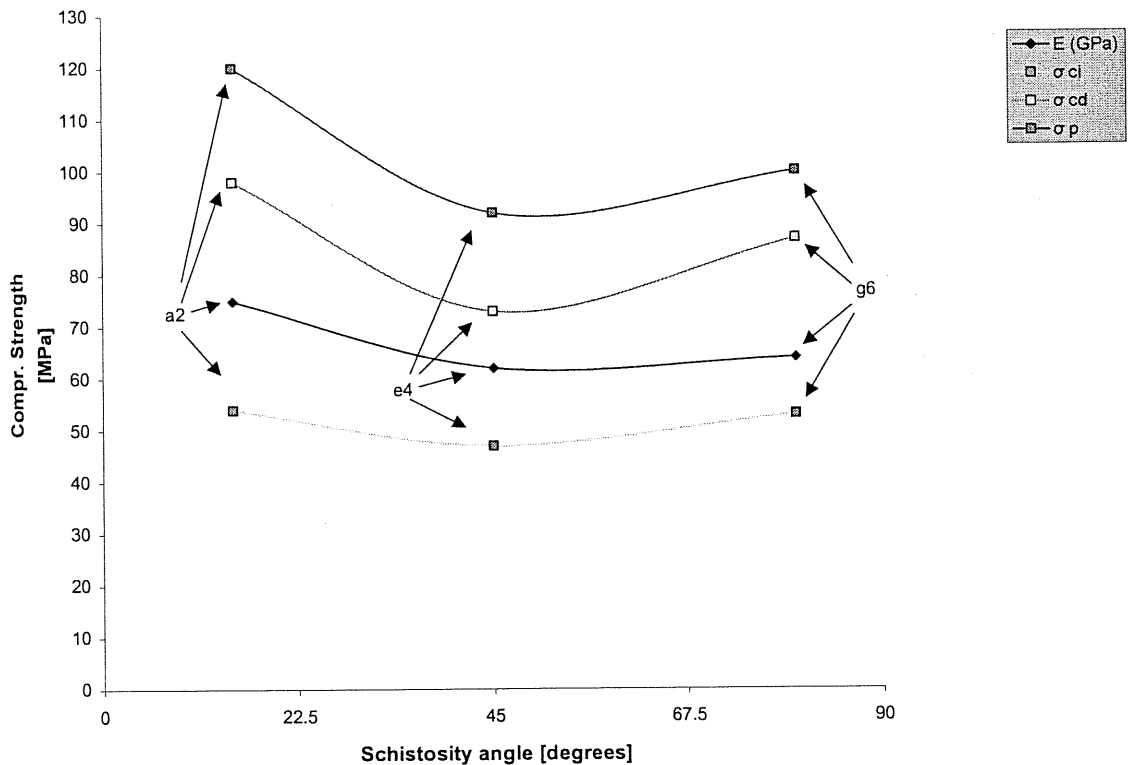
Figure 3.8-1. *Crack initiation strength* σ_{ci}*, crack damage strength* σ_{cd}*, compressive strength* σ_p *and Young's modulus E of 54 mm diameter samples obtained using normal loading and sample conditions.*
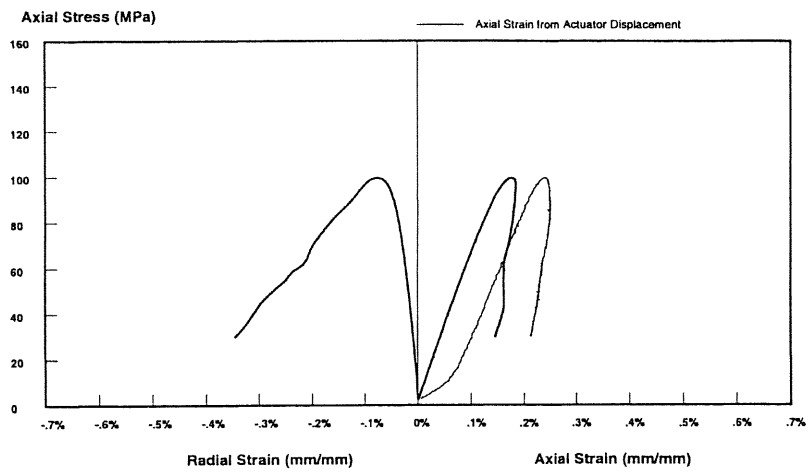
38
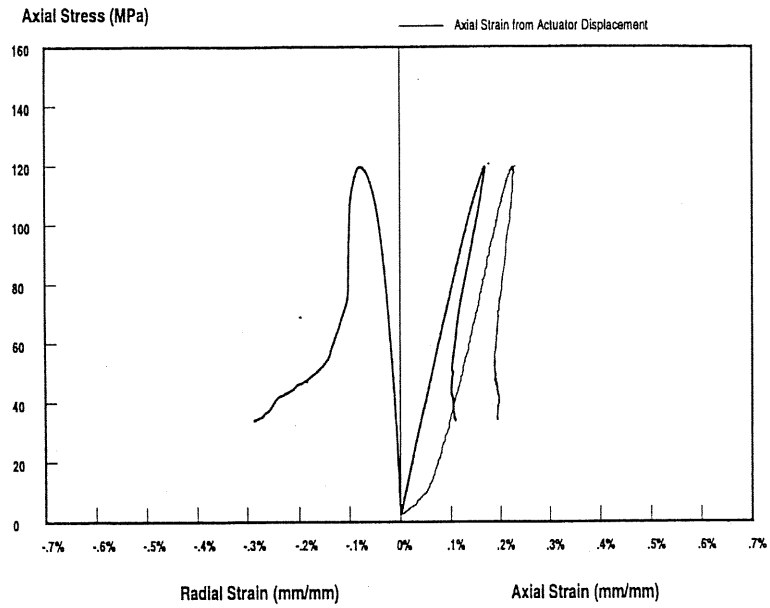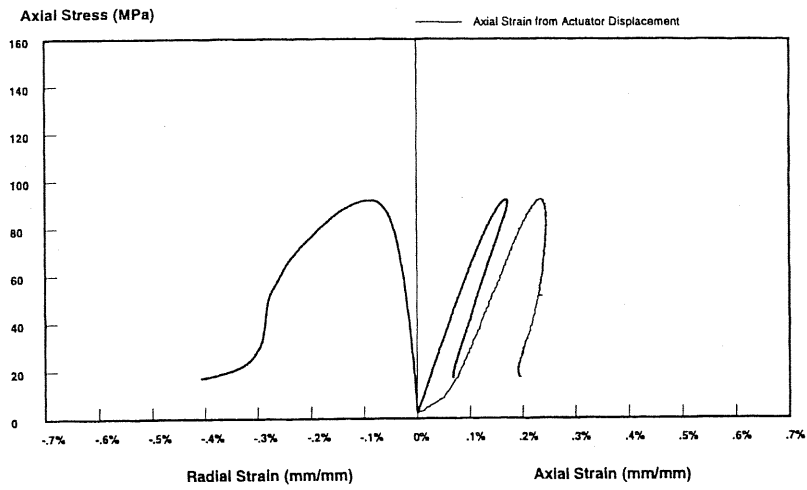
Figure 3.8-2. Stress-strain deformation curves for samples a2, e4 and g6.
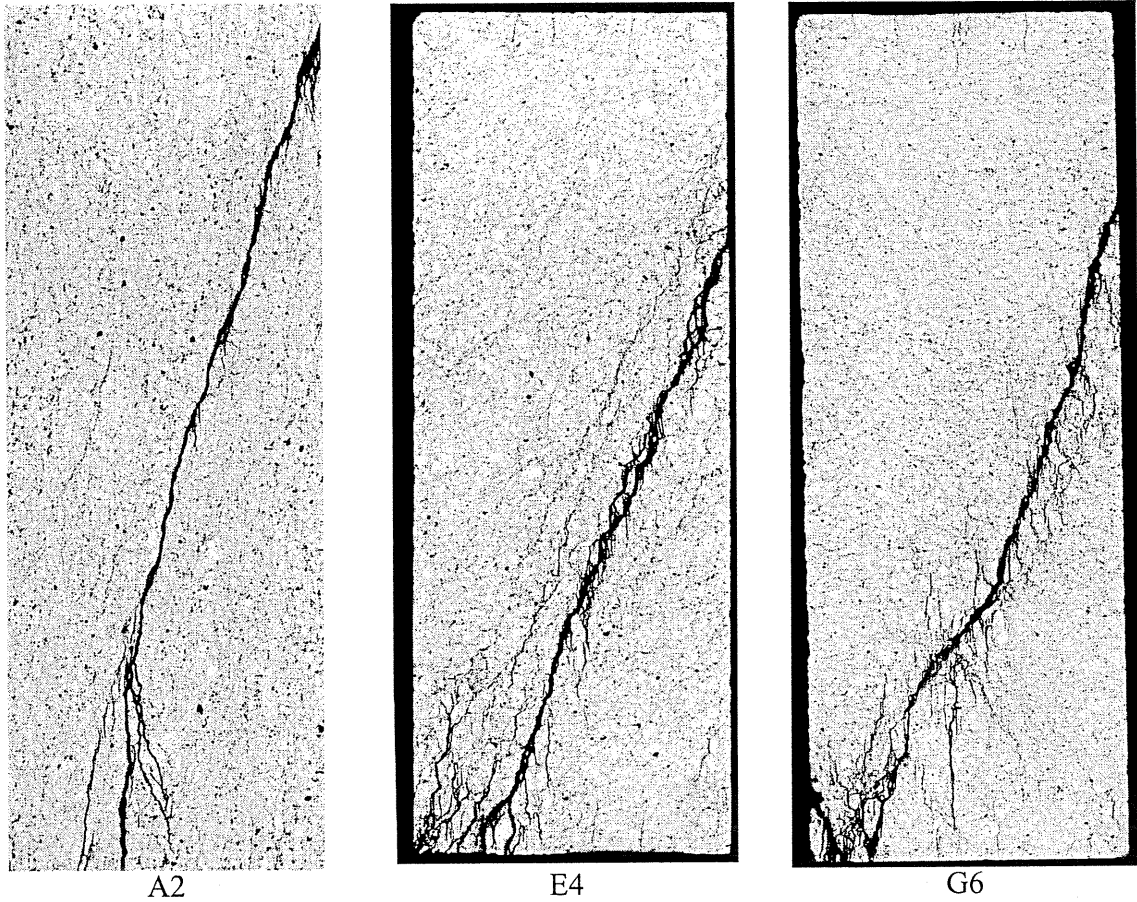
Figure 3.8-3. Autoradiographs of samples A2, E4 and G6.

Comparison of the failure patterns in samples with different orientations show two common features. The main planes of fracture, which eventually split the samples diagonally, have very similar positions and in the case of samples e4 and g6 is almost identical. In this respect, Sample a2 shows a deviation of few degrees in the angle of the fracture plane. The ends of all the samples showed distinct fractures 5 to 10 mm in length parallel to the axis of the sample and the main fracture merged with these fractures.

The main differences between the samples are in the thickness of the main fracture. In the case of Samples e4 and g6 this should actually be called a fracture zone, while in the case of Sample a2 it resembles a single fracture with only a few neighbouring fractures which are not easily visible.

The fracture zone in Sample e4 is composed of a set of parallel fractures which all have a saw-tooth shape. There are two prominent directions, one is parallel to the sample axis and the other is close to the orientation of the schistocity plane. There are neighbouring fractures of same form close to the main fracture zone. It appears evident that a number of potential main fractures existed prior to the formation of the main fracture which split the sample.

The fracture zone in Sample g6 is characterised by a large number of side fractures which are parallel to the axis of the sample and initiate from the main fracture. These

side fractures appear more frequently on one side of the main fracture and it is most likely that they have been formed after the main fracture occurred, probably during the post-peak strength phase of the loading.

3.8.2 Progressive failure

Three similar samples taken from same position in the Research Tunnel with diagonal orientation of schistocity were tested at three different successive loading steps. The loading of the first sample JM1.3 was stopped at a level of about 10% less than the peak strength. The loading of the second sample JM4.3 was stopped at peak strength and the loading of the third sample JM4.2 was stopped at a pre-peak loading level of 5% less than the peak strength. The microfracturing and porosity of the samples were studied by using [14]CPMMA-method (Autio at al. 1999). The porosity images, photoimages and superposition images of the horizontal and vertical sections of the samples are shown in Figures 3.8-3, 3.8-5 and 3.8-7. The corresponding deformation curves are shown in Figures 3.8-4, 3.8-6 and 3.8-8. The superposition image shows the high-porosity reagions seen in the porosity images superimposed on the photoimage of the samples and gives an illustrative presentation of the microfracturing and spatial distribution of porosity with respect to different mineral species.

The result shows that the porisity of the sample increases along the linear part of the stress-strain loading curve. The porosity is located randomly and it is more intense closer to the outer surface of the sample. At a loading point about 10% less than the estimated peak strength there appears to be no actual continuous microfractures (see Figure 3.8-3). The sample fails (the strength starts to reduce) at a point when microfractures coalescence to form continous microfractures which follow the schistosity planes as seen in Figure 3.8-5. As the pre-peak loading is continued, more continous microfractures along the schistosity planes are coalescenced as seen in Figure 3.8-7 which eventually lead to a total loss of strength and failure of sample as seen for Sample E4 in Figure 3.8-2. The failure seems to originate from the sample surface where the porosity is more intense at pre-peak loading and in that respect the failure process is similar to that presented by Moore & Lockner (1995) and Lockner (1993) for Barre granite.

Figure 3.8-4. *Fracturing in sample JM13. Autoradiograph (left), photoimage of rock surface and superposition image (right) showing areas of higher porosity and microfracturing in red colour. Sample diameter 54 mm.*

Figure 3.8-5. *The deformation curve of sample JM13. The peak loading was about 10% less than the peak strength.*

Figure 3.8-6. Fracturing in sample JM43. Autoradiograph (left), photoimage of rock surface and superposition image (right) showing areas of higher porosity and microfracturing in red colour. Sample diameter 54 mm.

Figure 3.8-7. The deformation curve of sample JM43. The loading was stopped at the peak strength.
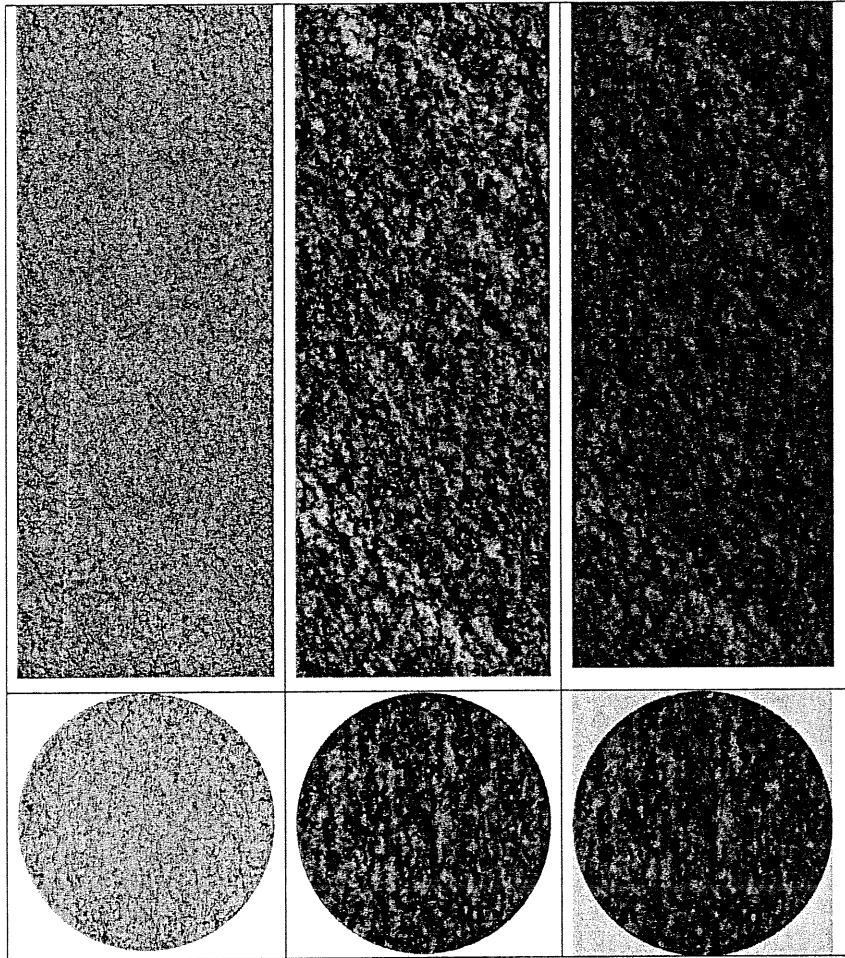
43

Figure 3.8-8. *Fracturing in sample JM42. Autoradiograph (left), photoimage of rock surface and superposition image (right) showing areas of higher porosity and microfracturing in red colour. Sample diameter 54 mm.*
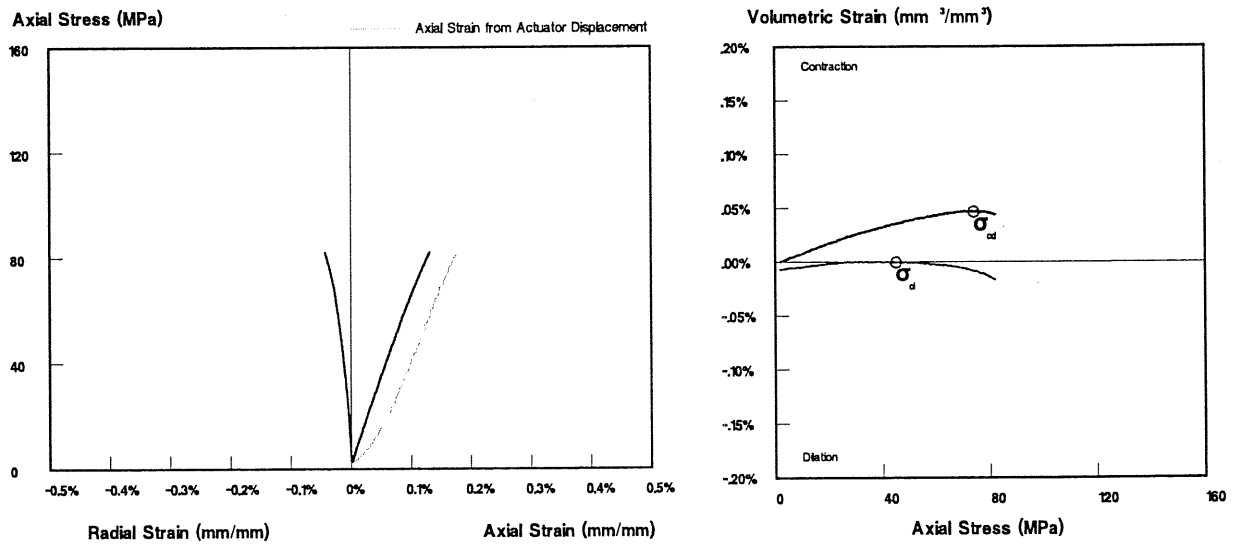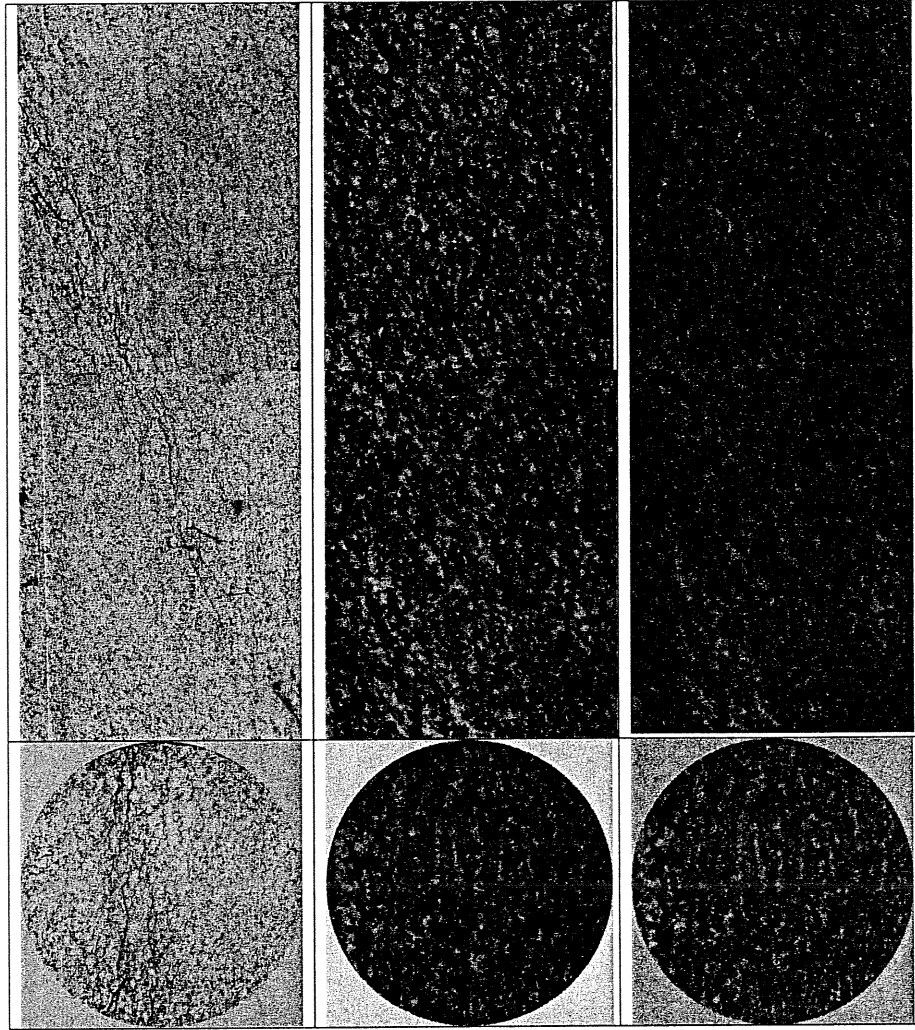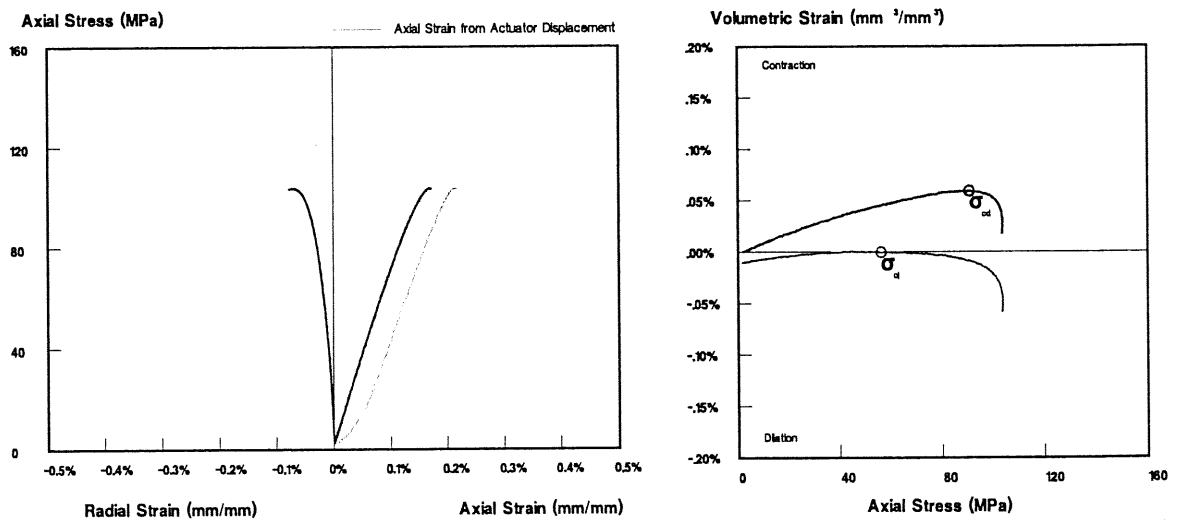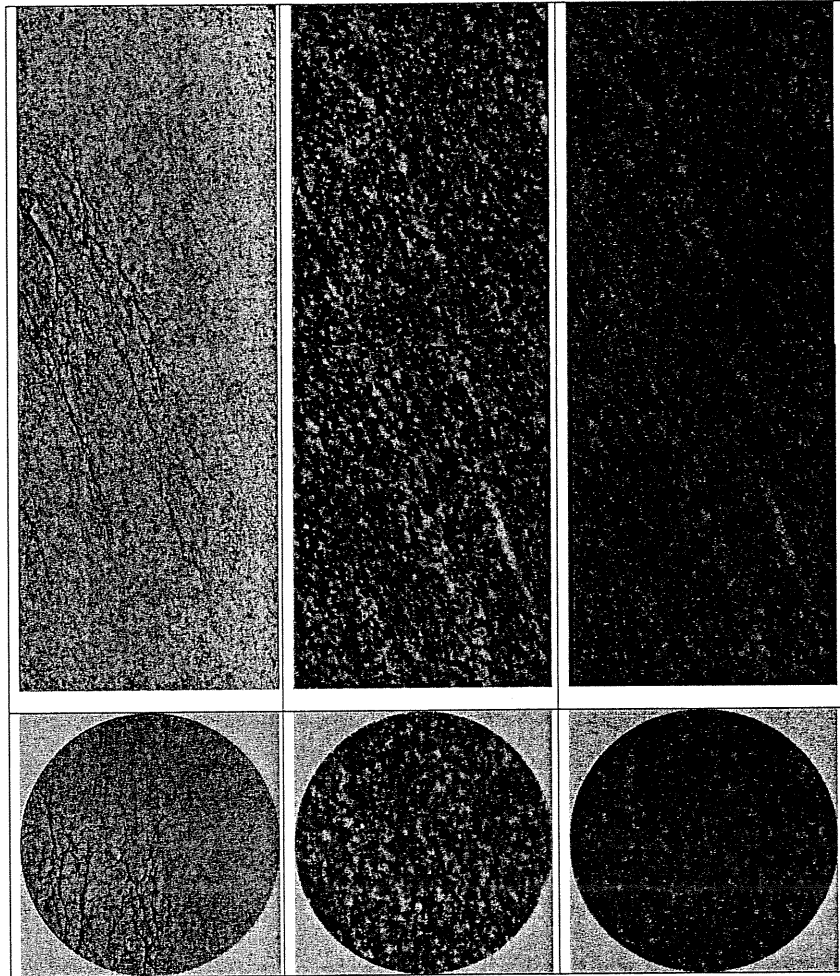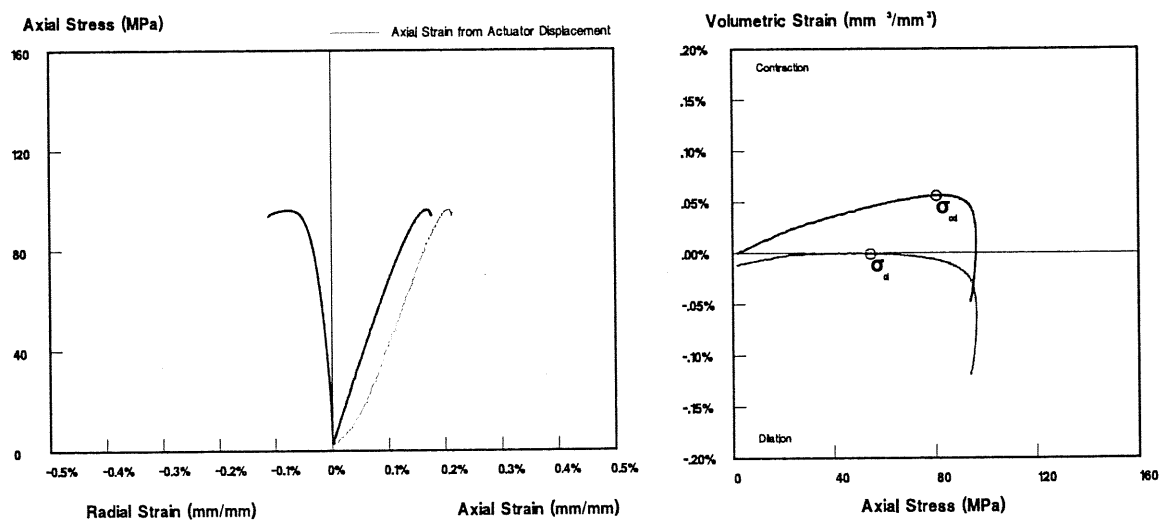

Figure 3.8-9. *The deformation curve of sample JM42. The loading was stopped about at a post-peak level 5 % lower than peak strength.*

3.9 Acoustic emission

3.9.1 Measurement arrangement

The acoustic emissions from two samples of diameters 42 mm and 99 mm was monitored during the compressive test using the equipment described below.

The monitoring system was manufactured by the Physical Acoustic Corporation (PAC). The most important components and features of the measurements system were:

- Four channels
- One wide band piezoelectric transducer (PAC WD), with an operating range of 100 to 1000 kHz
- One 20-1200 kHz bandwidth preamplifier (PAC 1220A) with a 100-1200 kHz band pass filter (PAC 1220A-600B)
- An AE analyser (Model 3104)
- A PC/CPM control/data collection unit (Model 3000).

The AE transducer was positioned on the side of the rock sample as shown in Figure 3.9-1. Details of the measuring technique have been presented by Hakala & Heikkilä (1997).
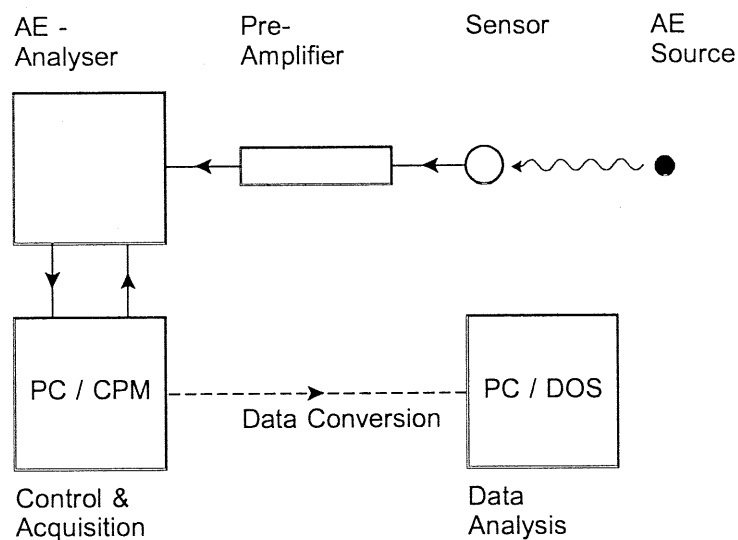
Figure 3.9.-1. Acoustic emission measurement configuration.

The first hit on any channel above the threshold value initiates the count collection time period for a single event. After the dead point all sensors are ready to detect the next event.

During the measurements, the preamplification was set to 40 dB, no analyser amplification was used, the threshold value used to start the recording of an emission

event was 0.1 V and the dead time (i.e. the time after which recording of next event can take place) was set to 0.5 ms.
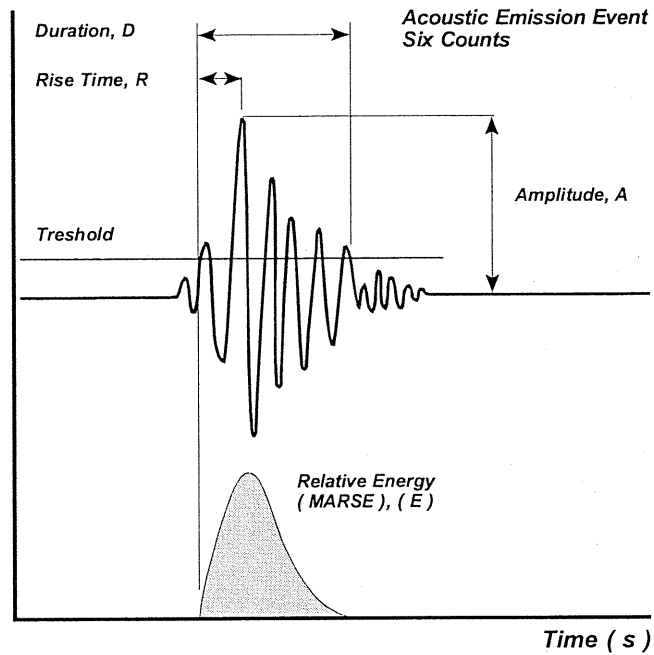
Figure 3.9-2. Parameters describing an AE event (Pollock 1989).
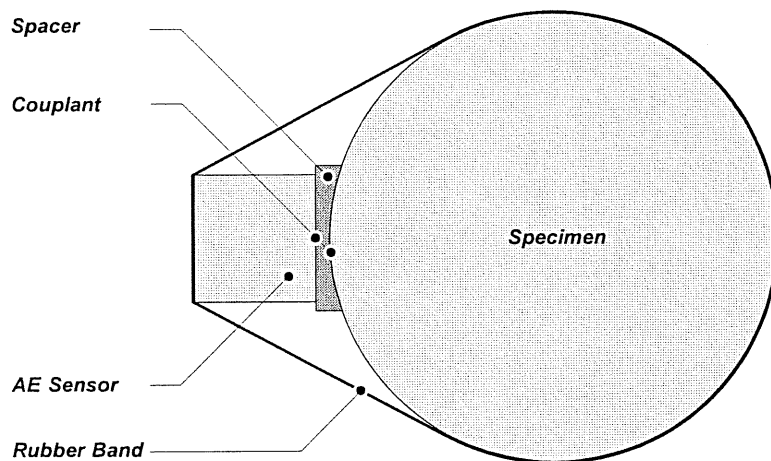
Figure 3.9-3. Cross-section of the rock sample and position of the AE sensor (Hakala&Heikkilä 1997).

3.9.2 Results

The results of the measurements in terms of the energy of acoustic emission (AE) and counts (see Fig. 3.9-2 for an explanation) with respect to axial strain are shown in Figures 3.9-4 to 3.9-7.
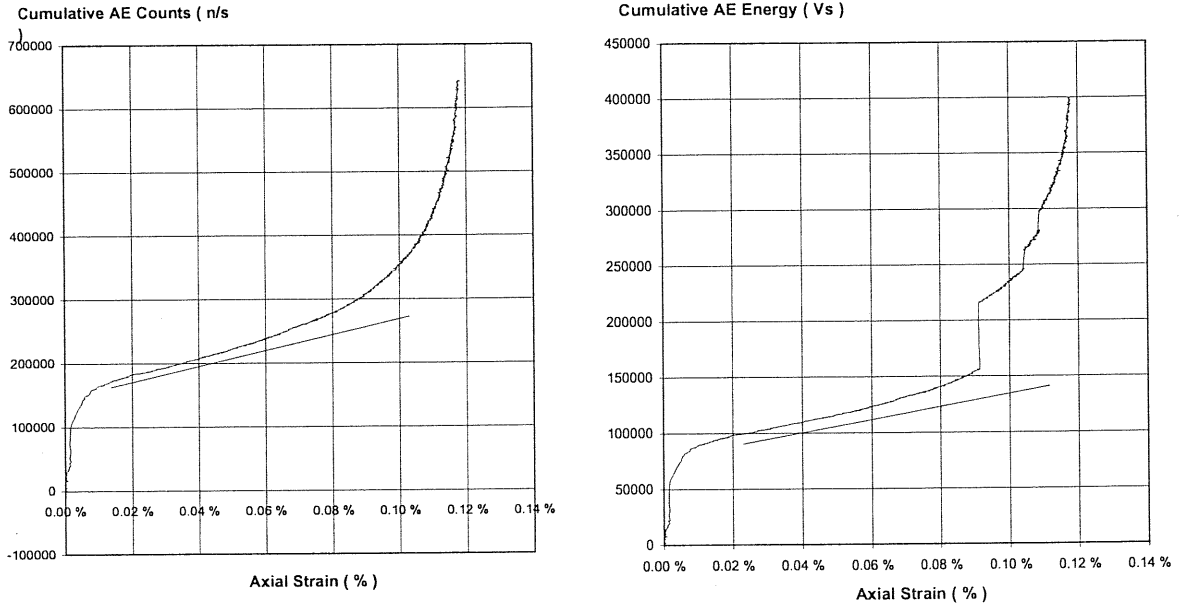
Figure 3.9-4. *Cumulative AE counts (left) and AE energy (right) with respect to axial strain (the straight line is for reference only). Sample OL-TT-D6-42, diameter 42 mm.*
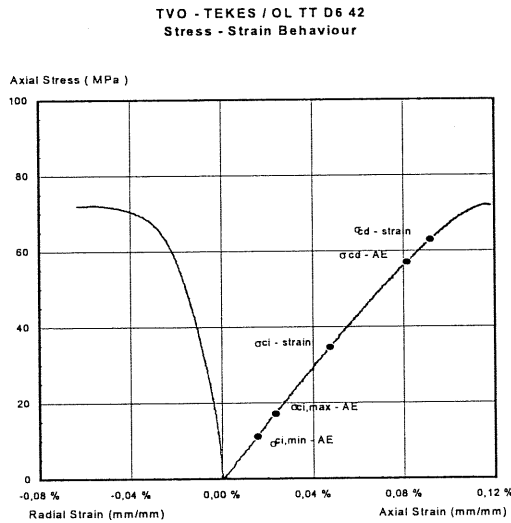
Figure 3.9-5. *The stress-strain curve corresponding to the data presented in Fig. 3.9-4. The estimated lowest and highest values based on AE for σ_{ci} and σ_{cd} are also shown.*
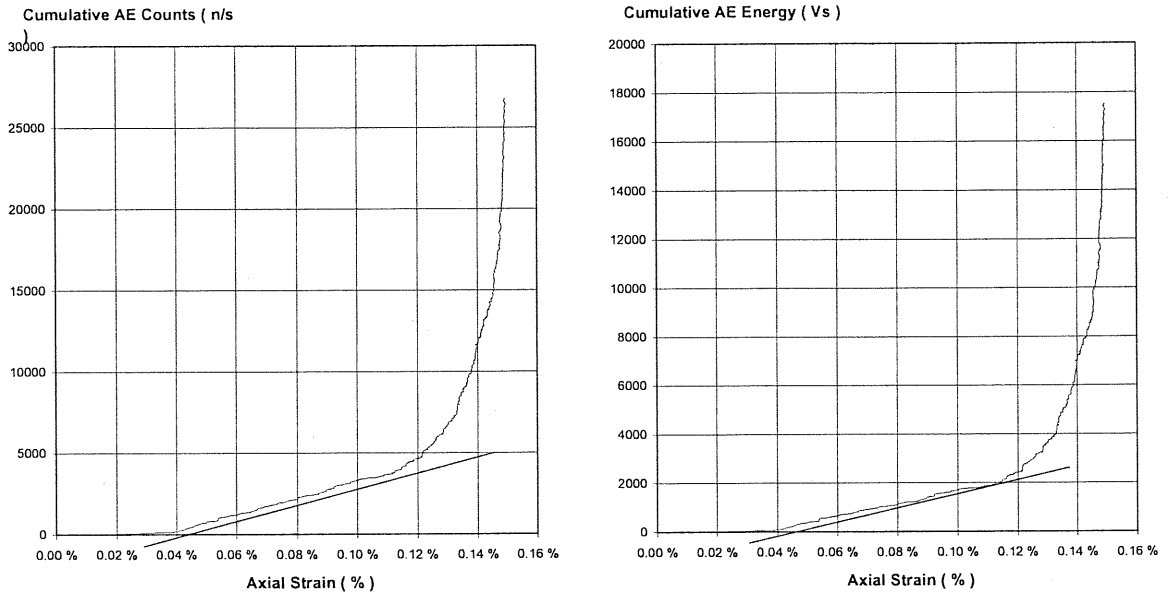
Figure 3.9-6. Cumulative AE counts (left) and AE energy (right) with respect to axial strain. Sample OL-TT-D6-100, diameter 99 mm (the straight line is for reference only).
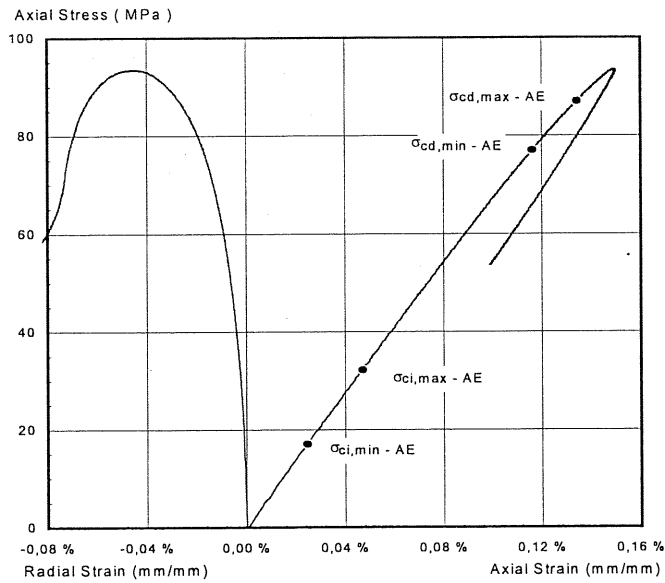
Figure 3.9-7. The stress-strain curve corresponding to the data presented in Fig. 3.9-6. The estimated lowest and highest values based on AE for σ_{ci} and σ_{cd} are also shown.

The results of the tests show that the deformation of the sample and the activation of microfractures which cause acoustic emissions start at low levels of stress and increase gradually, culminating at a point in the region of unstable crack growth and lasting until the sample fails.

3.10 Conclusions

The values obtained for compressive strength, Young's Modulus and Poisson's Ratio from the gneissic tonalite in the Research Tunnel at Olkiluoto show significant orientation. The strength of rock is about 40% higher when the schistocity is oriented parallel to the sample axis than when it is oriented diagonally. The measured rock mechanical properties are not significantly affected by the sample size provided that the direction of the schistocity plane in the sample is not parallel to the axis of the sample.

The degree of saturation has an effect on sample strength. If the sample is totally saturated the compressive strength is clearly lower, but no clear difference was discerned between totally-dry samples and test room-conditioned samples (30-40% of pore space filled with water).

The loading rate has some effect on the sample strength. The reduction of loading rate by two orders of magnitude from 0.75 MPa/s to 0.0075 MPa/s reduced the compressive strength less than 10%.

The deformation of rock samples with different schistocity orientations is shown in Figure 3.10-1. Buckling only occurred in some samples where the schistocity was perpendicular to the sample axis or parallel to it. The failure patterns and cracking depend on the orientation. The microfracturing starts from the sample sample surface. At a loading about 10 % less than the peak strength there is increased random porosity which is more intense in a zone close to the surface. At peak strength there are distinct continous microfractures which evidently nucleate from the sample surface and follow the schistosity planes in the sample. After peak strength a school of parallel fractures are formed in the sample accompanied by a rapid drop in strength.
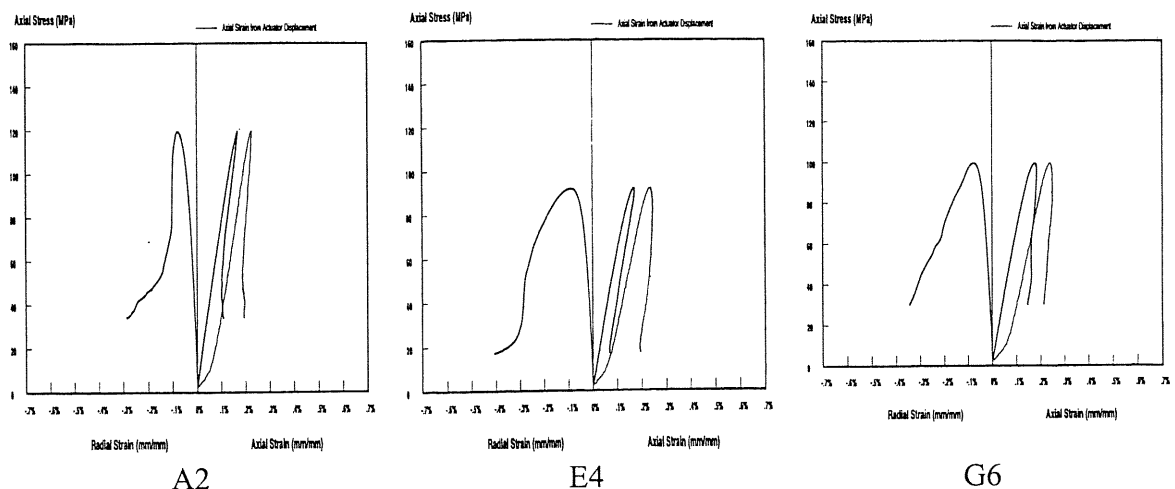

Figure 3.10-1. Stress-strain curves corresponding to three different orientations (Samples A2/ 15°, E4/45° and G6/80°).

4 THE STATE OF STRESS IN THE ROCK SURROUNDING THE FULL-SCALE DEPOSITION HOLES

4.1 General

One factor which has an influence on the design of the in-situ failure test are the existing in-situ stresses. In-situ stress measurements were made in the VLJ-repository prior to and during the excavation phase, but, no stress measurements have been made in the Research Tunnel itself. The decision was therefore made to conduct stress measurements close to the planned location for the experimental set-up for the in-situ failure test. The results obtained from these new secondary stress measurements would also be compared with previous measurements of in-situ stress.

4.2 Measurement technique and procedure at the Research Tunnel

4.2.1 Test arrangement

Over-coring technique was selected for the measurement of stresses around the full-scale deposition hole. The principle of the method was to core a 100 mm diameter hole, install strain gages on the surface of the drilled hole, over-core the smaller 100 mm diameter hole using a larger 200 mm diameter hole and measure the strains caused by the over-coring and the relaxation of stresses. The state of in-situ stress was then calculated using the measured strains and the elastic properties of the rock. The over-coring stress measurements were carried out in August 1997. A detailed description of the field work is given in a test report by Hakala (1998).

Measurements were carried out in the experimental full-scale deposition hole 2, which is the middle of the three full-scale holes. The depth of the section used for measurements was 3.7 m below the tunnel floor (Fig. 4.2-1). The holes used for measurements were cored in all cardinal and intermediate directions, a total of eight holes. An additional smaller diameter hole was drilled for wiring purposes as shown in Figure 4.2-2. The three strain gauge rosettes were placed in each measurement hole at a depth of 40 mm from the surface of the full-scale hole. Two sets of additional strain gauge rosettes were placed at depths of 95 mm and 150 mm in measurement hole JM3, which was oriented to the East.
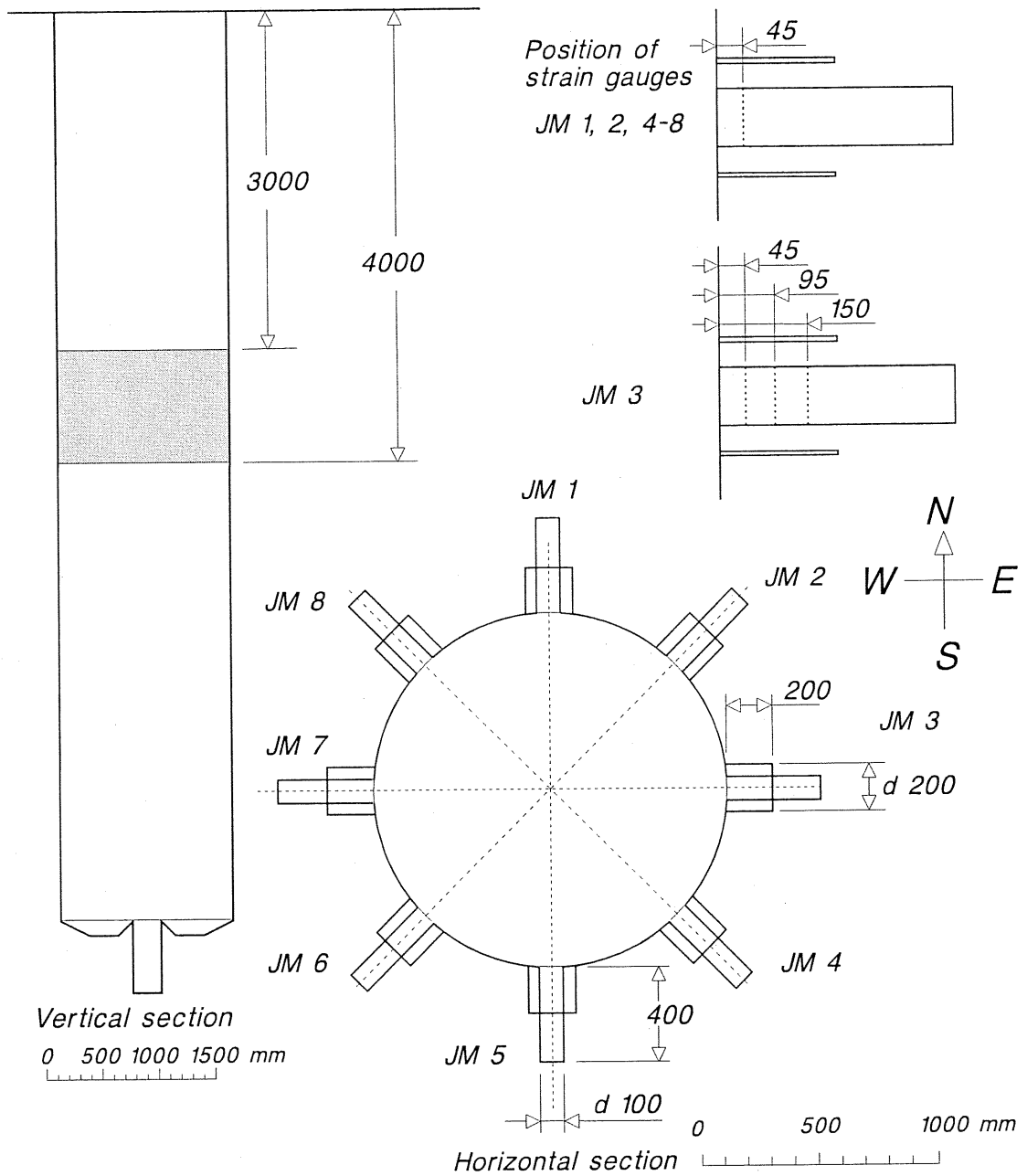
Figure 4.2-1. Position of the measurement section, the locations and dimensions of measuring holes JM1-JM8 and position of strain gauges in full-scale deposition hole 2.
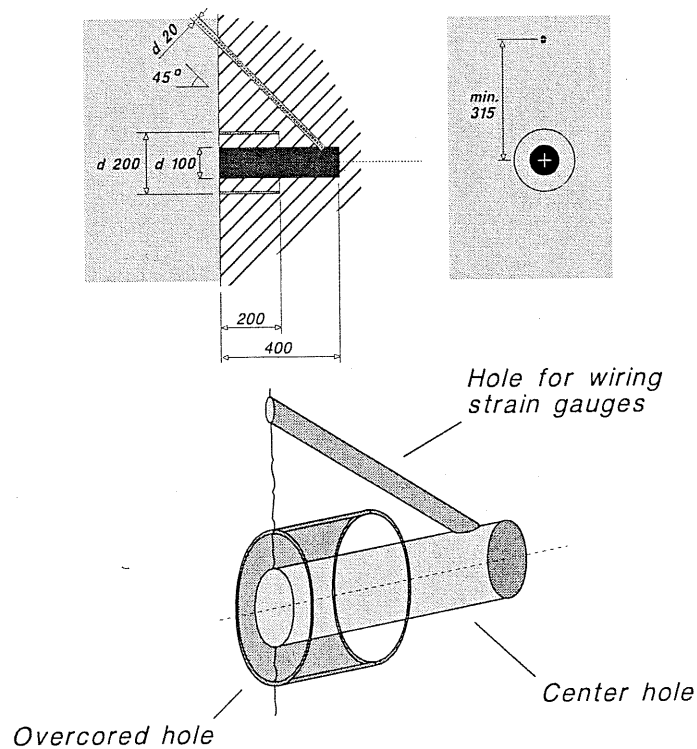
Figure 4.2-2. Geometry of the measurement holes.

4.2.2 Coring and overcoring

A small water-cooled portable coring machine of type Weka DK-42 was used to core the holes. This type of equipment has previously been used for sampling and a description of it can be found in (Autio et al. 1995).

The centre measurement holes were cored approximately two weeks prior to the over-coring. Before any measurements were made, an additional hole to accommodate the electric wiring was drilled to the bottom of the hole. Before over-coring took place, the holes were dried, the strain gage rosettes were glued in position and the hole was plugged to prevent the entry of any water.

The over-coring process took between 14 and 26 minutes. The time required to reach the depth of the strain gauges (5 cm) was approximately 10 minutes. After the over-coring process was complete, the plug was removed from the mouth of the hole and monitoring of the strain gages was continued for a period of 8 to 24 hours. After monitoring period the cores were break loose and the last strain reading was recorded.

4.2.3 Installation of strain gauges

The main steps in the installation of the strain-gauges (see Figure 4.2-3) were:
- Drying of the rock surface
- Mechanical removal of loose dust and dirt
- Final cleaning of the surface using 1.1.1 -tricloroethane
- Installation of the strain gauge rosettes using a special tool
- Heating of each test point with a hot air gun to speed up the resin hardening process
- Removal of the installation tool.
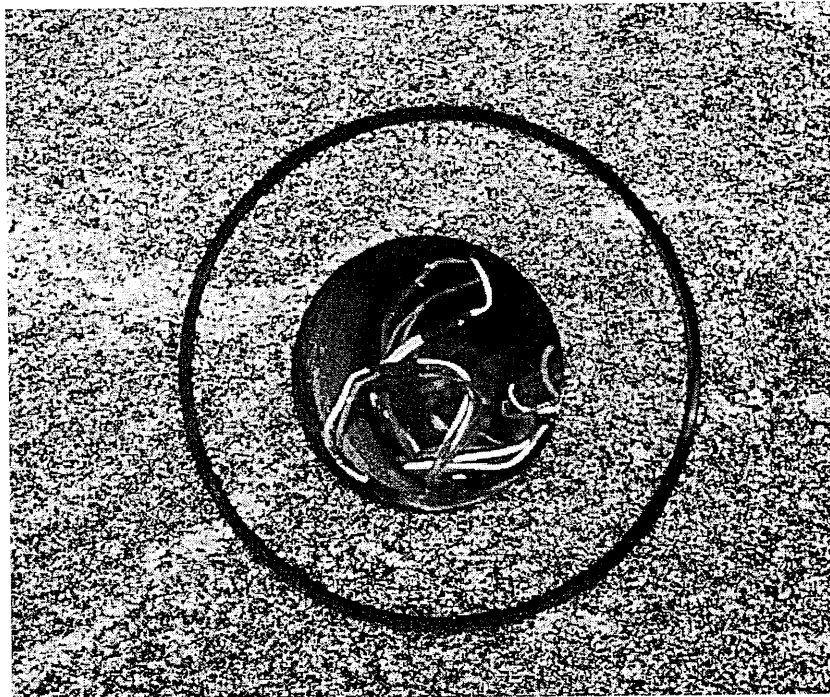
Figure 4.2-3. Measurement hole with strain gauges installed after over-coring.

4.2.4 Data registration

The signals from the strain gauges and the temperature sensors (PT-100) were passed to a computer controlled HBM-UPM 100 Multipoint Measuring Unit which was coupled to an Advantech IPC-610 Industrial PC. Monitoring of the measurement data was carried out by the computer

A maximum of 54 strain gauges and 4 temperature transducers were measured in a single cycle.

In order to maximise the measurement accuracy the following set up was used:
- a long integration time 100 ms (strain gages) or 20 ms (temperature sensors)
- four-wire measuring technique

- 600 Hz carrier frequency amplifier
- shielded transducer cables.

The four-wire measuring technique minimises possible errors caused by temperature changes in the transducer cables and contact points.

Strain and temperature was monitored during the over-coring process for a period of at least 20 minutes in five second cycles. Data from each of the eight tests was saved in a separate file. Measurements were then carried out for an extended period using a reduced cycle. The final measurements were taken after loosening the hollow rock core.

4.3 Stress around the deposition holes

4.3.1 Measured strains

Identification and labelling of different strain gauges in figures is shown in Figure 4.3-1. The time-strain curve of holes JM1, JM2, JM7 and JM8, which cover 180° of the measurement periphery and the coring data, are shown in Figures 4.3-2 and 4.3-3. The time-strain curves for hole JM3 at three different depths from the surface of the full-scale deposition hole are shown in Figure 4.3-4. The measurement error was assessed as being ±12 um/m on the basis of the reference measurements. The final strain values were recorded after the over-cored part had been detached. The strains measured before and after detaching the cores were parctically the same the difference being in the range of the signal noise which implies that there were no significant residual stresses in the samples after overcoring which was expected in the case of measurement hole JM3 at strain gauge depth 150 mm.

NO	Position/ Direction
1	0°/Tangential
2	0°/45°
3	0°/Axial
4	90°/Tangential
5	90°/45°
6	90°/Axial
7	225°/Tangential
8	225°/45°
9	225°/Axial
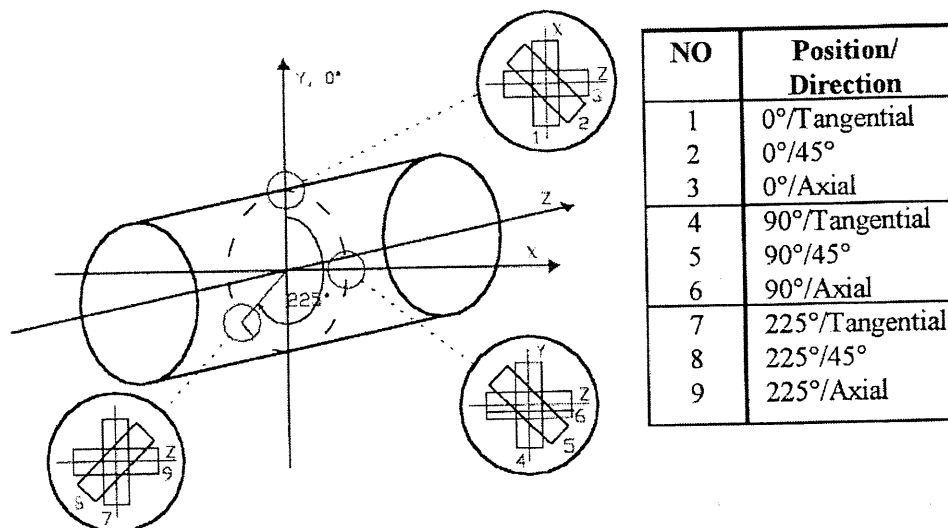
Figure 4.3-1. Identification and labelling of strain gauges.

VLJ-TT JM1 North

VLJ-TT JM2

Figure 4.3-2. *Time-strain curve for hole JM2 (bottom) and JM1 (top), and coring data. A stands for Axial and R for Tan (Tangential) in Figure 4.3-1.*
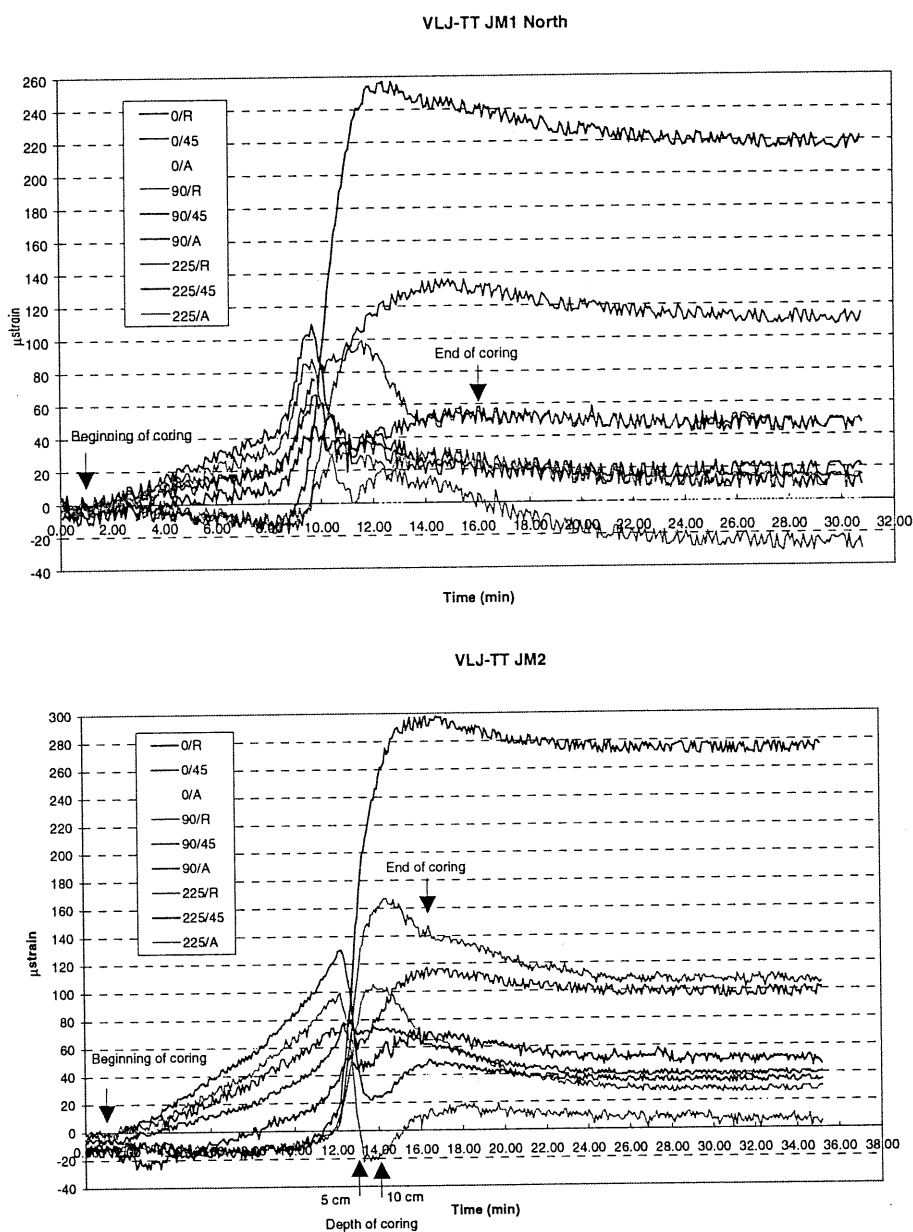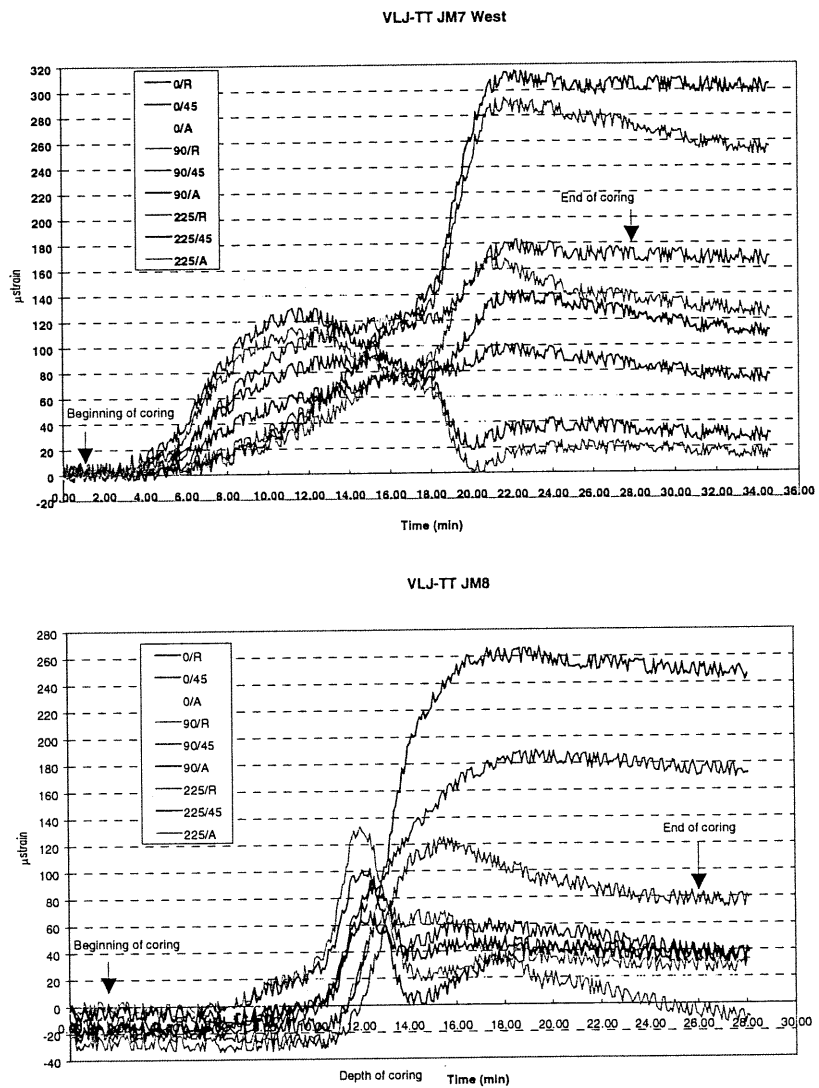
Figure 4.3-3. Time-strain curves for hole JM8 (bottom) and JM7 (top), and coring data. A stands for Axial and R for Tan (Tagential) in Figure 4.3-1.
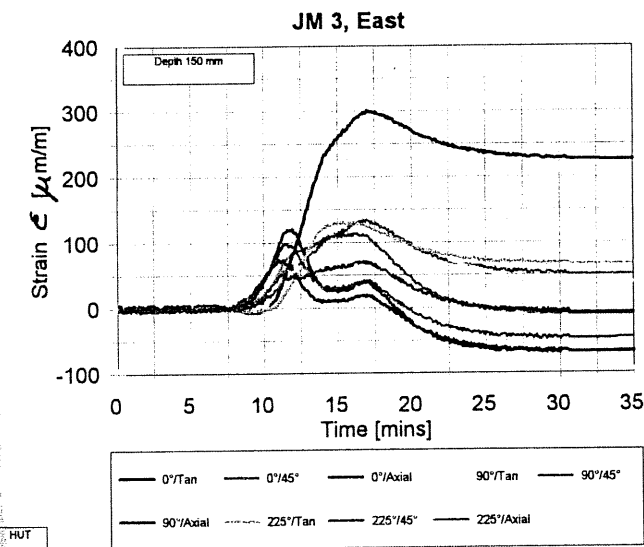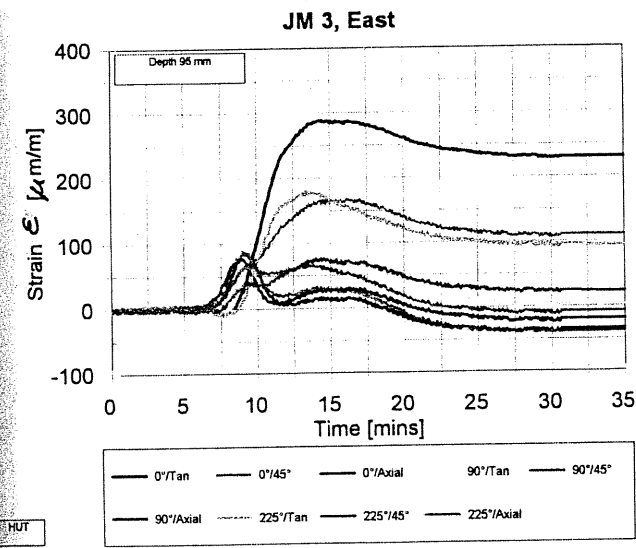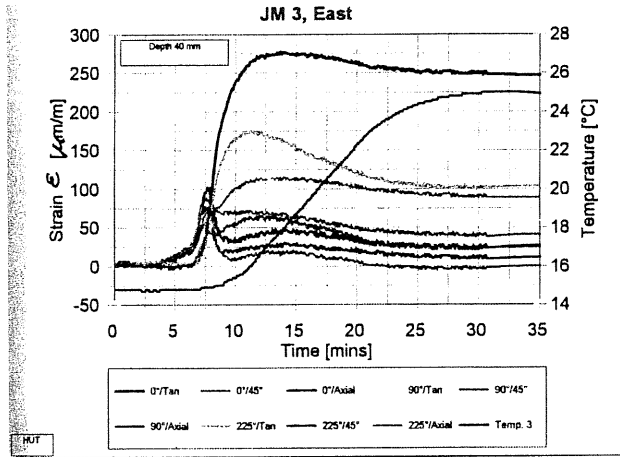
Figure 4.3-4. *Time-strain curve for hole JM3 at depths of 40 mm (top), 95 mm (middle) and 150 mm (bottom). See Figure 4.3-1 for labelling of strain gauges.*

4.3.2 Stresses around experimental full-scale deposition hole

The measured strains were converted to corresponding strains by using Kirsch's equations, these are found in most rock mechanics text books such as (Jaeger&Cook 1979). The input data required was the measured strain, Young's modulus E and Poisson's ratio. The strain value was taken 30 minutes after the coring had started, since by this time the coring process was complete and the strains had settled to stable levels. The Poisson's ratio used was 0.29. The following three alternative values, representing the range determined for Young's modulus E in Chapter 3.4, were used in the conversion: A) 61 GPa, B) 66 GPa and C) 80 GPa. The stresses were also calculated using the peak strain value taken from the measurements and E of 66 GPa. These values are labelled as D) values in the graphs. A summary of the all the stresses calculated using different Young's modulus values and Poisson's ratios for the gneissic tonalite are presented in Table 4.3-2. A summary of the stresses calculated using average values for the gneissic tonalite, i.e. E=66 GPa and υ=0.29, are presented in Table 4.3-2. A summary of all the results using the other values, is shown in Figure 4.3-5.

The actual measured largest tangential stress σ_{1max} adjacent to the surface of the full-scale hole corresponding to the measured average rock mechanical properties (E=66 GPa, Poisson's ratio 0.29) was 10 MPa, and the minimum primary tangential stress σ_{1min} was 6 MPa. The range for the largest tangential stress was from 9 to 12 MPa depending on the Young's modulus used. The range for the smallest tangential stress was from 5 to 8 MPa.

The maximum tangential stress component is found in holes which are in sector 225-270° (clockwise from north), with the maximum value being probably close to 250° on the basis of the symmetry. This implies that the direction of the largest principal stress component, which is in a direction perpendicular to that, is in a sector which is close to 160°.

The calculated primary principal stresses in different measurement holes were close to horizontal and tangential to the surface of the full-scale hole with a deviation of 5 - 23 gons (corresponding to 4.5-23.4°) from the horizontal depending on the measurement position and input values, see Fig. 4.3-6. The horizontal deviation between the plane tangential to the full-scale hole and the direction of the main principal stress was 3-18 gons (corresponding to 2.7 - 16.2°). The intermediate stress σ_2 and minimum stress component σ_3 were of same magnitude. In some holes the intermediate stress σ_2 was directed close to perpendicular to the surface of the full-scale hole and the minimum stress component σ_3 is directed upwards, parallel to the axis of the full-scale hole. In some holes the directions were vice versa as seen in Table 4.3-2.

The stress values become smaller as the distance from the surface of the full-scale hole grows larger, as can be seen for hole JM3 in Table 4.3-3 and Figure 4.3-7. The main stress component is 31% larger at the depth of 40 mm from the surface of the full-scale hole than at the depth of 95. The ratio between the σ_1 and σ_3 stress components is 1.4-3.7 at depth of 40 mm from the surface of the full-scale hole. The ratio is smallest in the same positions where the main stress component is the largest.

Table 4.3-1. Calculated main components of stress around full-scale experimental deposition hole 2. Values A, B and C have been calculated using the post-peak strain value at a time of 30 minutes after completion of coring. The peak strain has been used for the calculation of D value. The Poisson's value used in all the calculations was 0.29 and the Young's moduli for values A, B and C were 61, 66 and 80 GPa respectively.

Stress components		σ_1				σ_2				σ_3				σ_1/σ_3	
Hole	Direction [°]	A	B	C	D	A	B	C	D	A	B	C	D	A&B&C	D
JM 1	0	5.5	6	7.2	7.9	3.4	3.7	4.5	5.3	1.5	1.6	2	3.1	3.7	2.5
JM 2	45	7.9	8.6	10.4	9.8	4.2	4.6	5.6	6.6	3.1	3.4	4.1	5.6	2.5	1.8
JM 3	90	7.4	8	9.7	9.1	3.9	4.2	5.1	6.4	3.4	3.6	4.4	5.9	2.2	1.5
JM 4	135	7.3	7.9	9.6	9.3	4.3	4.6	5.6	6.4	2.7	2.9	3.6	4.6	2.7	2.0
JM 5	180	7	7.5	9.1	9.1	3.5	3.8	4.6	5.9	2.1	2.3	2.8	3.6	3.3	2.5
JM 6	225	8.4	9.1	11	10.3	4.6	5	6.1	6.5	4	4.3	5.2	6.3	2.1	1.6
JM 7	270	9.2	10	12.1	10.7	6.4	6.9	8.4	7.7	6	6.4	7.8	7.6	1.5	1.4
JM 8	315	6.6	7.1	8.6	8.7	4.1	4.4	5.4	5.9	2	2.1	2.6	4.5	3.3	1.9
JM 1	360	5.5	6	7.2	7.9	3.4	3.7	4.5	5.3	1.5	1.6	2	3.1	3.7	2.5

Table 4.3-2. Calculated main components of stress around full-scale experimental deposition hole 2. σ_H is the largest horizontal stress component, σ_h the smallest and σ_v is the vertical component. The directions of the largest stress components (clockwise from north) and the dip (deviation from horizontal) of σ_1 is also shown. The Poisson's value used in the calculation was 0.29 and the Young's moduli 66 GPa respectively (B values in Table 4.3-1).

Measured stresses [MPa] and orientations [°] around full-scale deposition hole 2 at depth 40 mm.

Hole	Direction	σ_1	σ_2	σ_3	σ_H	σ_h	σ_v	$\theta\sigma_1$	$\theta\sigma_H$	$\theta\sigma_{1dip}$
JM 1	0° (360°)	6	3.7	1.6	5.8	3.7	1.8	86	85	13
JM 2	45°	8.6	4.6	3.4	8.3	4.6	3.7	152	151	13
JM 3	90°	8	4.2	3.6	7.6	4	4.2	190	9	18
JM 4	135°	7.9	4.6	2.9	7.9	3.9	3.7	28	27	6
JM 5	180°	7.5	3.8	2.3	7.1	2.6	3.9	80	77	20
JM 6	225°	9.1	5	4.3	9	4.9	4.6	138	139	10
JM 7	270°	10	6.9	6.4	9.9	6.9	6.6	178	178	7
JM 8	315°	7.1	4.4	2.1	7	4.3	2.4	30	29	7

Young's modulus E = 66 Gpa, Poisson's ratio υ=0.29.
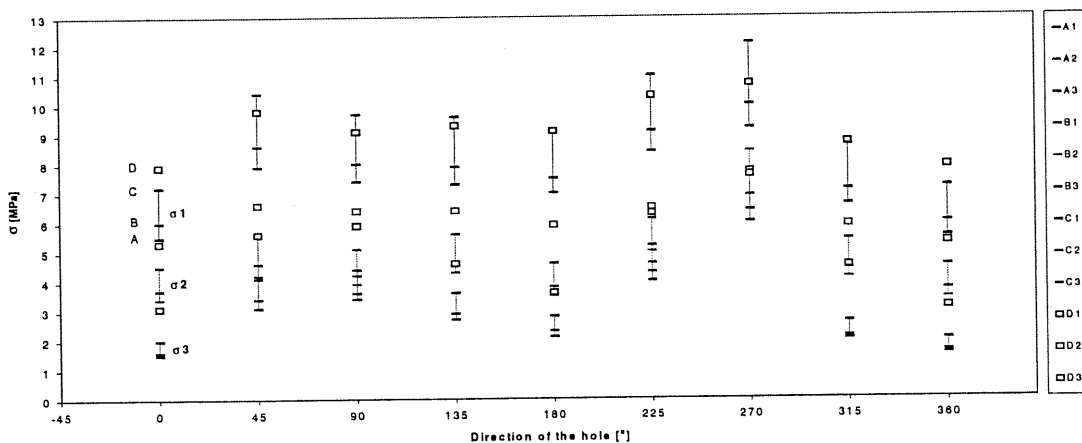
Figure 4.3-5. Graph showing the main stress components shown in Table 4.3-1 as a function of the direction and position of the measurement hole for four different input values. See Table 4.3-1 for an explanation of the A, B, C and D values.
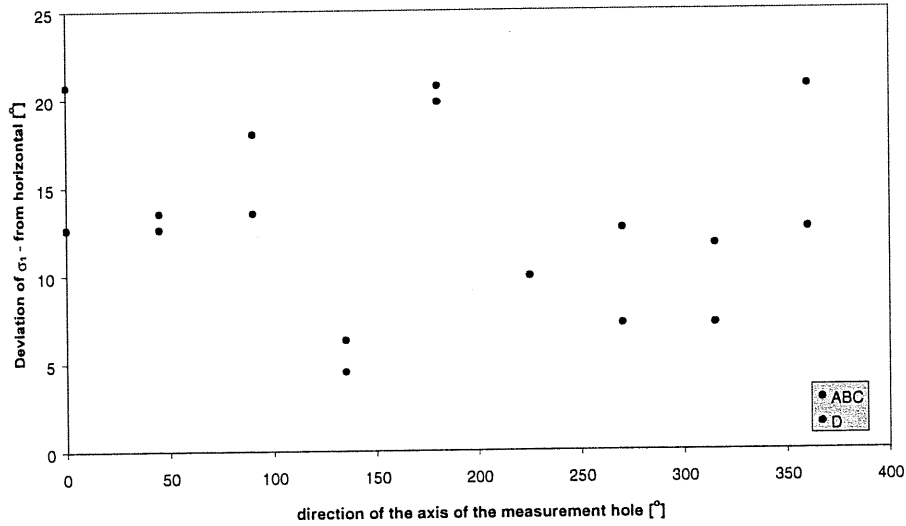
Figure 4.3-6. The deviation of the main principal stress σ_1 from horizontal with respect to the direction of the measurement hole. Note that σ_1 is close to tangential to the surface of test hole. See Table 4.3-1 for explanation of the A, B, C and D values.

Table 4.3-3. The main stress components in measurement hole JM3 at depths of 40 and 95 mm from the surface of the full-scale hole.

Measurement hole JM3, direction of axis 90°

depth [mm]	σ_H	σ_h	σ_v	σ_H/σ_v
40	7.6	4	4.2	1.8
95	6	0.1	1.8	3.3
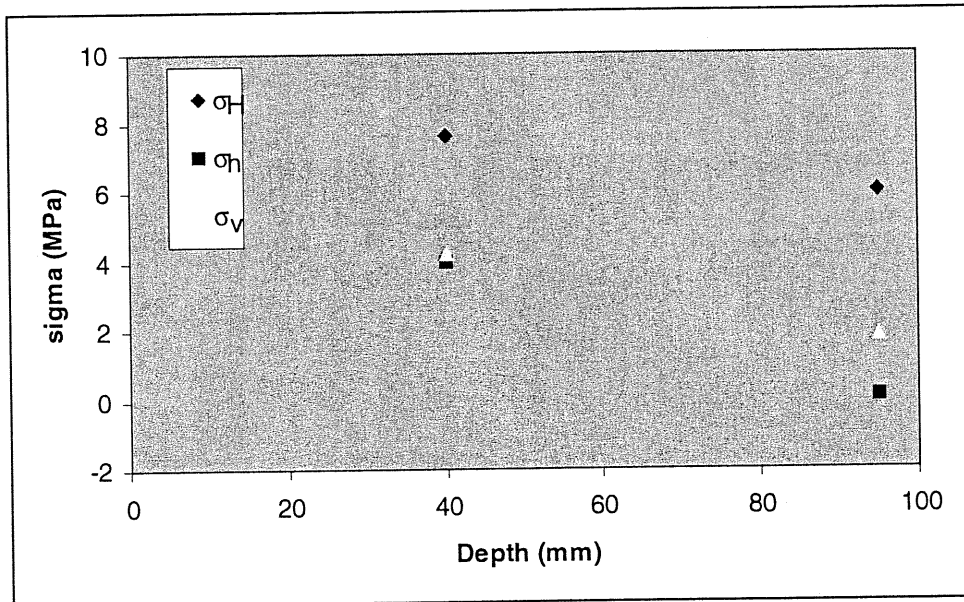
Figure 4.3-7. The main stress components in measurement hole JM3 at depths of 40 and 95 mm from the surface of the full-scale hole.

4.4 Estimate of in-situ stresses

The measured state of stress in the vicinity of the full-scale deposition holes differs from the in-situ stress because it is affected by both the full-scale hole and the existence of the Research Tunnel situated directly above it. The in-situ stresses can be estimated if the tangential stresses around the full-scale hole at the measuring depth are known by using Kirsh's equation for the tangential stress around a circular 2D opening and by modeling.

The state of stress around the full-scale holes was also modelled by using numerical 3DEC code (Itasca 1994) to include the effect of the tunnel above the full-scale holes and the three dimensional geometry. For practical purposes, the geometry of the Research Tunnel (width 7 m and height 7.5 m) was simplified to more closely resemble the proposed deposition tunnel (width 3.3 m and height 4.6 m). For this reason the largest tangential stresses around the full-scale hole given by modelling should, in reality, be slightly larger.

The largest tangential stress at the surface of the full-scale hole given by modelling is presented in Figure 4.4-1 with respect to distance from the tunnel floor. The largest and smallest tangential stresses around the full-scale holes estimated by modelling at the depth of the stress measurements were 12 and 8 MPa respectively. The in-situ stresses used in modelling for σ_H, σ_h and σ_v were 5.1, 2.5 and 1.9 MPa respectively. Since the input values used for tangential stress are at the upper boundary the real in-situ sresses should be equal or less than these in-situ stress values. The distribution of principal stresses is shown in Figure 4.4-2. The real stresses adjacent to the surface of the full-scale hole should be slightly (0.5-1.0 MPa) higher than those obtained by modelling because the element model used for the surface section was quite coarse.
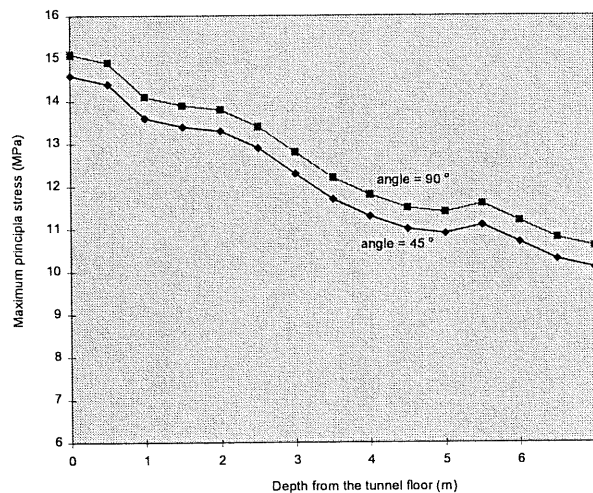
Figure 4.4-1. *Maximum tangential principal stress σ_l (horizontal) around a full-scale deposition hole with respect to depth from the tunnel floor. Estimates are based on numerical modelling using 3DEC-code. The two angles shown (90° and 45°) were used to study the sensitivity of the model and specify the angle between the maximum principal stress (horizontal) and the tunnel axis.*
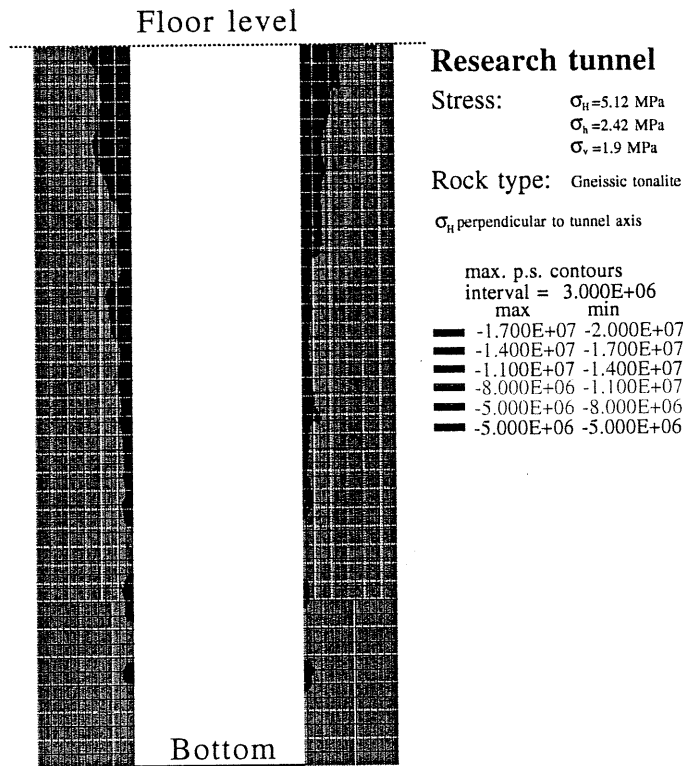
Figure 4.4-2. Contour plot of the maximum principal stress (tangential) around full-scale deposition holes. The angle between the principal in-situ stress and the tunnel axis is 90°. The largest tangential stress is 12 MPa.

The in-situ stresses were estimated by using Kirsh's equation for the tangential stress around a circular 2D opening. The main and intermediate principal in-situ stresses shown in Figure 4.4-3 were calculated using Kirsch's equations on the basis of the largest measured and smallest tangential stresses, these being 10 MPa and 6 MPa respectively at a depth of 4 cm from the surface of the full scale hole. The calculated magnitude of the principal in-situ stress was 4.6 MPa and the calculated magnitude of the intermediate principal stress was 3.6 MPa. The estimate is simple and does not include the effect of Research Tunnel and assumes that the length of the full-scale hole is infinite.

Stress around full scale experimental deposition holes

Largest tangential stress component
(10 MPa at 4 cm)

Smallest tangential stress component
(6 MPa at 4 cm)

In situ stress $\sigma 1$ and $\sigma 2$ are 4.6 and 3.6 MPa respectively

Tangential stresses [MPa]

Distance from the surface of the full-scale hole [m]

● StH-u
● Sth-u
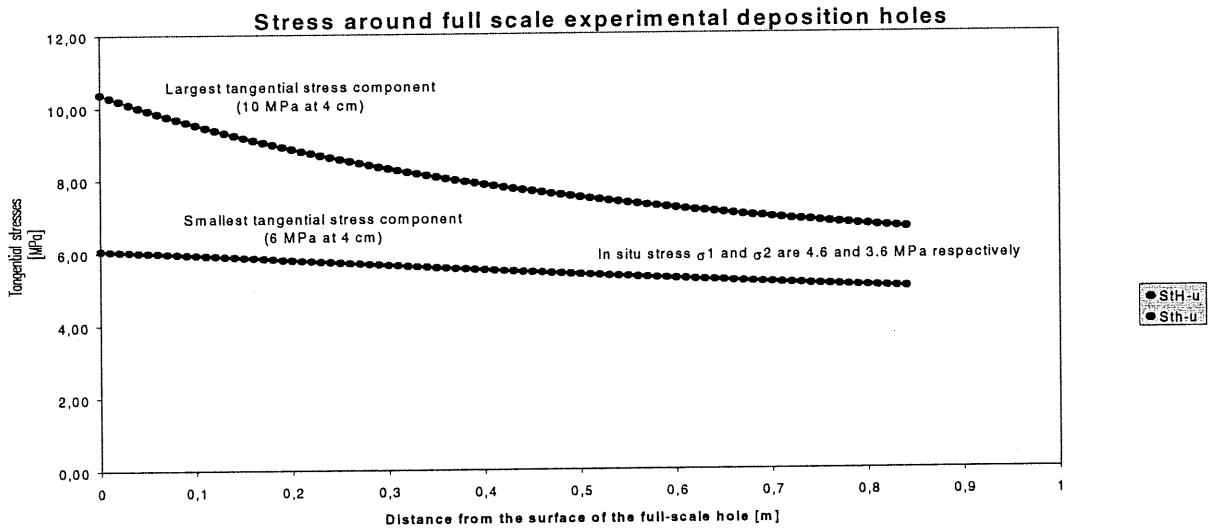
Figure 4.4-3. Largest and smallest tangential stresses around the full-scale holes with respect to depth. The curves have been calculated using Kirsch's equations and the measured maximum and minimum tangential stresses.

18°

N

σ_H

4,6

3,6

σ_h

Research tunnel
Horizontal section
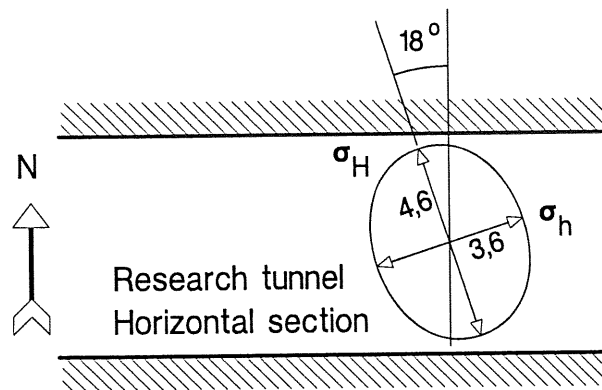
Figure 4.4-4. Horizontal section of the Research Tunnel showing estimate of the direction and magnitude of the primary in-situ stresses after the stress measurements presented here. The earlier estimate was presented in Figure 6.3-2.

The modelled maximum in-situ stresses σ_H and σ_h were 5.1 MPa and 2.5 MPa respectively. The corresponding in-situ stresses given by Kirsch'c equations were 4.6 MPa and 3.6 MPa respectively. The real in-situ values are likely to be closer to the values given by Kirch's equations since the input values for modelling overestimated the in-situ sresses.

According to stress measurements (Kuula & Johansson 1991, Nykyri et al. 1991) carried out before the construction of the VLJ-repository and the Research Tunnel, the state of in-situ stress at the VLJ-repository and in the area of the Research Tunnel is low. Measured values of the maximum in-situ stress averaged from 5 to 6 MPa at the

level of the repository. A value of 5.1 MPa was estimated for the σ_H stress (horizontal) and 2.4 MPa for the σ_h stress (horizontal) (Kuula & Johansson 1991). The calculated vertical stress (σ_v) of 1.9 MPa was assumed to be caused by gravity (Kuula & Johansson 1991). Results obtained from the monitoring of rock displacement during and after construction of the repository were consistent with these results (Nykyri et al. 1994).

The measured magnitudes of the principal and intermediate in-situ stresses are quite consistent with the earlier results (Kuula & Johansson 1991, Nykyri et al. 1991), even though the calculated ratio based on Kirsh's equations of 1.3 between the two stresses was lower than the ratio of 2.1 achieved earlier.

The main difference in the new set of results compared to those obtained previously is in the direction of the main principal stress shown in Figure 4.4-4 which differs by 65° from the earlier determination. The difference is not significant since the earlier estimation of stress orientation at low stress levels based on bore-hole measurements is inaccurate. There may also be local deviations in the stress field which may effect the results.

The measured behaviour of the magnitude of the principal main stress with respect to the distance from the surface of the full-scale hole shown in Figure 4.3-6 is consistent with the results of the calculation shown in Figure 4.4-3.

According to the cross-sectional contour plots obtained by modelling, the stress conditions around a full-scale hole are close to two dimensional at a depth of 3.5 to 4.5 m from the tunnel floor. At this range of depths neither the Research Tunnel nor the bottom of the full-scale hole appear to have any significant effect on the stresses adjacent to the surface of the full-scale hole.

5 EXPANDING AGENT

5.1 General

The stress around the centre hole is created by filling the slots shown in Figure 2-1 with an expanding agent. The fact that the swelling of the expanding agent is restricted means that pressure is generated. The expanding agent used is sold in Finland under two different commercially-registered names - Betonamit and Demex and is commonly used to break smaller amounts of rock in situations where blasting is not feasible. The usual practice is to drill vertical holes and then pore the expanding agent into the holes. Details of the expansion pressure in different sizes of holes is given in the manufacturers instructions (see Figure 5.1-1).

Since the behaviour of the expanding agent in other geometries than cylindrical holes was not know, a test was carried out to verify that the required level of pressure can be achieved using a planar slot. Three different thicknesses of expanding layer i.e. 30, 40 and 50 mm were tested.

The minimum pressure required to cause the failure in the central hole of the text configuration was estimated using the modelling techniques described in Chapter 6. These indicated that an expansion pressure of 50 MPa should be adequate to result in failure.

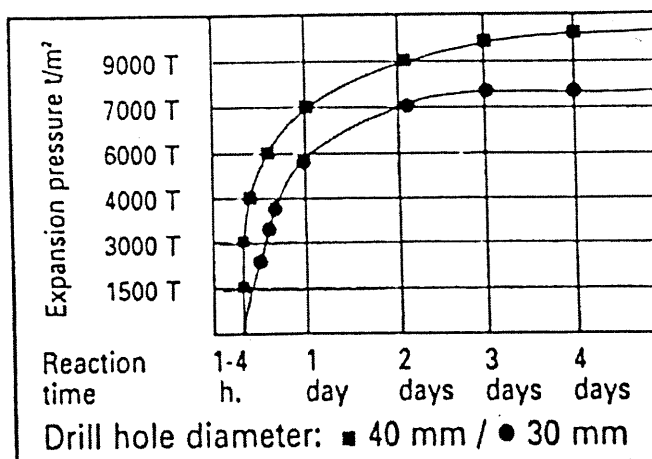Graph of the Expansion Pressure and Time of Reaction.

Figure 5.1-1. Expansion pressure of Betonamit with respect to reaction time for different diameters of hole (according to Betonamit International AG, Liechtenstein).

5.2   Description of the expanding agent

The expanding agent chosen for use in this study was Demex produced by Optiroc. The working material is calcium oxide CaO, which produces calcium hydroxide $Ca(OH)_2$ when it reacts with water. The reaction also causes expansion of the mixture and the release of thermal energy. The speed of the reaction is temperature dependent, and to achieve adequate pressure development, the initial temperature of the object to be broken should be between 0 and 20°C. In colder conditions Demex is ineffective, in warmer conditions where the temperature of the reaction exceeds 90°C the water in the mix begins to boil.

Demex is delivered in powder form and it is used by mixing it with water. The correct quantity of water is 23% of the weight of Demex used. When breaking rock or concrete the mixed material is poured into boreholes which should have a diameter of between 25 and 45 mm. The recommended hole diameter is 35 mm. With larger boreholes the danger of overheating increases. According to the manufacturers instructions supplied with Demex, the maximum pressure developed is greater than 75 MPa after three days (see Figure 5.2-1).
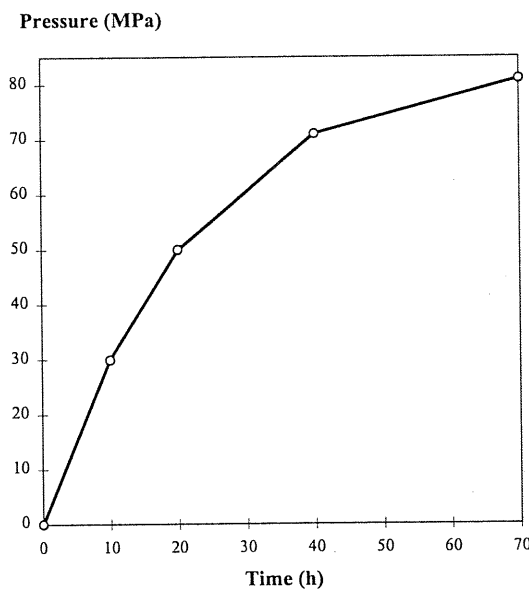
Figure 5.2-1. Pressure developed by Demex expanding agent (Optiroc 1996).

5.3   Experimental technique and procedure

Tests to determine the expansion pressure developed by Demex were carried out using a MTS 815 Rock Mechanics testing system and a cylinder-piston arrangement (Figure 5.3-1) at the Laboratory of Rock Engineering in Helsinki University of Technology. The displacement of the piston was monitored by measuring the displacement of the actuator in the MTS system. The radial strain on the cylinder was calculated from the displacement of the lateral chain extensometer positioned on the side of the cylinder (Figure 5.3-2).
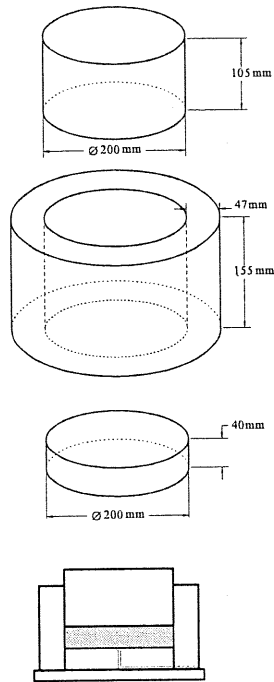
Figure 5.3-1. The cylinder-piston system.
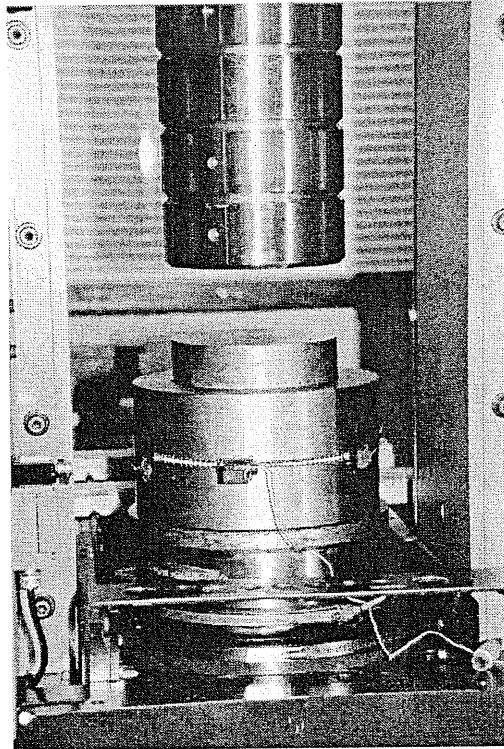
Figure 5.3-2. The lateral chain extensometer on the side of the cylinder.

Temperatures in several locations in the cylinder (Figure 5.3-3) were measured using a PICO TC-08 system which is a combined thermocouple amplifier and analog-to-digital converter. The room temperature was also recorded. Temperature data was collected using a PicoLog data logging program and a PC.
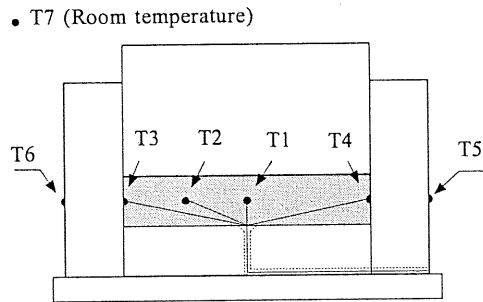
Figure 5.3-3. Arrangement of the thermocouples.

The actuator displacement was controlled in a way that the displacement of the piston was equivalent to the displacement of the rock surfaces of the slots to be used in the in-situ test (Figure 5.3-4). The values for displacement were obtained from the results obtained using 3D numerical modeling as presented in Chapter 6. The actuator of the testing system was lifted at 2.5 or 5.0 MPa intervals to follow the modelled pressure-displacement behaviour. The deflection in the testing system was determined by testing an aluminum sample with a known Young's modulus. The stiffness of the system was calculated to be 1.304 MN/mm and was found to be greater than the displacement of rock. Before the test, the mixture of water and Demex powder and the piston cylinder arrangement were cooled to an initial temperature of 7°C which corresponds to the average in-situ temperature of the rock mass at Olkiluoto.
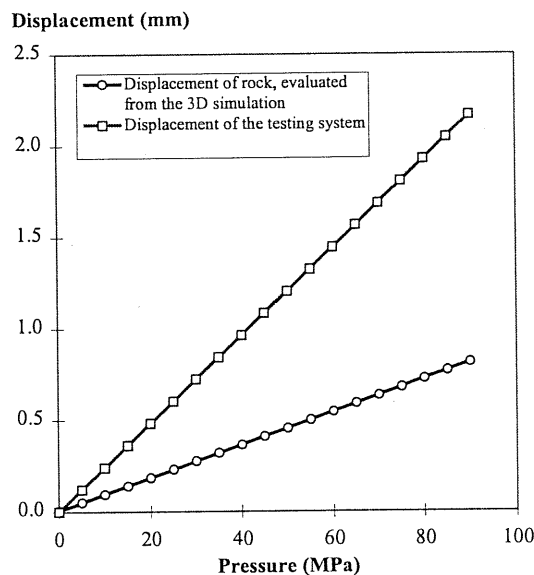
Figure 5.3-4. Displacement of the testing system and displacement of the rock.

5.4 Swelling of the expanding agent

5.4.1 Pressure

The first test was executed twice with a 30 mm thick layer of Demex. The pressure development and the radial strain are presented in Figures 5.4-1 and 5.4-2 where a) and b) refer to the two different tests. Time t in the figures starts from the mixing of the Demex with water. The negative values of the radial strain curves indicate extension and positive compression. Similar results were obtained in both tests.
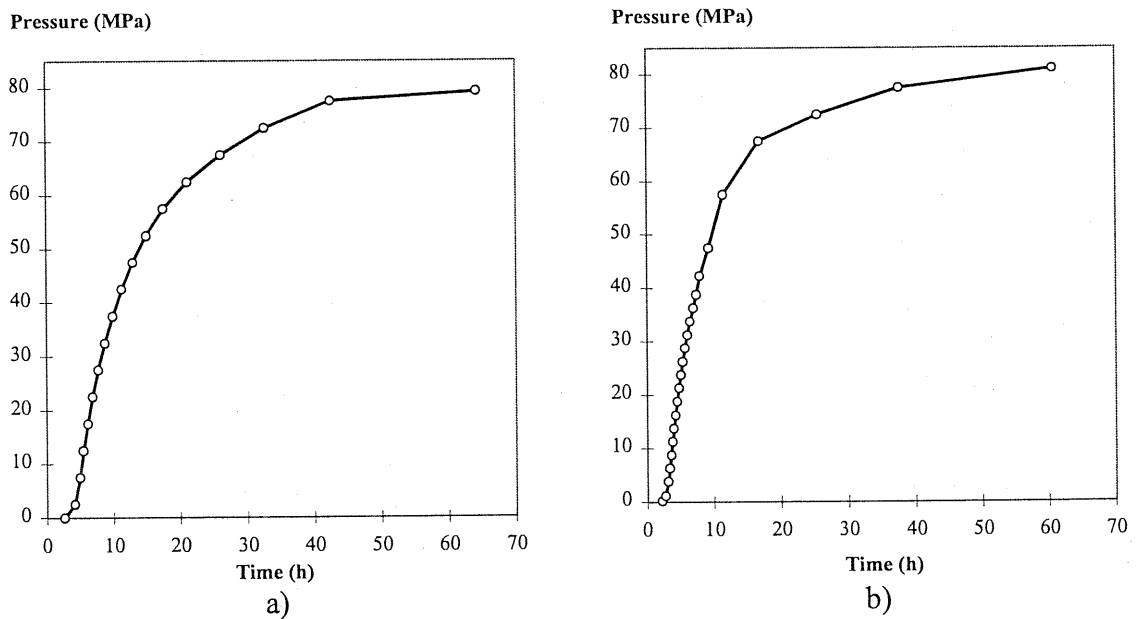
Figure 5.4-1. Pressure development of 30 mm layer of expanding agent Demex. 2 tests
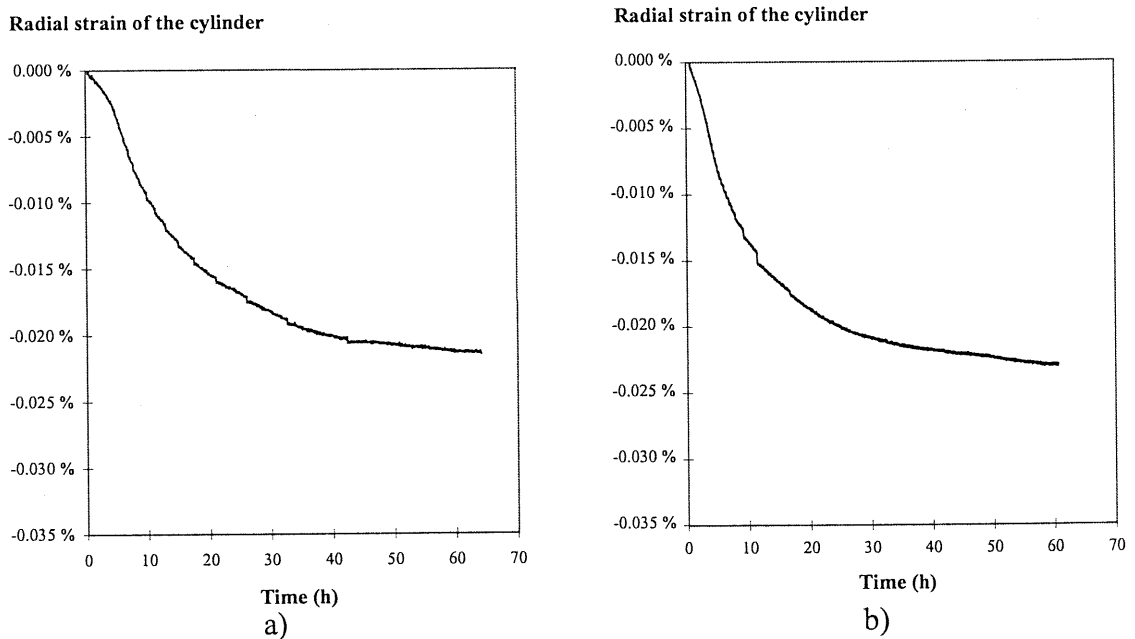
Figure 5.4-2. Radial strain on the cylinder using a 30 mm layer of Demex expanding agent. Negative values indicate extension (two tests)

When a 40 mm layer of Demex was used, measurement of the pressure development shown in Figure 5.4-3 was terminated at 81 MPa because the loading capacity of the testing system is limited to 2600 MN and pressure that had been achieved was known to exceed the requirement for the in-situ test. After reaching 81 MPa the force was held constant. The test using a 53 mm thick layer of expanding agent failed because the temperature rose above the boiling point of water.
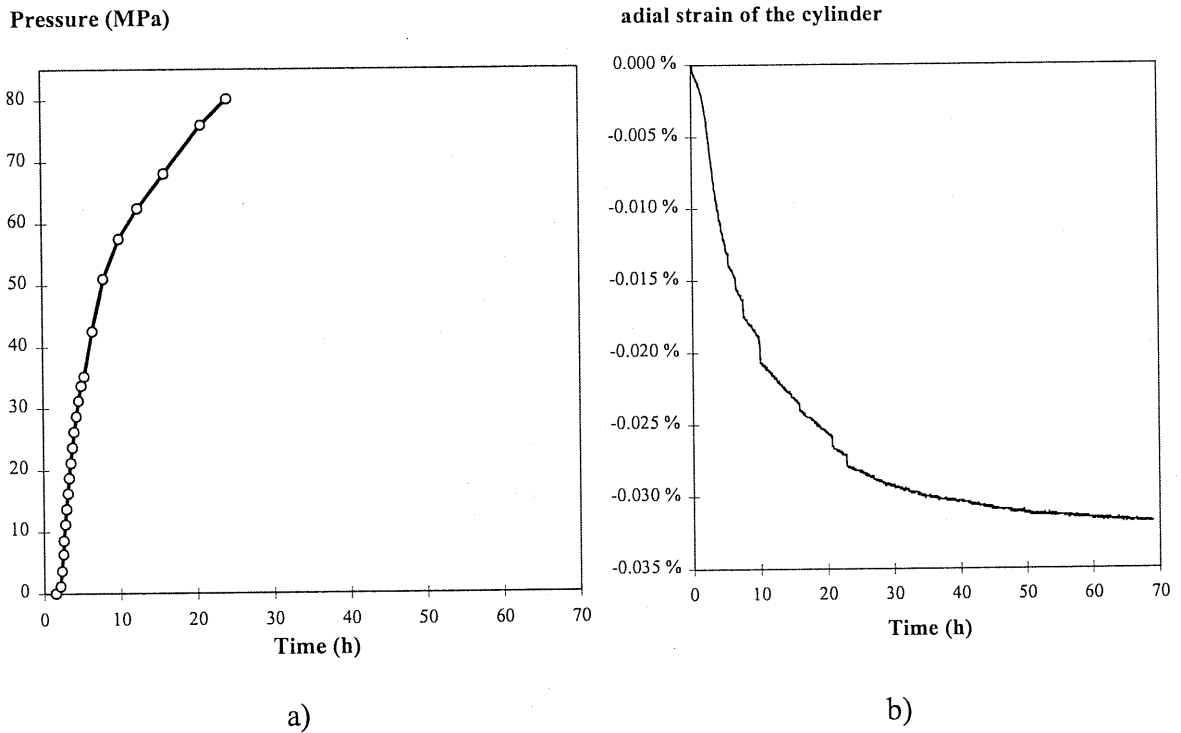
Figure 5.4-3. *Pressure development a) and radial strain b) on the cylinder with a 40 mm layer of Demex expanding agent. Negative values indicate extension.*

5.4.2 Temperature

A significant amount of thermal energy is released when calcium oxide CaO reacts with water to produce calcium hydroxide $Ca(OH)_2$. During testing, the temperature at different positions in the layer of expanding agent were measured using thermocouples as shown in Figure 5.3-3. Temperatures in the expanding agent are shown in Figures 5.4-4, 5.4-5 and 5.4-6 for 30, 40 and 53 mm layers of expanding agent respectively.

The temperature inside the 30 mm layer of Demex stayed below 35°C in the centre of the layer of expanding agent, whereas the temperature at the centre of the 40 mm layer of Demex rose slightly above 45°C. When the thickness of the layer was increased from 40 to 53 mm the temperature at the centre of the expanding layer rose rapidly above 300°C. Once the water in the mix had boiled, the increase in temperature halted.
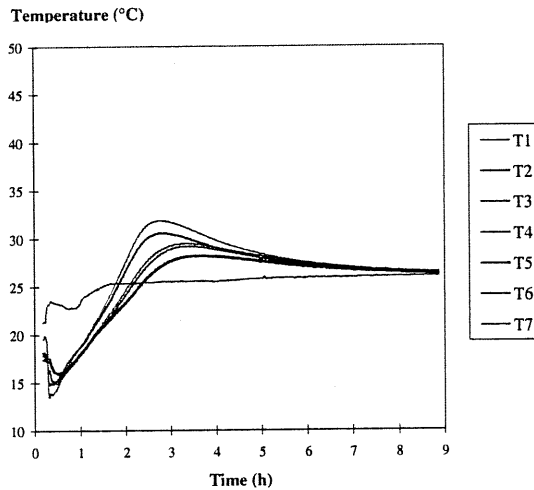
Temperature (°C)

Figure 5.4-4. Temperatures in separate locations in the cylinder in the test using a 30 mm layer of Demex. The location of thermocouples T1- T6 is shown in Figure 5.3-3. The thermocouple T7 measured the room temperature.
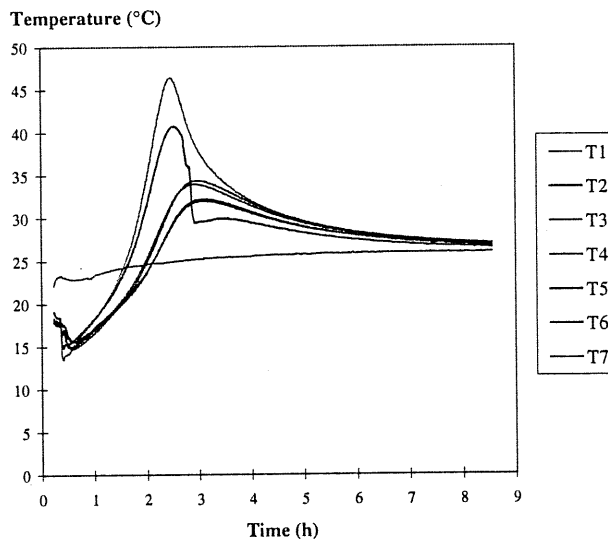
Temperature (°C)

Figure 5.4-5. Temperatures in the test using a 40 mm layer of Demex.
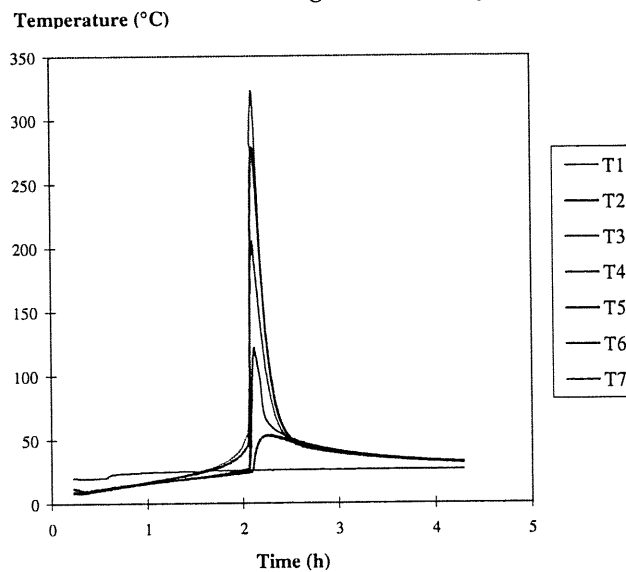
Temperature (°C)

Figure 5.4-6. Temperatures in the test using a 53 mm layer of Demex.

5.5 Sources of errors

The thermal conditions in the in-situ test differ from those of the laboratory tests. The initial cooling of the cylinder-piston system and the Demex powder/water mixture to rock temperature temporarily lowers the temperature of the mixed expanding agent and the temperature of the cylinder-piston system returns to room temperature in 1-2 hours. In the in-situ test, the cooling effect will last longer and the expansion-time behaviour of the expanding agent during the in-situ test is likely to differ from the behaviour observed in the laboratory. It is probable that the cooling will have a greater effect on the time dimension of the expansion process than on the actual achievable expansion pressure.

As there is some variation in the quality of Demex from different manufacturing lots material from a single manufacturing lot was used for this study. The manufacturer measures the pressure development with Demex using the "Bomb method". Examples of the measured differences in performance of separate lots are shown in Figure 5.5-1. The two lower curves are caused by a variation in the chemical composition of Demex which, according to the manufacturer, should no longer be a problem. Differences in the expansion versus time behaviour are clear and for this reason, it was decided to avoid the problems resulting from variations in quality between different manufacturing lots by either using material from the same lot or from mixture of different lots.
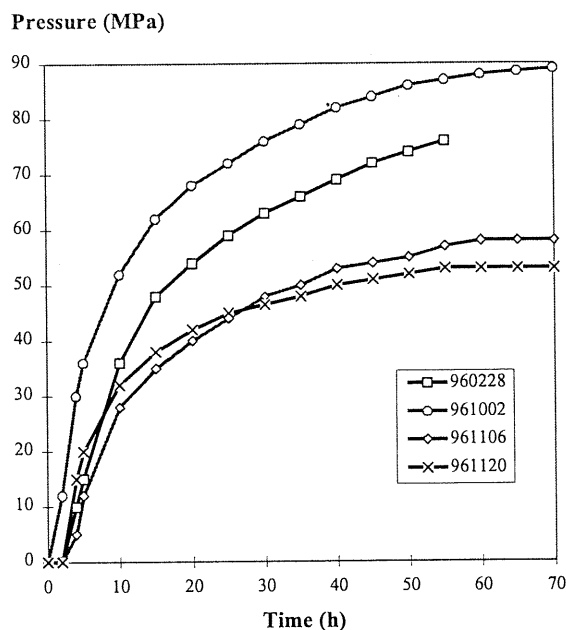
Figure 5.5-1. Variation in pressure developed by using Demex from different manufacturing lots.

5.6 Conclusions

The pressure obtained in tests using a 30 and 40 mm layer of mixed Demex was approximately 80 MPa and this is sufficient for the prospective in-situ test. Although it was not possible to measure the final pressure in the 40 mm layer case, extrapolation using the measured displacements of the upper piston of the cylinder-piston system indicates that the greatest pressure is not likely to significantly exceed 80 MPa (see Figure 5.6-1).

The reaction of CaO and water to produce $Ca(OH)_2$ also results in the release of heat and the reaction rate increases exponentially with temperature growth. The thermal peak comes early (in few hours) with respect to the pressure development, as seen in Figure 5.6-2. If the mass of expansive agent is too large, the production of heat becomes very rapid and results in boiling of water and blow out as happened in the test for the 53 mm thick layer of Demex mix, which boiled violently during the test, see Figure 5.6-3. The blow out stops the pressure generation and temperature rise. As the degree of overheating is proportional to the thickness of the layer of mixed Demex, this should be clearly be less than 53 mm.
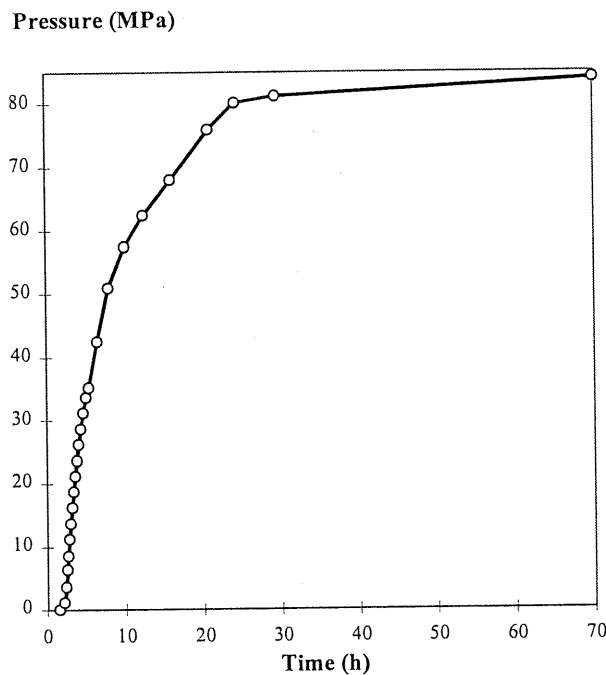
Pressure (MPa)

Figure 5.6-1. Extrapolated pressure development above 80 MPa for the test using a 40 mm layer of Demex mix.
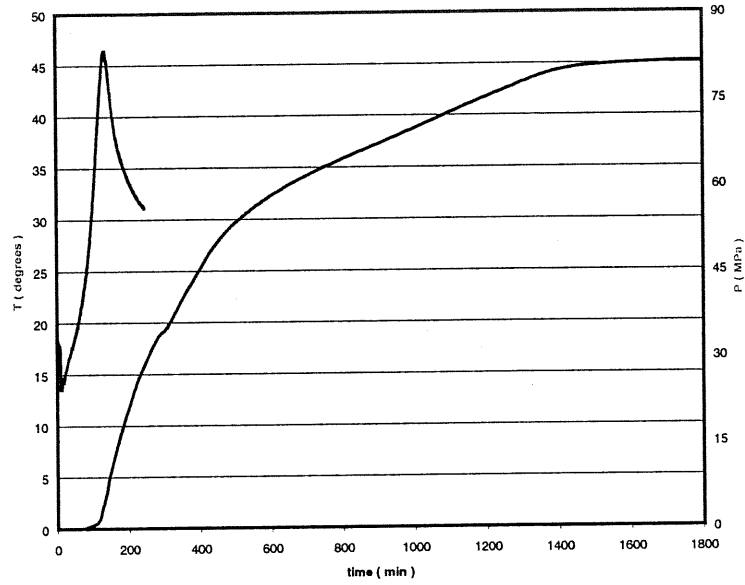
Figure 5.6-2. Pressure development (blue) and temperature(red) in the test using a 40 mm layer of Demex.
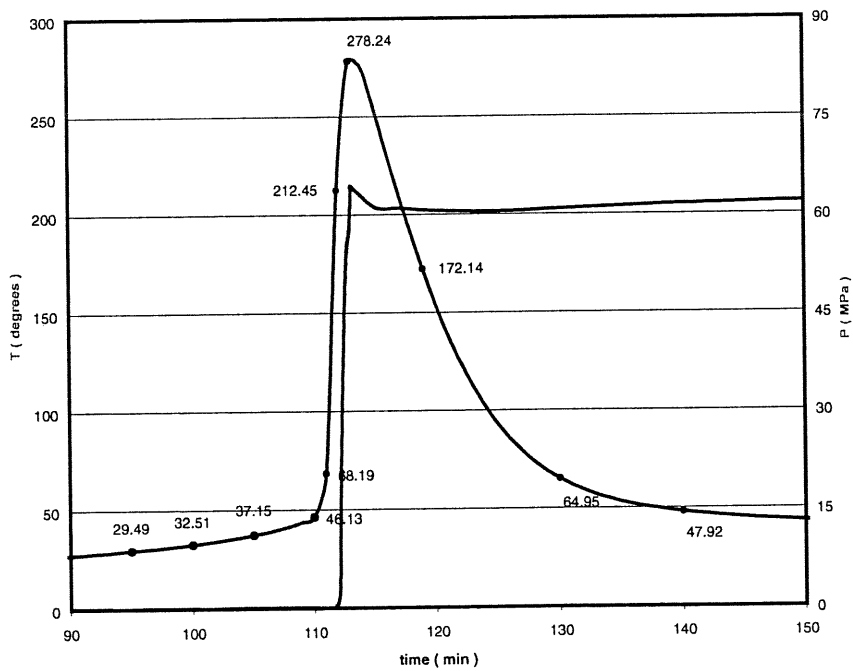
Figure 5.6-3. Pressure development (blue) and temperature (red) in the test using a 53 mm layer of Demex.

6 PRELIMINARY NUMERICAL MODELLING OF THE TEST USING FLAC^{3D}

6.1 General

Before carrying out the in-situ test, failure shall be modelled with the intention of comparing the results obtained against the actual modes of failure which occur during the test. The general objective of this work was to assess the applicability of numerical modelling codes and methods to the study of rock failure and associated crack propagation. The modelling was based on input data which was available at the time of modelling which differes somewhat from the data presented in Chapter 3 and 4.

The test programme includes three phases: design, execution and analysis. After completion of the design phase the feasibility of the test will be evaluated before proceeding to the experimental (i.e. execution) phase. The first step in the design phase, i.e. the modelling of the failure test in three dimensions (3D) by using Flac^{3D} code (Itasca 1995b), is reported in this chapter.

The first stage in the 3D modelling process was to create a 2D scooping model by using Flac^{2D} code (Itasca 1995a). The main purpose of this stage was to assess the actual feasibility of the test. Another objective was to make coarse adjustments to the test geometry if the results obtained indicated that such adjustments would be beneficial. An additional objective was to estimate the degree of deformation of the rock caused by the boring of the centre hole in the test design in order to obtain background information on the evaluation of different methods of measuring the in-situ stresses in rock. After 2D scooping calculations the basic geometry of the failure test was modelled in 3D by using Flac^{3D} code and the inout for modeling and results are presented in Chapters 6.2 – 6.5. After modeling the behaviour of the basic geometry, complementary modeling of a modified geometry was carried out and the rsults are presented in Chapter 6.6.

The modelling was based on the information about rock strength, in-situ stresses and other input data which was available at the time of modelling before the more specific and detailed infromation of the rock properties presented in this report was available. In the course of the design phase the input data presented in this report will be studied in greater detail and further modelling will be carried out if necessary using more specific and accurate data.

6.2 Rock properties and material models

Averages of all the measured values available at the time that the modelling was carried out were used as inputs for the modelling work: Young's modulus 58.3 GPa, Poisson's ratio 0.25, uniaxial compressive strength 81 MPa, tensile strength 8.4 MPa and density 2804 kg/m^3.

Three different types of isotropic homogeneous material models (see Fig. 6.2-1) were used: 1) elastic, 2) elastic /plastic behaving according to Mohr-Coulomb yield criteria (referred as Mohr-Coulomb hereafter) and 3) elastic/plastic behaving according to strain-softening Mohr-Coulomb yield criteria (referred as strain-softening hereafter).

The material parameters used in the strain-softening model (Table 6.2-1) were chosen heuristically on the basis of typical values previously determined for similar types of rock. As the objective was to conceptualise the strain-softening behaviour, the results achieved by modelling should be considered to be preliminary.

The parameters used in the strain-softening model, cohesion, friction and dilatation, are defined as functions of the total plastic strain. Once plastic yield begins, the program keeps track of the total plastic strain and determines the current values of cohesion, fiction and dilation which correspond to this strain (Itasca 1995a). The cohesion, friction and dilation are defined as a piecewise linear function of the total plastic strain. A detailed description of the model can be found in Itasca 1995a.

Table 6.2-1. Parameters used in the strain-softening model.

Plastic strain (%) ε^{ps}	Cohesion (MPa)	Friction (degrees)	Calculated Residual σc (MPa)
0.00	26.6	23.5	81
0.01	24.6	21.5	67
0.02	22.6	19.5	58
0.03	20.6	17.5	51
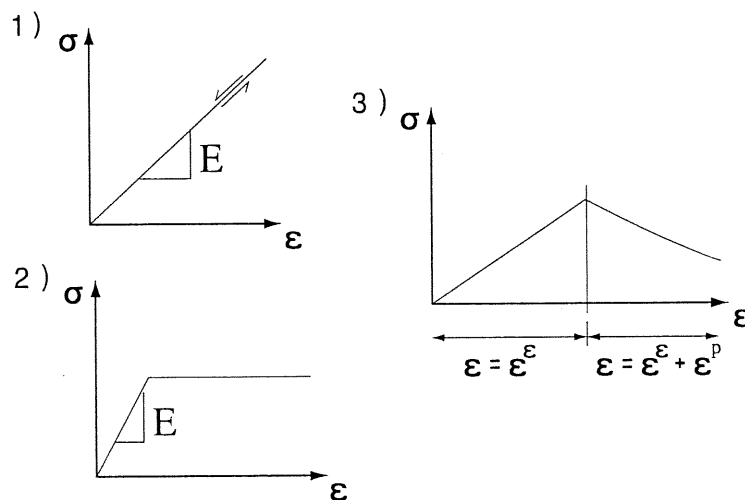
Figure 6.2-1. The three different constitutive material models: 1) Elastic, 2) Mohr-Coulomb and 3) Strain-softening.

The failure criteria used when calculating safety factors for the elastic analysis were the Mohr-Coulomb criterion and Mogi's polyaxial strength criterion (Haimson & Song 1995).

Values of cohesion and fiction angle for the Mohr-Coulomb criterion were estimated on the basis of results of uniaxial compression tests and Brazilian tensile tests. The criterion was estimated using three different types of subcriteria. These are shown as the lines marked 1, 2 and 3 in Figure 6.2-2. The Line 1 in Figure 6.2-2 was obtained by fitting it to the tensile strength and uniaxial compressive strength and follows the Mohr-Coulomb yield enevelope at lower stresses. The Line 3 describes material with limited tensile strength and which strength is determined by cohesion only. Line 2 describes material between Lines 1 and 3 which strength follows the Mohr-Coulomb envelope at higher compressive strengths.

Mogi's polyaxial criterion includes both minimum and intermediate stresses (Haimson & Song 1995).The parameters for the criterion (see Equation (6-1) and (6-2) below where f is an nearly-linear function) were estimated on the basis of uniaxial compression and the corresponding tensile strengths, see Figure 6.2-3.

$$\tau_{oct} = f_1\left(\sigma_2^m\right) \tag{6-1}$$

$$\tfrac{1}{3}\sqrt{(\sigma_1 - \sigma_2)^2 + (\sigma_2 - \sigma_3)^2 + (\sigma_3 - \sigma_1)^2} = f_1\left[\tfrac{1}{2}(\sigma_1 + \sigma_3)\right] \tag{6-2}$$
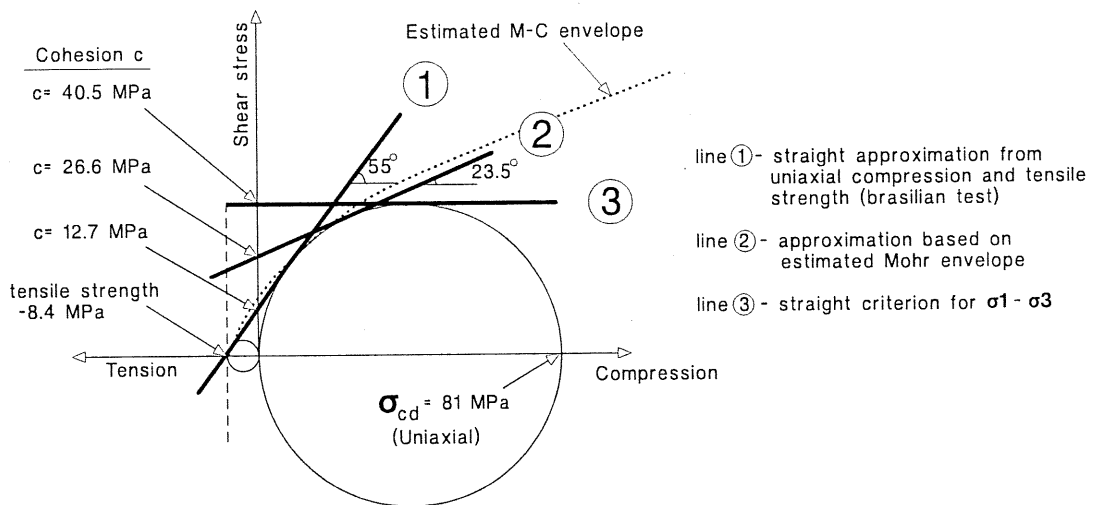
Figure 6.2-2. Mohr-Coulomb criterion types 1, 2 and 3 and their respective lines.
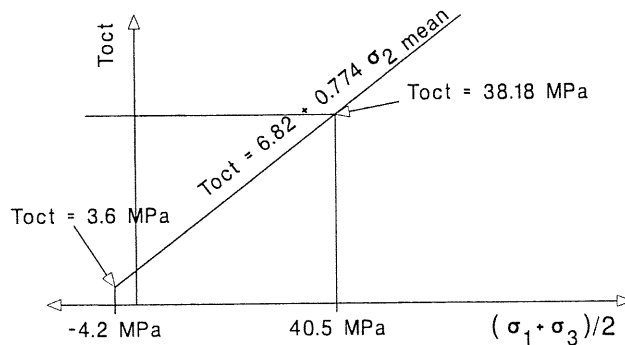
Figure 6.2-3. Mogi's criterion lines estimated from a uniaxial compression test.

6.3 Test geometry

The geometry used in the modelling consisted of a horizontally-oriented hole with identical slots positioned vertically above and below it, see Figure 6.3-1 and 6.3-2. The diameter and length of the central hole were set at 200 mm and 500 mm respectively. The distance from the axis of the borehole to the closest surface of each slot was set at 350 mm. Three different widths and depths of slot were modelled to establish the effect of slot dimensions on the resultant stress distribution. In the first model the width was set at 500 mm and the depth at 300 mm, in the second model the width was 1000 mm and the depth 500 mm, and in the third model the width was 1000 mm and the depth was 775 mm. In the last complementary model the diameter of the center hole was set at 100 mm and the slot width at 500 mm.
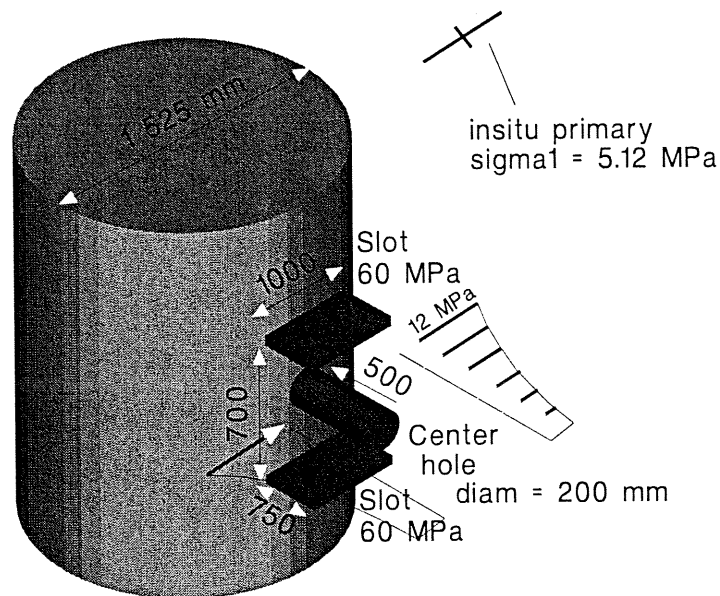
Figure 6.3-1. Geometry used in modelling.
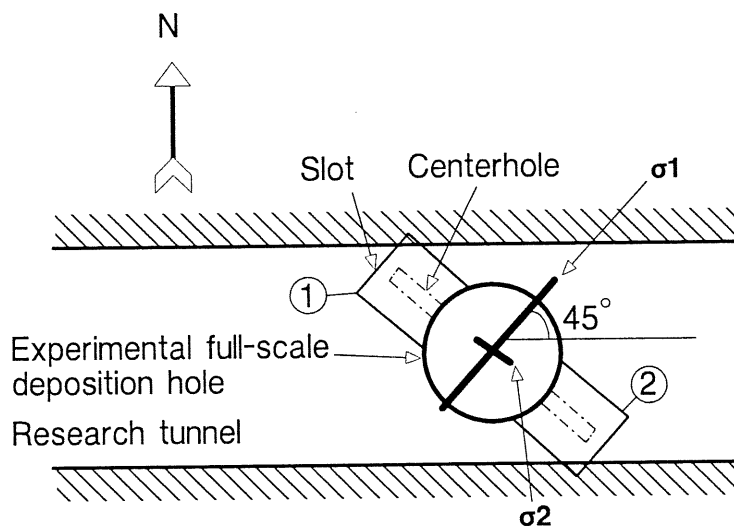
Figure 6.3-2. Horizontal section of the Research Tunnel showing the direction of primary in-situ stresses.

6.4   Rock stress, expansive pressure

The stress environment in the vicinity of the full-scale deposition holes differs from the in-situ stress because it is affected by both the full-scale hole and the existence of the Research Tunnel situated directly above it.

The stress conditions adjacent to the full-scale holes was first calculated using Kirsh's equation for the tangential stress around a circular 2D opening as presented in Chapter 4.4. This does not include the effect of Research Tunnel and assumes that the length of the full-scale hole is infinite. This calculation gave a maximum tangential stress adjacent to the surface of the opening of 12 MPa at a depth of 4 cm. At a depth of 32 cm the stress was approximately 8 MPa and at a depth of 90 cm the stress was approximately 6 MPa.

The stress conditions around the full-scale holes were then modelled by using numerical 3DEC code (Itasca 1994). For practical purposes, the geometry of the Research Tunnel was simplified to more closely resemble the proposed deposition tunnels. According to the cross-sectional contour plots, the stress conditions around the full-scale hole are close to two dimensional at a depth of 3.5 to 4.5 m from the tunnel floor. At this range of depths neither the Research Tunnel nor the bottom of the full-scale hole appear to have any significant effect on the stresses adjacent to the surface of the full-scale hole. From both the modelling and the experimental points of view it is beneficial to have both uniform and symmetrical stress conditions in the test area.

The maximum tangential stress of 12 MPa given by modelling an analytical calculation at a depth ranging from 3.5 to 4.5 m was therefore chosen as the input boundary (constraining) stress for the modelling process. It was assumed that stress follows Kirsch's equation and decreases to the in-situ level at a depth of 2 m from the surface of the full-scale hole.

Different pressures caused by the introduction of an expanding agent into the slots were modelled to establish the minimum pressure level which would cause failure. The input pressures used were from either 20 or 30 MPa up to 60 MPa in 10 MPa steps.

6.5   Results of modelling

Test geometry

Comparison of the predicted stress fields around the test hole resulting from the use of different slot sizes showed that the largest slot size (width 1000 mm / length 775 mm) resulted in significantly higher stresses and a more uniform stress field. Further enlargement of the slots would be impractical from an experimental point of view and a slot size of width 1000 mm and length 775 mm was assessed as being the most suitable for the test. The maximum tangential compressive stress developed around the borehole was 198 MPa at a slot pressure of 60 MPa and this was taken as the highest stress which could be achieved with an adequate degree of certainty. It was noted that even at a swelling pressure of 40 MPa, the maximum principal stresses at the surface of the hole exceed the uniaxial compressive strength of the rock. It is therefore evident that a

swelling pressure high enough to cause failure can be achieved in the experiment and that the stress distribution on the stem section of the hole is reasonably uniform.

Models

Modelling using the elastic material model with Mohr-Coulomb failure criteria of type (2) and (3); the Mohr-Coulomb plastic material model with failure criteria of type (2) and (3); Mogi's failure criteria; and the strain-softening material model gave very similar results at swelling pressures between 30 and 40 MPa. Although slight differences could be seen in the extent of the areas of failure, the main features observed were very similar.

As they had not been determined experimentally, the parameters used in the strain-softening model were of a tentative nature and this result is therefore considered to be the most unreliable. If the parameters could be used with greater confidence, the strain-softening model would be a suitable method for the modelling of progressive failure because the strength of the modelled material is reduced as failure takes place.

The parameters employed with Mogi's criterion were estimated from the results of uniaxial compression and Brazilian tests and the predicted safety factors should therefore only be comparable with modelling which employs the Mohr-Coulomb type (1) criterion. The magnitudes of the stress components $\sigma 2$ and $\sigma 3$ were of the same order and therefore the difference between results obtained using the Mohr-Coulomb criterion of type (1) and Mogi's criterion should be small.

Failure prediction

Modelling results obtained using the elastic material model and Mohr-Coulomb failure criteria of types (2) and (3); the Mohr-Coulomb material model and failure criteria of type (2) and (3); and Mogi's failure criterion; and the strain-softening material model all predict similar areas for initial failure. Regardless of the material model and criteria employed, failure appears at a swelling pressure of well below 60 MPa, and in some cases at a swelling pressure as low as 30 MPa. The forms in which failure is predicted to take place are tensile failure on the upper and lower surfaces of the test hole and compressive/shear failure on the side surfaces. The results of modelling using swelling pressures of 30 and 40 MPa with the Mohr-Coulomb material model with cohesion 26.6 MPa and fiction angle of 23.5°, and the same model with cohesion of 40.5 MPa and fiction angle 0° are shown in Figures 6.5-1 and 6.5-2, and are considered to be a satisfactory representation of the areas of failure surrounding the test hole. Figure 6.5-3 is a vertical section taken perpendicular to the axis of the test hole which shows the modelled areas of failure.

The results of modelling using a swelling pressure of 50 MPa with the Mohr-Coulomb material model with cohesion 26.6 MPa and friction angle of 23.50, which are considered to be a satisfactory representation of the deformation properties surrounding the test hole, are shown in Figure 6.5-4 as a vertical section taken parallel to the axis of the test hole. A horizontal section of the for the same conditions is shown in Figure 6.5-5. Sections perpendicular to the test hole at the positions shown in Figure 6.5-4 are shown in Figures 6.5-6 and 6.5-7.
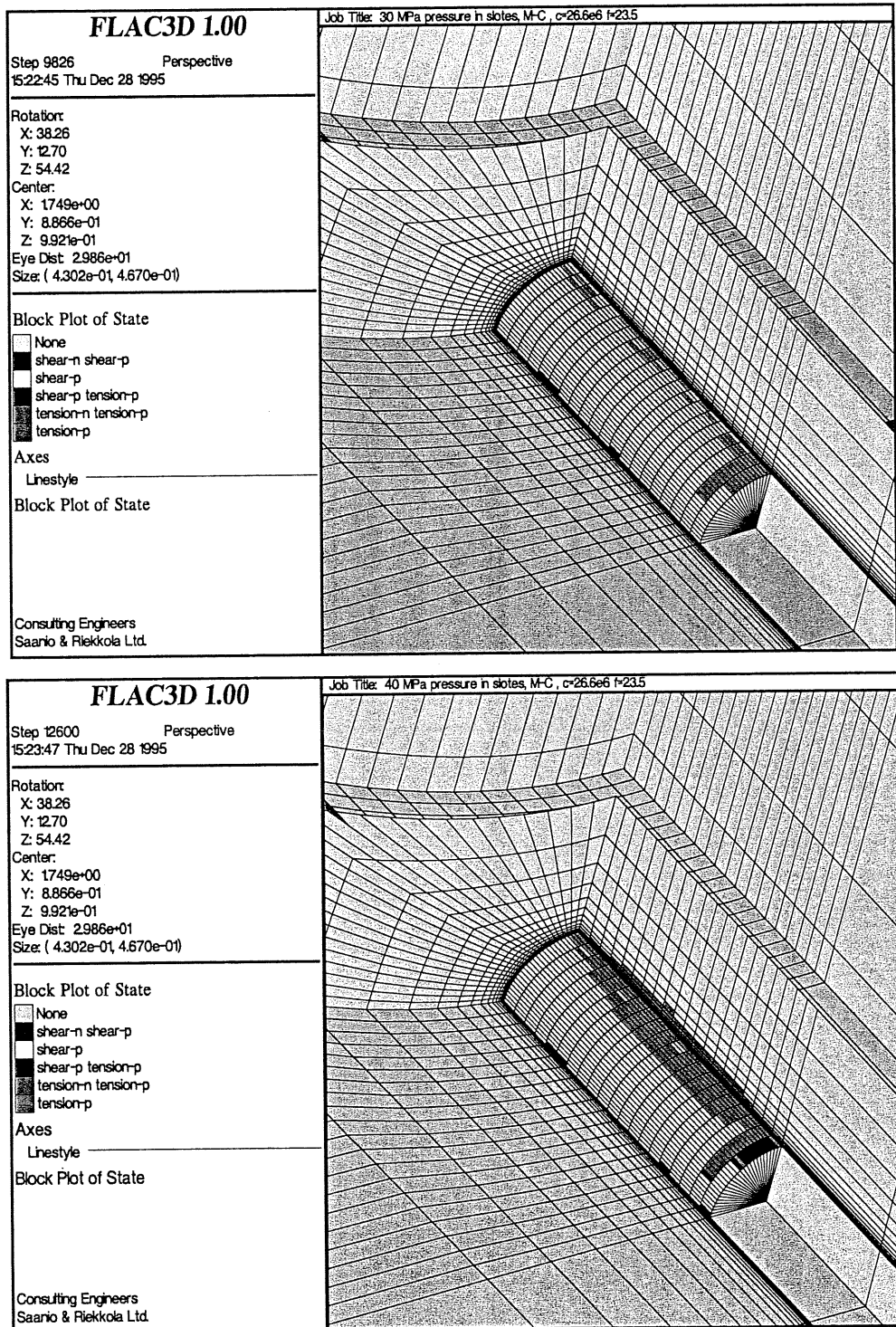
Figure 6.5-1. *Results obtained by modelling swelling pressures of 30 MPa (top) and 40 MPa (bottom) using the Mohr-Coulomb material model with criterion of type (1), cohesion 26.6 MPa, fiction angle 23.5°.*
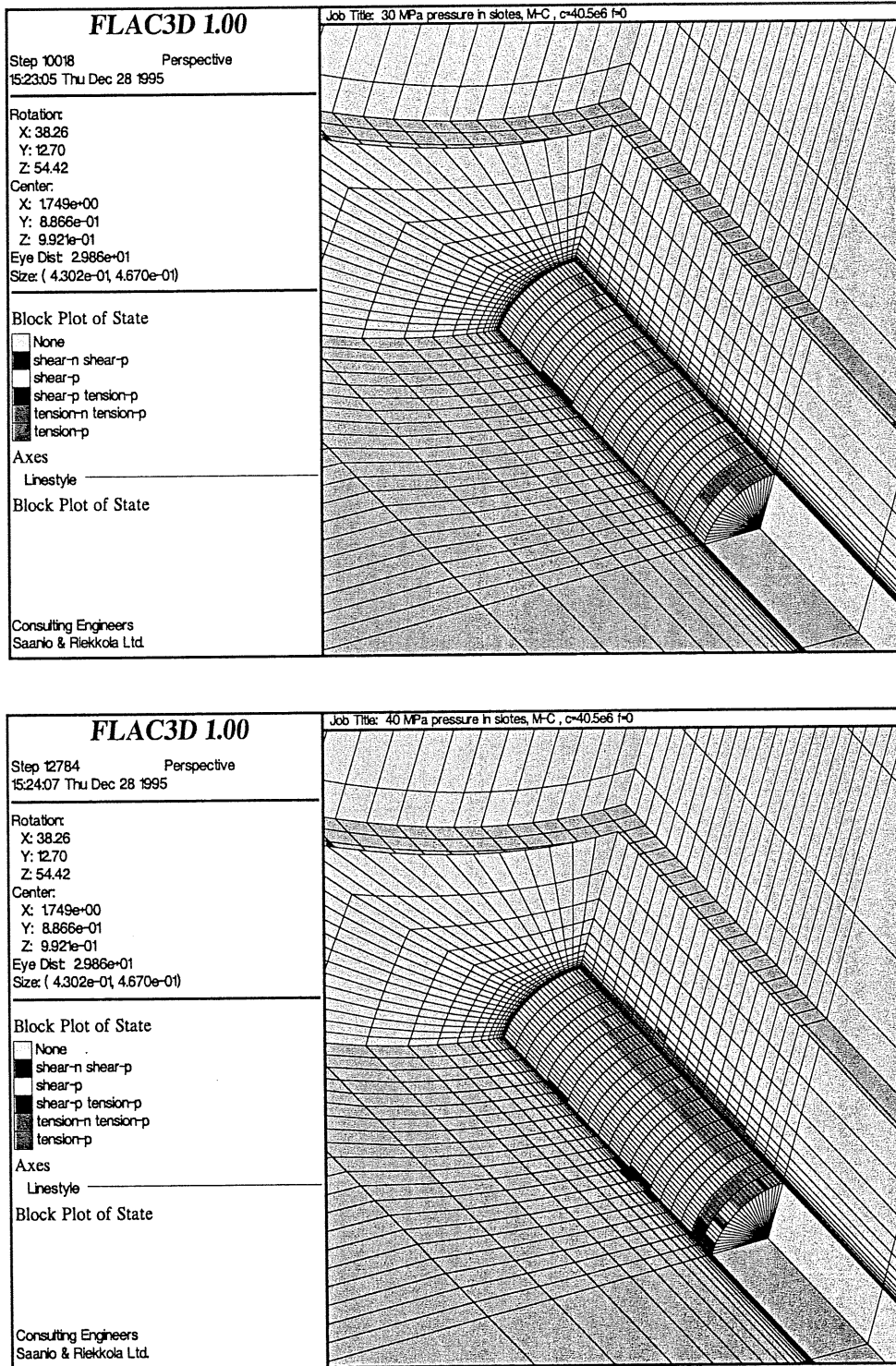
Figure 6.5-2. Results obtained by modelling swelling pressures of 30 MPa (top) and 40 MPa (bottom) using the Mohr-Coulomb material model with criterion of type (1), cohesion 40.5 MPa, friction angle 0°.
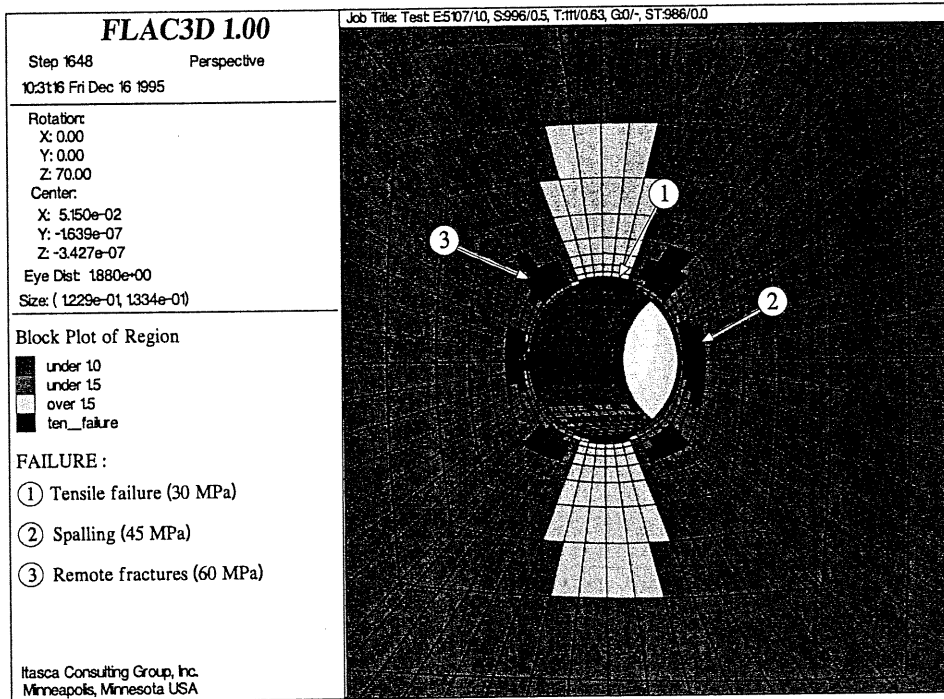
Figure 6.5-3. *Vertical section perpendicular to the axis of test hole showing the modelled failure areas.*
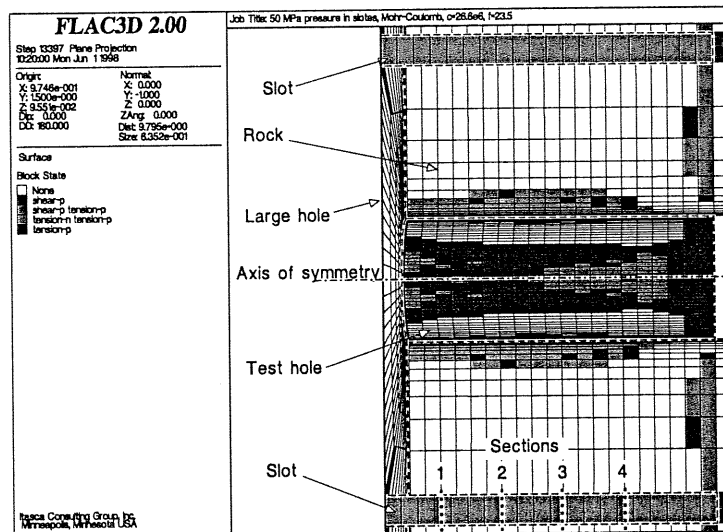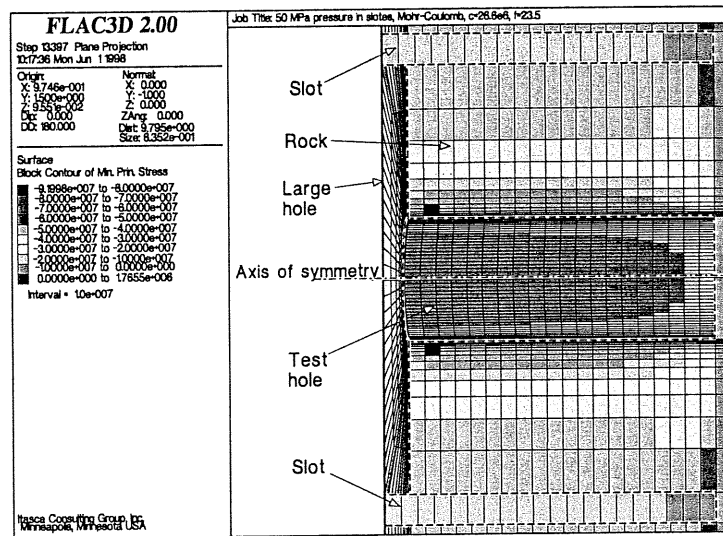
Figure 6.5-4. A vertical section taken parallel to the axis of the test hole showing the state of stress (top) and state of failure (bottom) with a swelling pressure of 50 MPa and the Mohr-Coulomb material model with cohesion 26.6 MPa and friction angle of 23.5°.
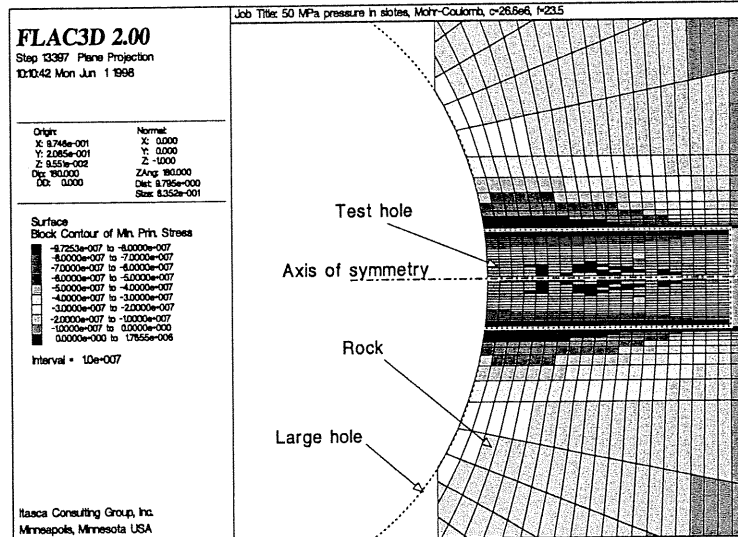
Figure 6.5-5. *A horizontal section taken parallel to the axis of the test hole, showing the state of stress (top) and state of failure (bottom) with a swelling pressure of 50 MPa and the Mohr-Coulomb material model with cohesion 26.6 MPa and friction angle of 23.5°.*
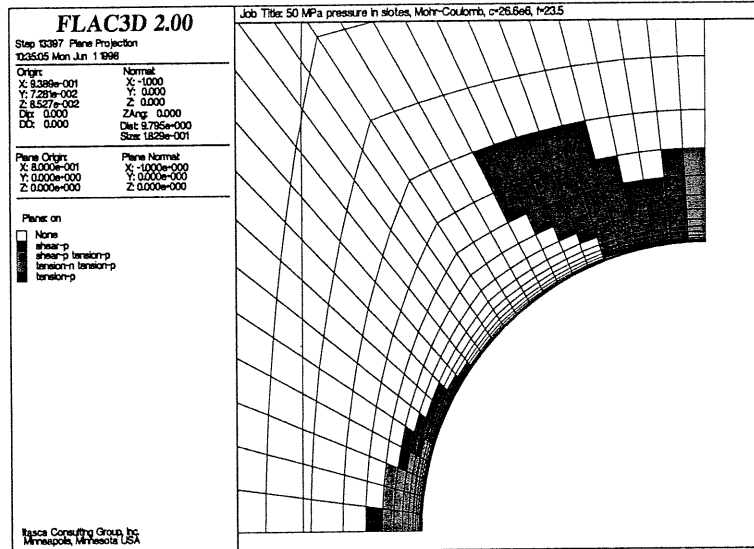
Section 1
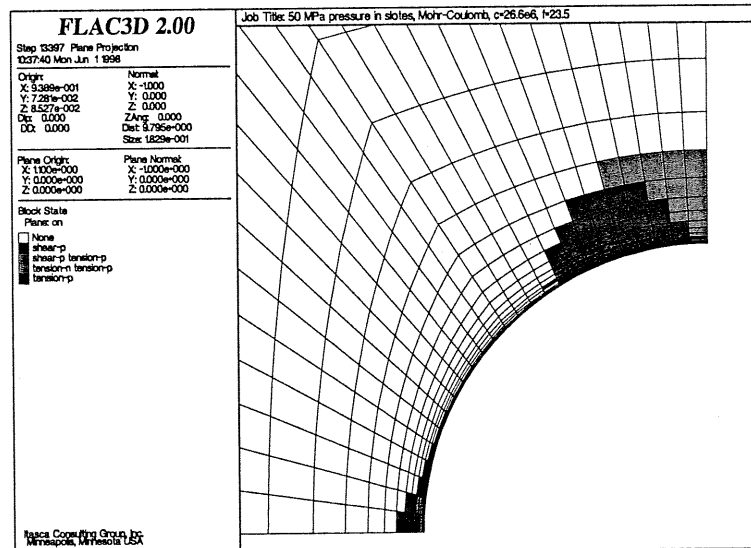
Section 2

Figure 6.5-6. Sections 1 and 2 perpendicular to the test hole at the positions shown in Figure 6-4 showing the state of failure with a swelling pressure of 50 MPa and the Mohr-Coulomb material model with cohesion 26.6 MPa and a friction angle of 23.5°.
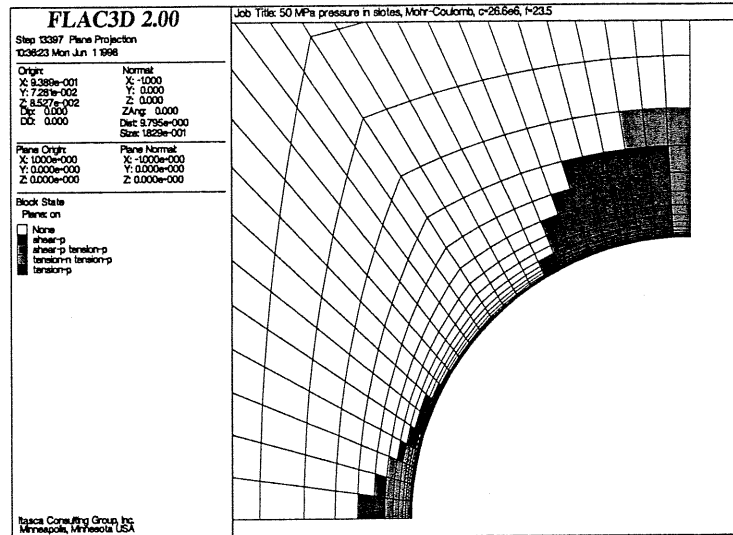
Section 3
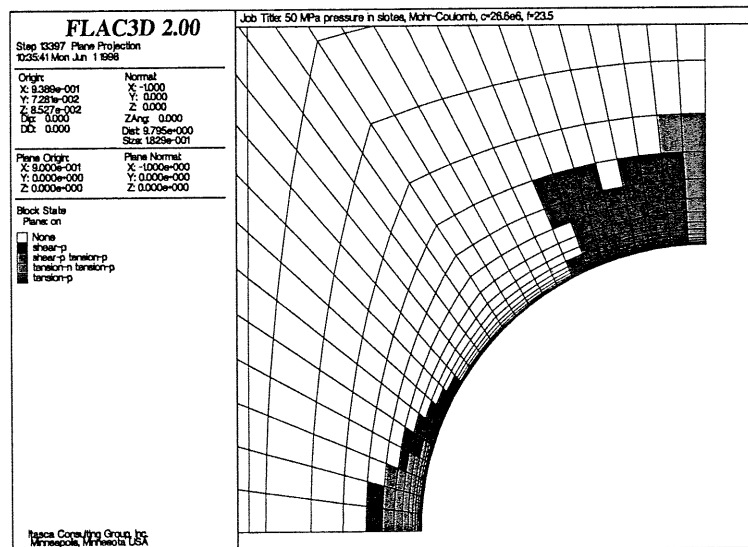
Section 4

Figure 6.5-7. Sections 3 and 4 taken perpendicular to the test hole at the positions indicated in Figure 6-4 showing the state of failure with a swelling pressure of 50 MPa and the Mohr-Coulomb material model with cohesion 26.6 MPa and a friction angle of 23.5°.

6.6   Complementary modeling

Modelling using a swelling pressure of 50 MPa and the Mohr-Coulomb material model with cohesion 26.6 MPa and a friction angle of 23.5°, which are considered to be a satisfactory representation of the rock properties surrounding the test hole, was repeated using a geometry with curved slots of width and depth of 500 mm and smaller 100 mm diameter centre hole.

From the experimental point of view it is beneficial to have slightly curved slots because this simplifies the process of filling of the slots with expanding agent. Another advantage is that it increases slightly the state of stress and the horizontal component around the test hole.

Use of a slot design with 50 mm front filling is beneficial from experimental point of view since it reduces the possibility for shear failure at surface of the large and also improves the geometry of the stress field around the test hole to be closer to two dimensional. Therefore and alternative design with front filling was also modelled.

The element mesh at the bottom end of the centre hole was modified by reducing the element size and increasing the number of elements in order to obtain a more accurate indication of the stress distribution.

The modelling results with 50 mm fronfilling of the slot are shown in Figures 6.6-1 – 6.6-9 which show vertical and horizontal sections taken parallel and perpendicular to the axis of the test hole. The results of corresponding modelling without frontfilling are shown in Figures 6.6-10 – 6.6-15.

The modified geometry with curved slots of width and depth of 500 mm, 50 mm of front filling and 100 mm diameter centre hole produces a state of stress in the center part of the test hole is close to desired two dimensional state of stress and high enough for failures to occur in a detectable scale.

The results show that the modifications of the test geometry improves the shape of stress field around the test hole and technical implementation of the test without compromising the objectives.
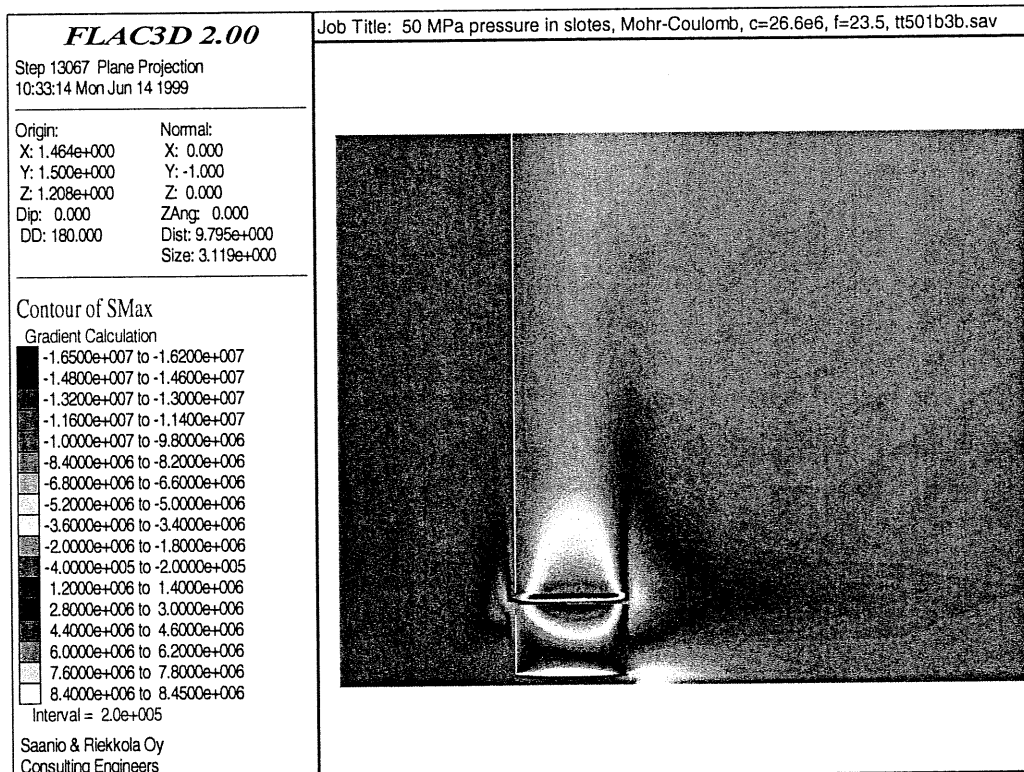
Figure 6.6-1. *A vertical section taken perpendicular to the axis of the test hole showing the state of major σ_1 (top) and minor σ_3 stresses (bottom) with a swelling pressure of 50 MPa. Slot width and depth 500 mm, diameter of center hole 100 mm, frontfilling 50 mm.*

FLAC3D 2.00

Step 13067 Plane Projection
10:15:38 Mon Jun 14 1999

Origin: Normal:
X: 1.043e+000   X: 0.000
Y: 1.000e-003   Y: -1.000
Z: 2.684e-001   Z: 0.000
Dip: 0.000   ZAng: 0.000
DD: 180.000   Dist: 9.795e+000
                   Size: 6.290e-001

Plane Origin: Plane Normal:
X: 0.000e+000   X: 0.000e+000
Y: 1.000e-003   Y: -1.000e+000
Z: 0.000e+000   Z: 0.000e+000

Contour of SMin
  Gradient Calculation
  -9.0000e+007 to -8.9000e+007
  -8.4000e+007 to -8.3000e+007
  -7.8000e+007 to -7.7000e+007
  -7.2000e+007 to -7.1000e+007
  -6.6000e+007 to -6.5000e+007
  -6.0000e+007 to -5.9000e+007
  -5.4000e+007 to -5.3000e+007
  -4.8000e+007 to -4.7000e+007
  -4.2000e+007 to -4.1000e+007
  -3.6000e+007 to -3.5000e+007
  -3.0000e+007 to -2.9000e+007
  -2.4000e+007 to -2.3000e+007
  -1.8000e+007 to -1.7000e+007

Saanio & Riekkola Oy
Consulting Engineers

Job Title: 50 MPa pressure in slotes, Mohr-Coulomb, c=26.6e6, f=23.5, tt501b3b.sav

FLAC3D 2.00

Step 13067 Plane Projection
10:16:36 Mon Jun 14 1999

Origin: Normal:
X: 1.043e+000   X: 0.000
Y: 1.268e-001   Y: 0.000
Z: 2.684e-001   Z: -1.000
Dip: 180.000   ZAng: 180.000
DD: 0.000   Dist: 9.795e+000
                   Size: 6.290e-001

Plane Origin: Plane Normal:
X: 0.000e+000   X: 0.000e+000
Y: 0.000e+000   Y: 0.000e+000
Z: 1.000e-003   Z: -1.000e+000

Contour of SMin
  Gradient Calculation
  -9.0000e+007 to -8.9000e+007
  -8.4000e+007 to -8.3000e+007
  -7.8000e+007 to -7.7000e+007
  -7.2000e+007 to -7.1000e+007
  -6.6000e+007 to -6.5000e+007
  -6.0000e+007 to -5.9000e+007
  -5.4000e+007 to -5.3000e+007.
  -4.8000e+007 to -4.7000e+007
  -4.2000e+007 to -4.1000e+007
  -3.6000e+007 to -3.5000e+007
  -3.0000e+007 to -2.9000e+007
  -2.4000e+007 to -2.3000e+007
  -1.8000e+007 to -1.7000e+007

Saanio & Riekkola Oy
Consulting Engineers

Job Title: 50 MPa pressure in slotes, Mohr-Coulomb, c=26.6e6, f=23.5, tt501b3b.sav

Figure 6.6-2. A vertical (top) and horizontal (bottom) section taken parallel to the axis of the test hole showing the state of major σ_1 stresses with a swelling pressure of 50 MPa. Slot width and depth 500 mm, diameter of center hole 100 mm, frontfilling 50 mm.
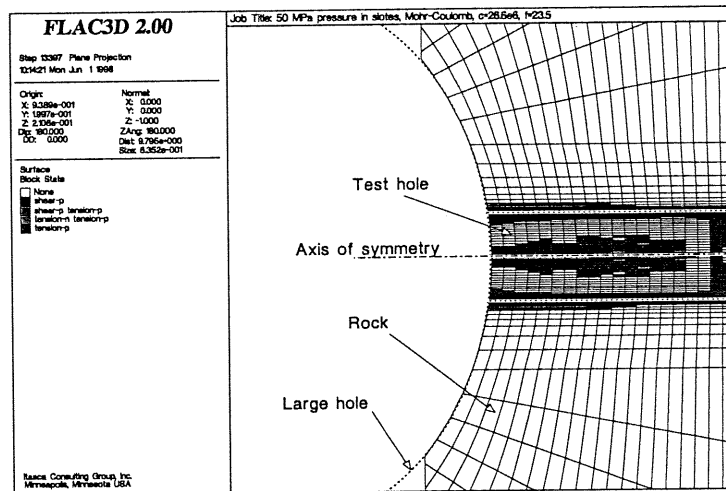
Figure 6.6-3. *A vertical section taken parallel to the axis of the test hole showing the state of major σ_1 stresses with a swelling pressure of 50 MPa. Slot width and depth 500 mm, diameter of center hole 100 mm, frontfilling 50 mm. Top Figure 6.6-2 shows the upper half of this figure.*

Figure 6.6-4. *Vertical sections taken perpendicular to the axis of the test hole showing the state of major σ_1 stresses at depth of 50 mm (top) and 150 mm (bottom) with a swelling pressure of 50 MPa. Slot width and depth 500 mm, diameter of center hole 100 mm, frontfilling 50 mm.*

Figure 6.6-5. Vertical section taken perpendicular to the axis of the test hole showing the state of major σ_1 stresses at depth of 150 mm with a swelling pressure of 50 MPa. Slot width and depth 500 mm, diameter of center hole 100 mm, frontfilling 50 mm. Upper half of the figure is shown in Figure 6.6-4.

Figure 6.6-6. *Vertical sections taken perpendicular to the axis of the test hole showing the state of major σ_1 stresses at depth of 250 mm (top) and 350 mm (bottom) with a swelling pressure of 50 MPa. Slot width and depth 500 mm, diameter of center hole 100 mm, frontfilling 50 mm.*
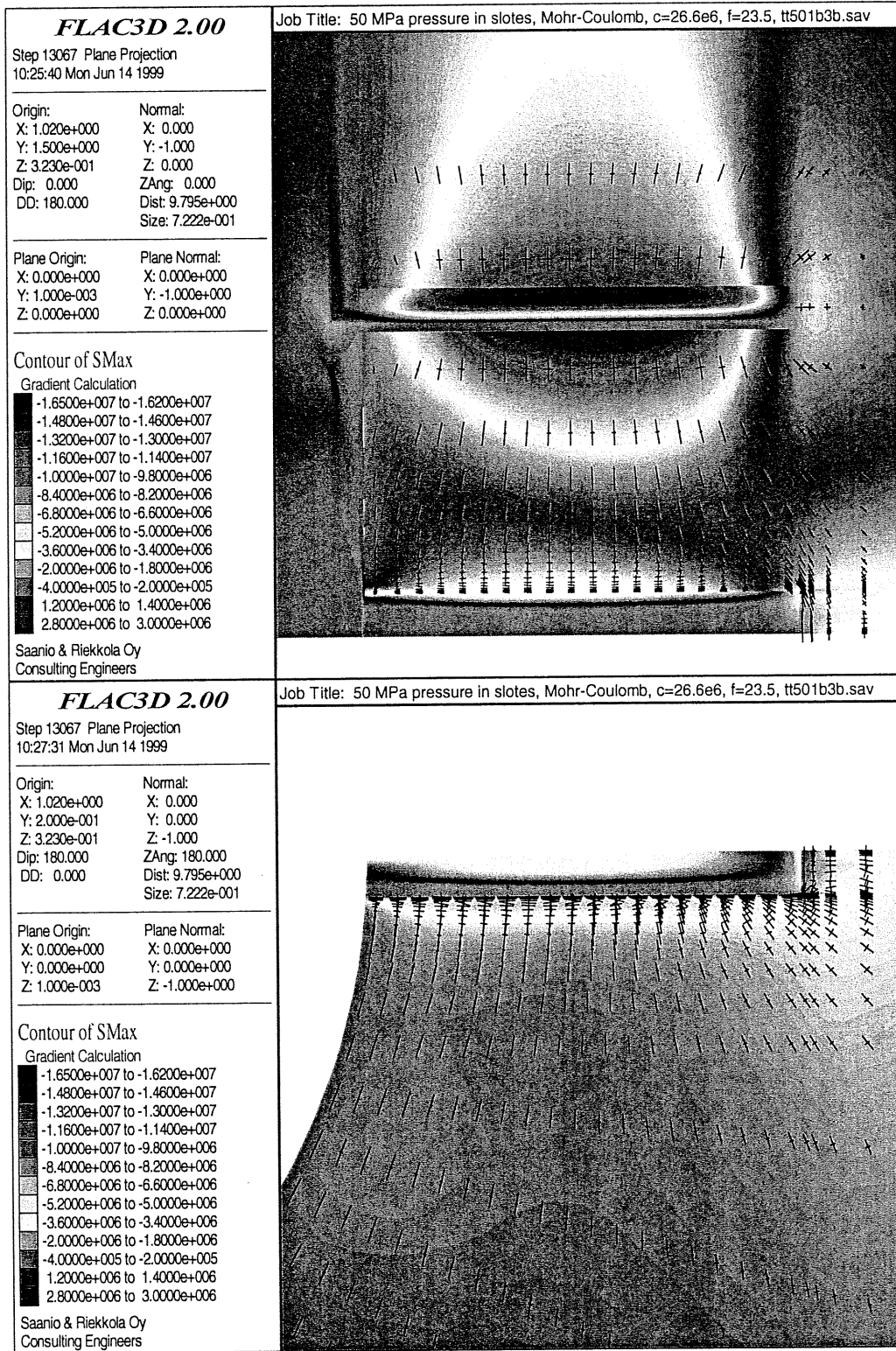
Figure 6.6-7. A vertical (top) and horizontal (bottom) section taken parallel to the axis of the test hole showing the state of minor σ_3 stresses with a swelling pressure of 50 MPa. Slot width and depth 500 mm, diameter of center hole 100 mm, frontfilling 50 mm.

FLAC3D 2.00

Step 13067 Plane Projection
10:23:39 Mon Jun 14 1999

Origin:	Normal:
X: 8.000e-001	X: -1.000
Y: 1.467e-001	Y: 0.000
Z: 2.467e-001	Z: 0.000
Dip: 0.000	ZAng: 0.000
DD: 0.000	Dist: 9.795e+000
	Size: 5.394e-001

Plane Origin:	Plane Normal:
X: 8.000e-001	X: -1.000e+000
Y: 0.000e+000	Y: 0.000e+000
Z: 0.000e+000	Z: 0.000e+000

Contour of SMax
  Plane: on
  Gradient Calculation
  -1.6500e+007 to -1.6200e+007
  -1.4800e+007 to -1.4600e+007
  -1.3200e+007 to -1.3000e+007
  -1.1600e+007 to -1.1400e+007
  -1.0000e+007 to -9.8000e+006
  -8.4000e+006 to -8.2000e+006
  -6.8000e+006 to -6.6000e+006
  -5.2000e+006 to -5.0000e+006
  -3.6000e+006 to -3.4000e+006
  -2.0000e+006 to -1.8000e+006
  -4.0000e+005 to -2.0000e+005
   1.2000e+006 to 1.4000e+006

Saanio & Riekkola Oy
Consulting Engineers

Job Title: 50 MPa pressure in slotes, Mohr-Coulomb, c=26.6e6, f=23.5, tt501b3b.sav

FLAC3D 2.00

Step 13067 Plane Projection
10:23:07 Mon Jun 14 1999

Origin:	Normal:
X: 9.000e-001	X: -1.000
Y: 1.467e-001	Y: 0.000
Z: 2.467e-001	Z: 0.000
Dip: 0.000	ZAng: 0.000
DD: 0.000	Dist: 9.795e+000
	Size: 5.394e-001

Plane Origin:	Plane Normal:
X: 9.000e-001	X: -1.000e+000
Y: 0.000e+000	Y: 0.000e+000
Z: 0.000e+000	Z: 0.000e+000

Contour of SMax
  Plane: on
  Gradient Calculation
  -1.6500e+007 to -1.6200e+007
  -1.4800e+007 to -1.4600e+007
  -1.3200e+007 to -1.3000e+007
  -1.1600e+007 to -1.1400e+007
  -1.0000e+007 to -9.8000e+006
  -8.4000e+006 to -8.2000e+006
  -6.8000e+006 to -6.6000e+006
  -5.2000e+006 to -5.0000e+006
  -3.6000e+006 to -3.4000e+006
  -2.0000e+006 to -1.8000e+006
  -4.0000e+005 to -2.0000e+005
   1.2000e+006 to 1.4000e+006

Saanio & Riekkola Oy
Consulting Engineers

Job Title: 50 MPa pressure in slotes, Mohr-Coulomb, c=26.6e6, f=23.5, tt501b3b.sav

Figure 6.6-8. Vertical sections taken perpendicular to the axis of the test hole showing the state of minor σ_3 stresses at depth of 50 mm (top) and 150 mm (bottom) with a swelling pressure of 50 MPa. Slot width and depth 500 mm, diameter of center hole 100 mm, frontfilling 50 mm.
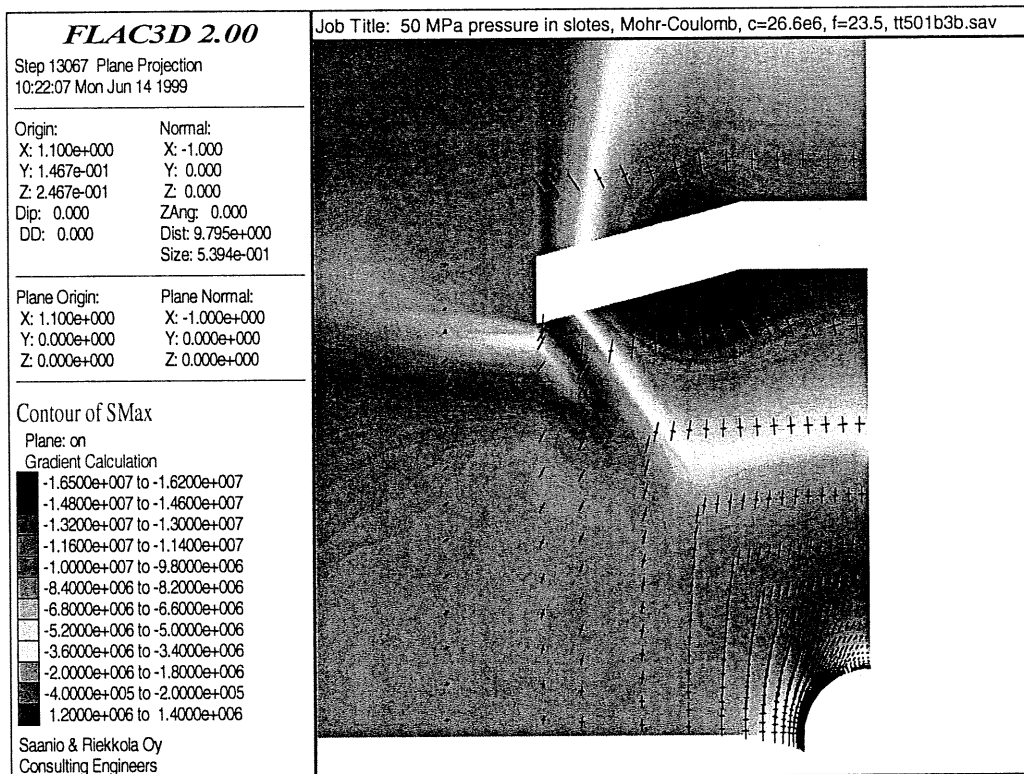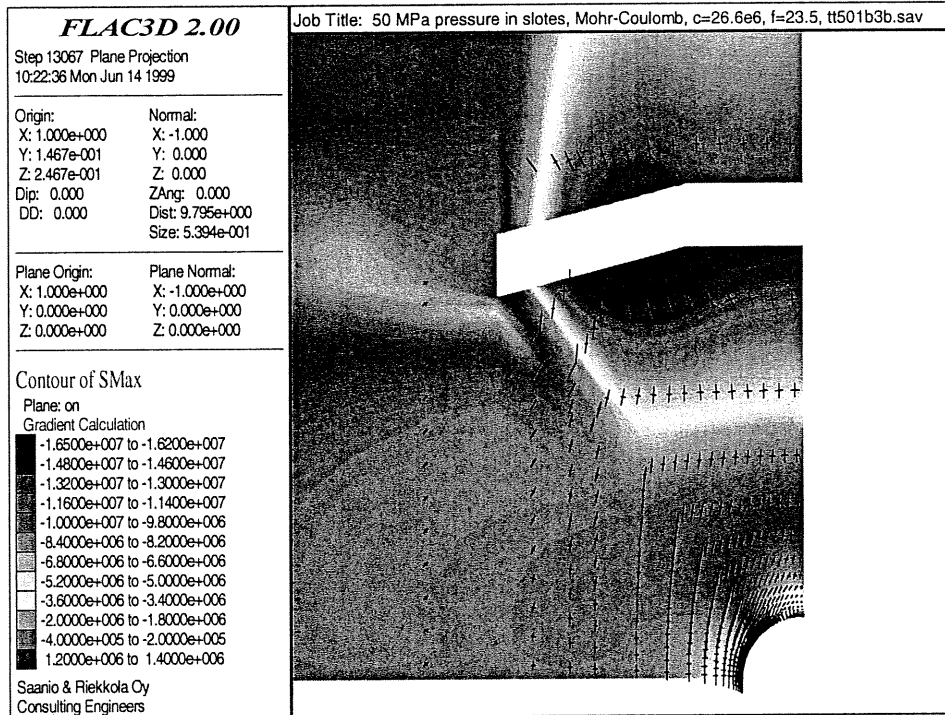
Figure 6.6-9. Vertical sections taken perpendicular to the axis of the test hole showing the state of minor σ_3 stresses at depth of 250 mm (top) and 350 mm (bottom) with a swelling pressure of 50 MPa. Slot width and depth 500 mm, diameter of center hole 100 mm, frontfilling 50 mm.
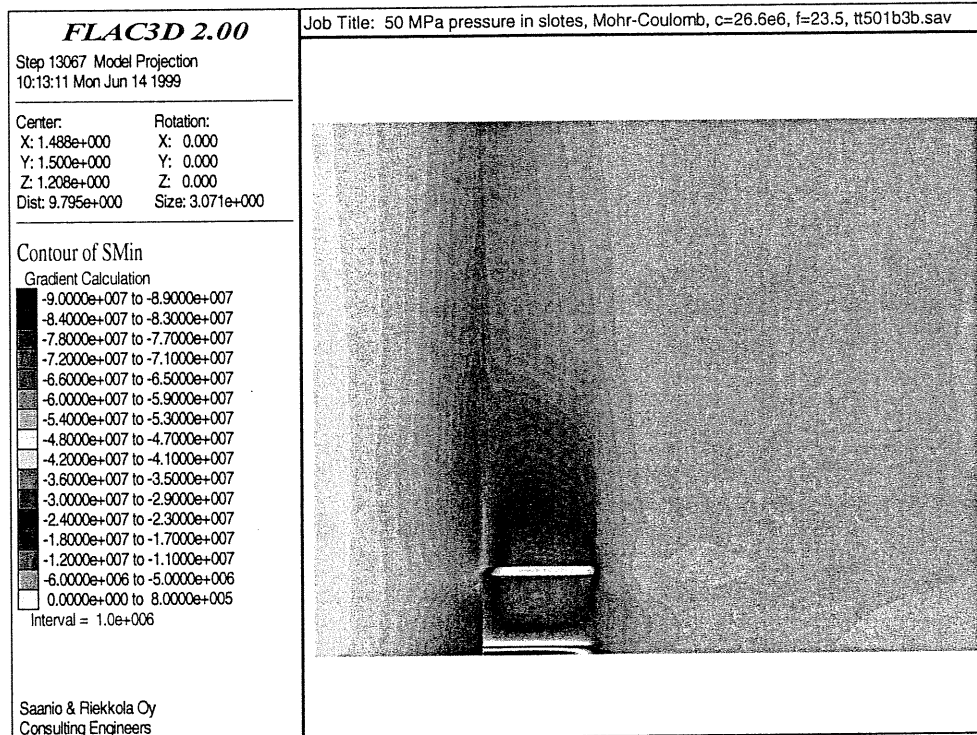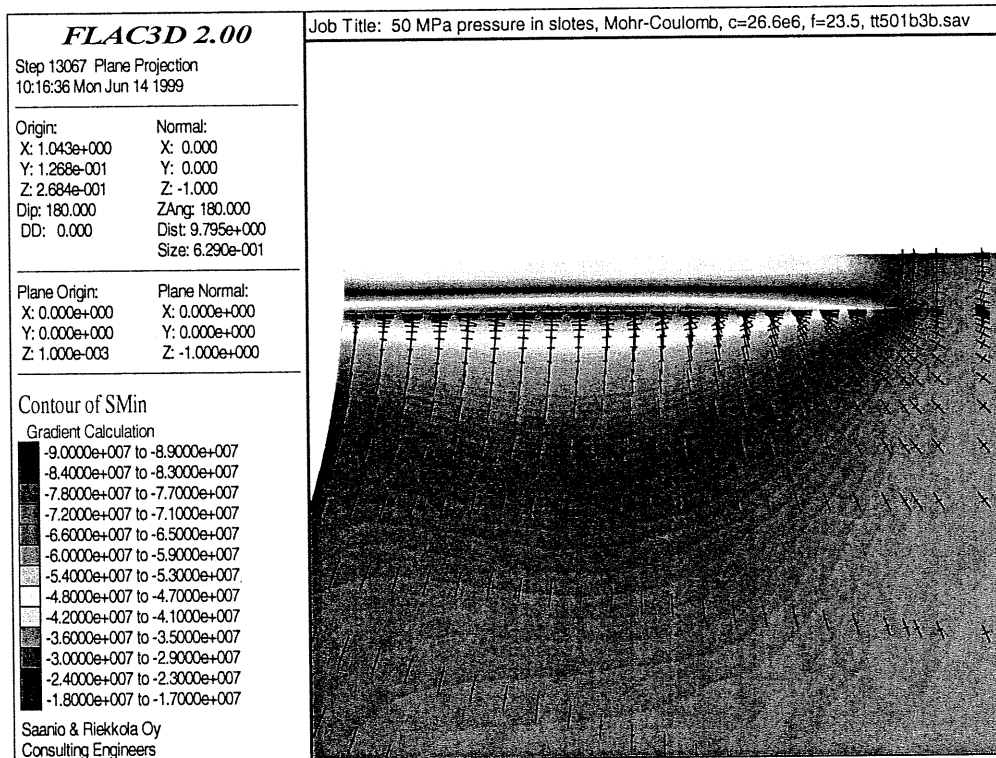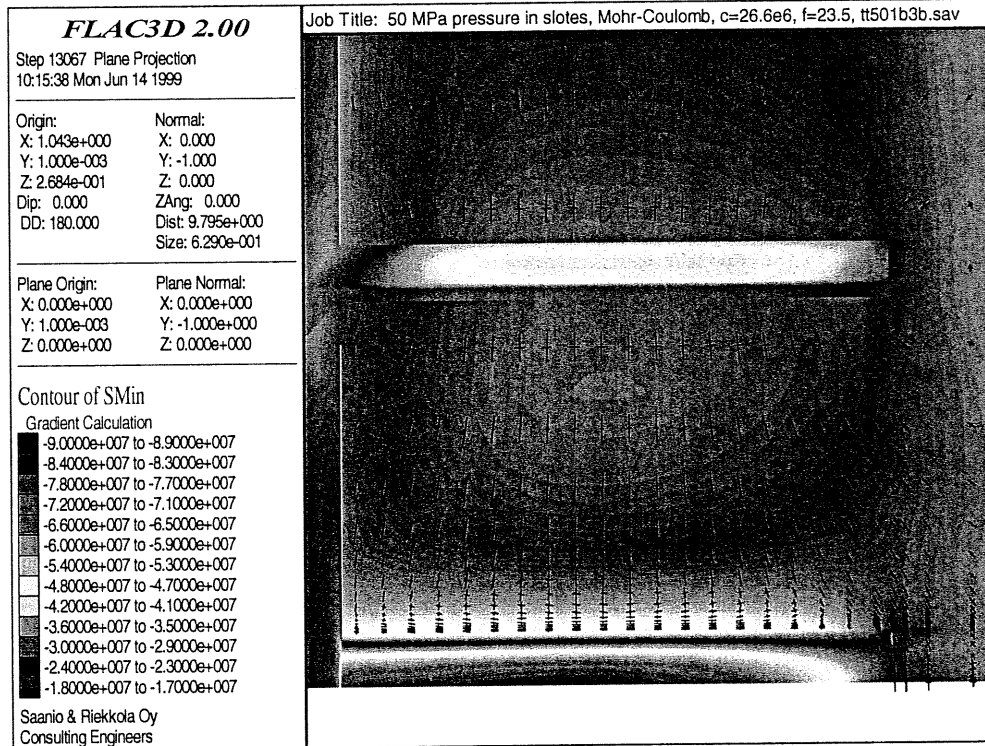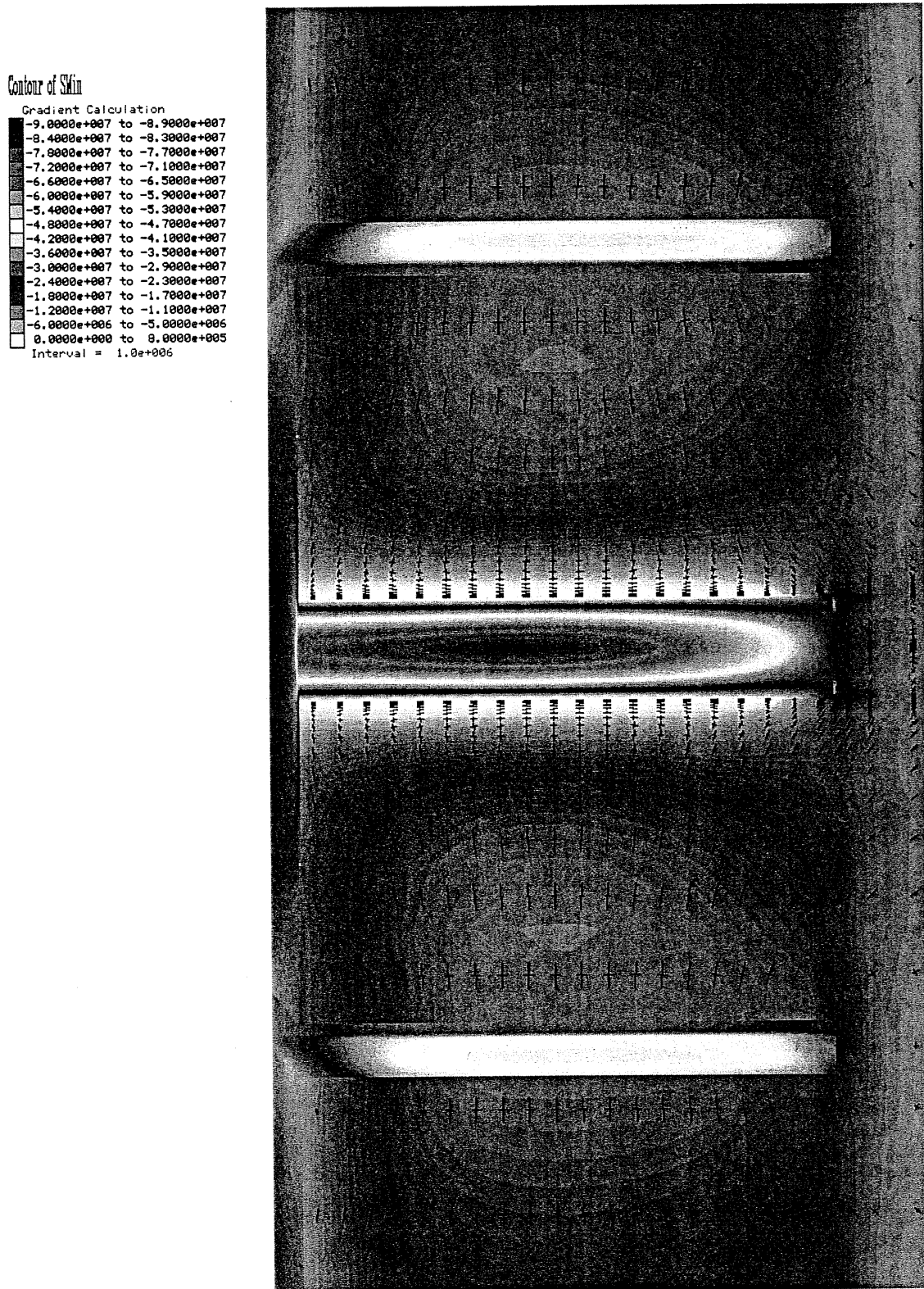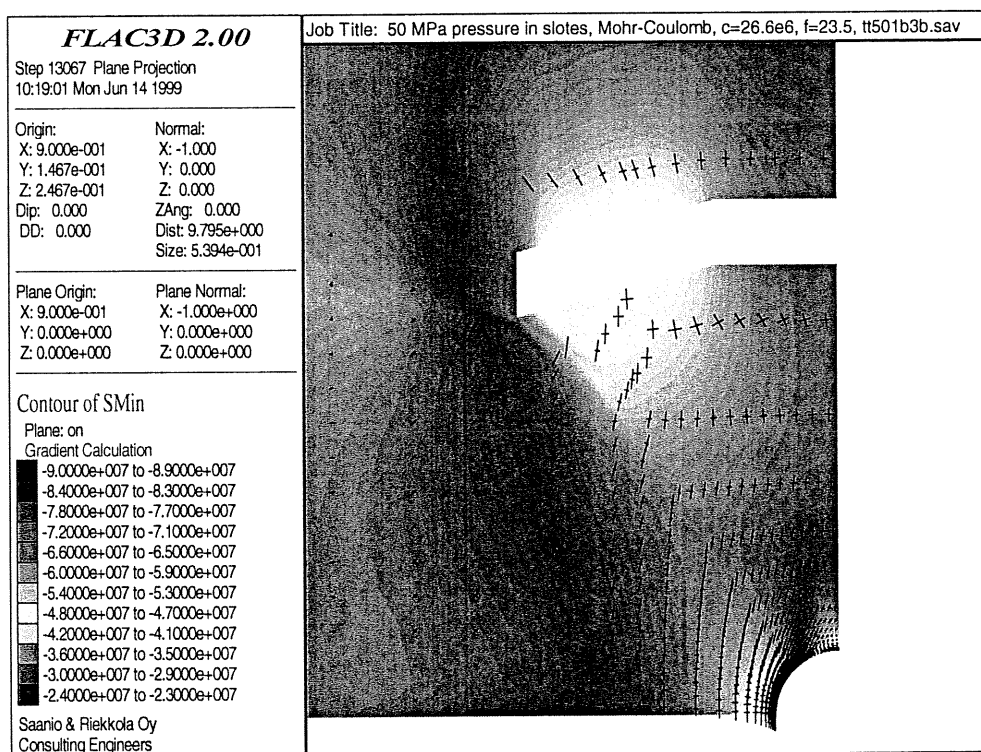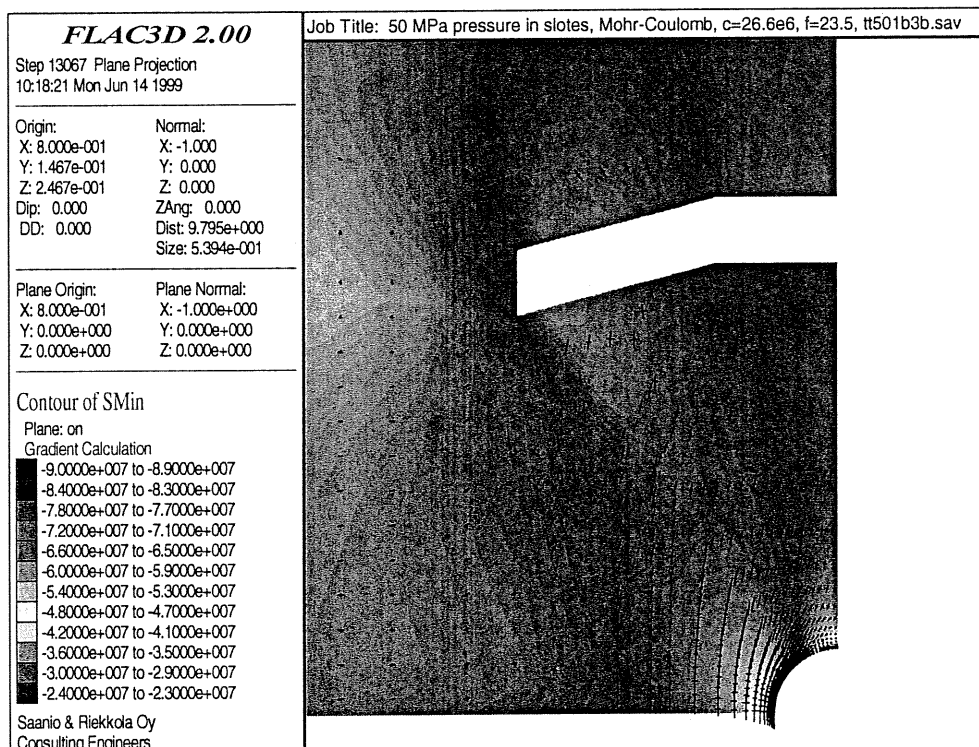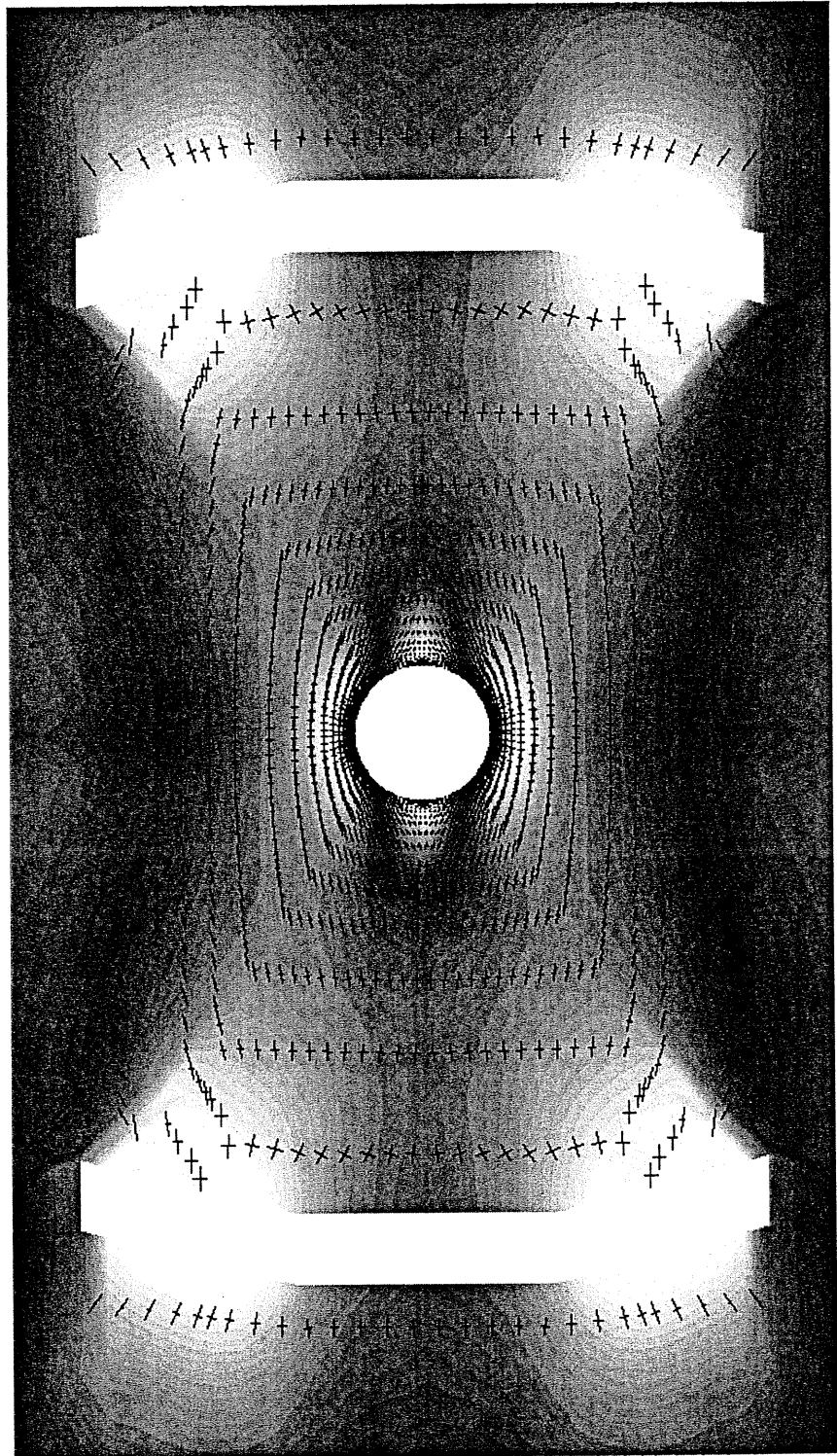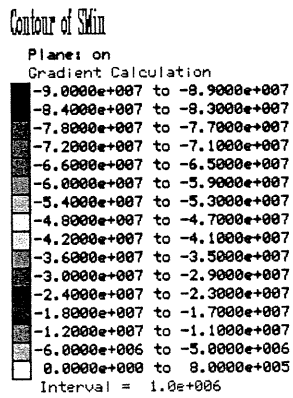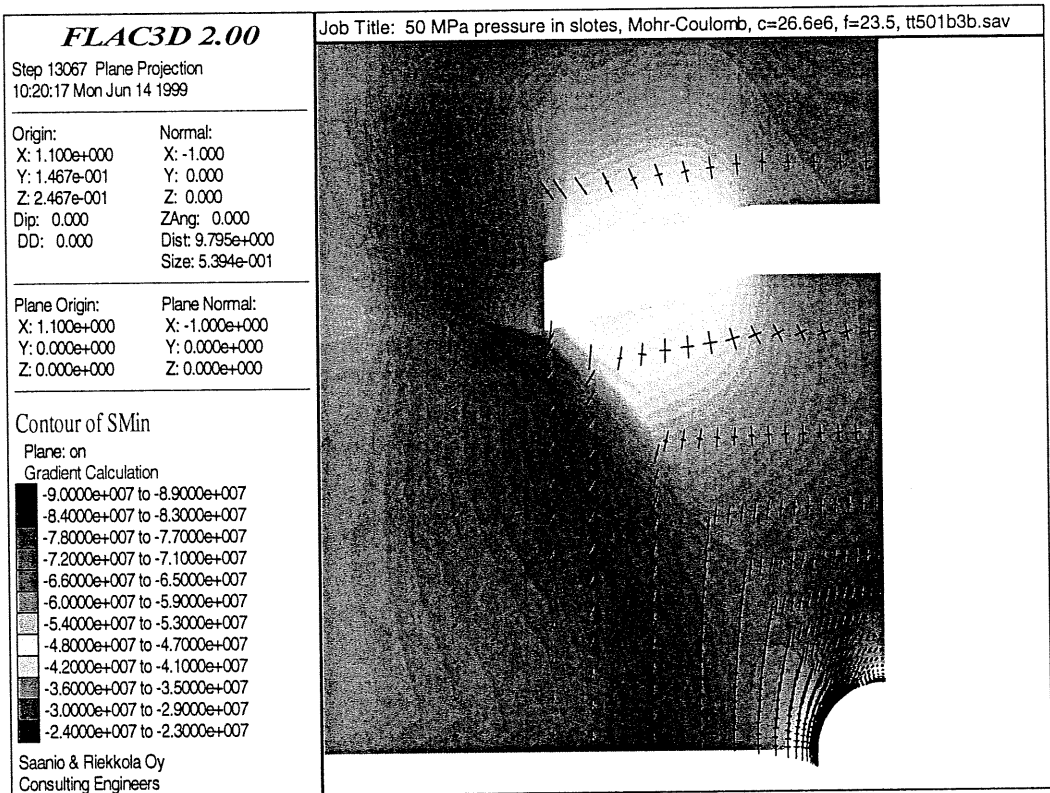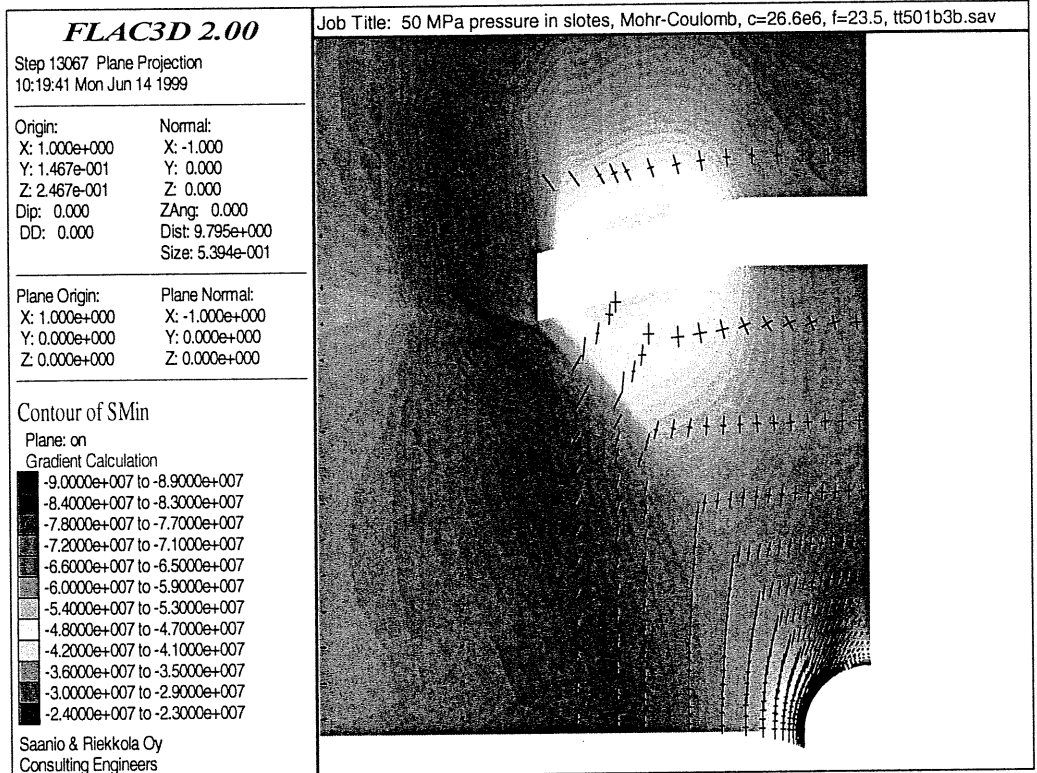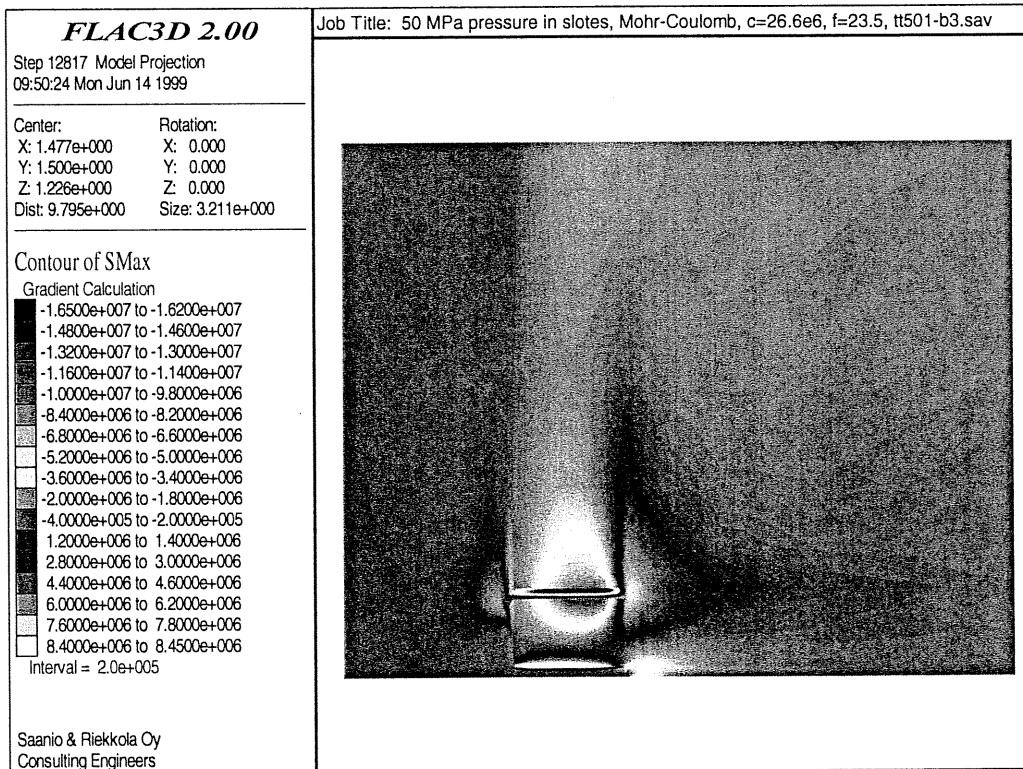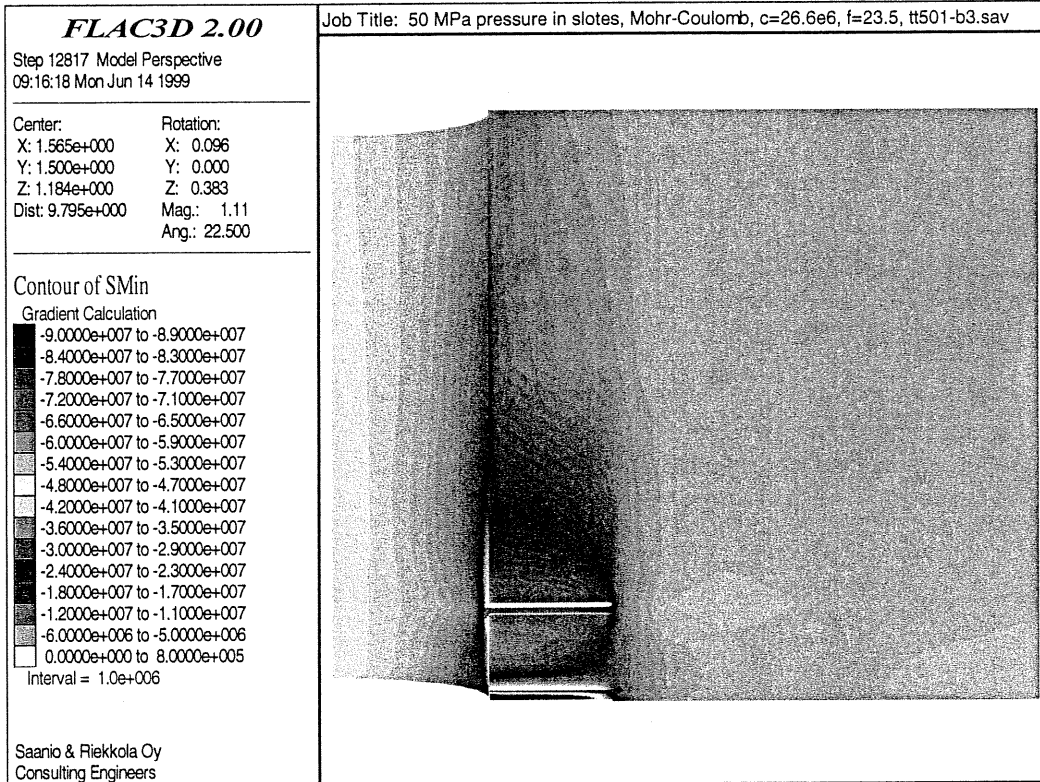
Figure 6.6-10. A vertical section taken perpendicular to the axis of the test hole showing the state of major σ_1 (top) and minor σ_3 stresses (bottom) with a swelling pressure of 50 MPa. Slot width and depth 500 mm, diameter of center hole 100 mm, no frontfilling.

FLAC3D 2.00

Step 12817 Model Projection
09:31:40 Mon Jun 14 1999

Center:	Rotation:
X: 9.941e-001	X: 0.000
Y: 1.500e+000	Y: 0.000
Z: 2.326e-001	Z: 0.000
Dist: 9.910e+000	Size: 6.071e-001

Plane Origin:	Plane Normal:
X: 0.000e+000	X: 0.000e+000
Y: 1.000e-003	Y: -1.000e+000
Z: 0.000e+000	Z: 0.000e+000

Contour of SMin
Gradient Calculation
-9.0000e+007 to -8.9000e+007
-8.4000e+007 to -8.3000e+007
-7.8000e+007 to -7.7000e+007
-7.2000e+007 to -7.1000e+007
-6.6000e+007 to -6.5000e+007
-6.0000e+007 to -5.9000e+007
-5.4000e+007 to -5.3000e+007
-4.8000e+007 to -4.7000e+007
-4.2000e+007 to -4.1000e+007
-3.6000e+007 to -3.5000e+007
-3.0000e+007 to -2.9000e+007
-2.4000e+007 to -2.3000e+007
-1.8000e+007 to -1.7000e+007
-1.2000e+007 to -1.1000e+007
-6.0000e+006 to -5.0000e+006

Saanio & Riekkola Oy
Consulting Engineers

Job Title: 50 MPa pressure in slotes, Mohr-Coulomb, c=26.6e6, f=23.5, tt501-b3.sav

FLAC3D 2.00

Step 12817 Plane Projection
09:34:23 Mon Jun 14 1999

Origin:	Normal:
X: 9.941e-001	X: 0.000
Y: 1.798e-001	Y: 0.000
Z: 2.326e-001	Z: -1.000
Dip: 180.000	ZAng: 180.000
DD: 0.000	Dist: 9.910e+000
	Size: 6.071e-001

Plane Origin:	Plane Normal:
X: 0.000e+000	X: 0.000e+000
Y: 0.000e+000	Y: 0.000e+000
Z: 1.000e-003	Z: -1.000e+000

Contour of SMin
Gradient Calculation
-9.0000e+007 to -8.9000e+007
-8.4000e+007 to -8.3000e+007
-7.8000e+007 to -7.7000e+007
-7.2000e+007 to -7.1000e+007
-6.6000e+007 to -6.5000e+007
-6.0000e+007 to -5.9000e+007
-5.4000e+007 to -5.3000e+007
-4.8000e+007 to -4.7000e+007
-4.2000e+007 to -4.1000e+007
-3.6000e+007 to -3.5000e+007
-3.0000e+007 to -2.9000e+007
-2.4000e+007 to -2.3000e+007
-1.8000e+007 to -1.7000e+007

Saanio & Riekkola Oy
Consulting Engineers

Job Title: 50 MPa pressure in slotes, Mohr-Coulomb, c=26.6e6, f=23.5, tt501-b3.sav

Figure 6.6-11. A vertical (top) and horizontal(bottom) section taken parallel to the axis of the test hole showing the state of major σ_1 stresses with a swelling pressure of 50 MPa. Slot width and depth 500 mm, diameter of center hole 100 mm, no frontfilling.

Figure 6.6-12. Vertical sections taken perpendicular to the axis of the test hole showing the state of major σ_1 stresses at depth of 50 mm (top) and 150 mm (bottom) with a swelling pressure of 50 MPa. Slot width and depth 500 mm, diameter of center hole 100 mm, no frontfilling.
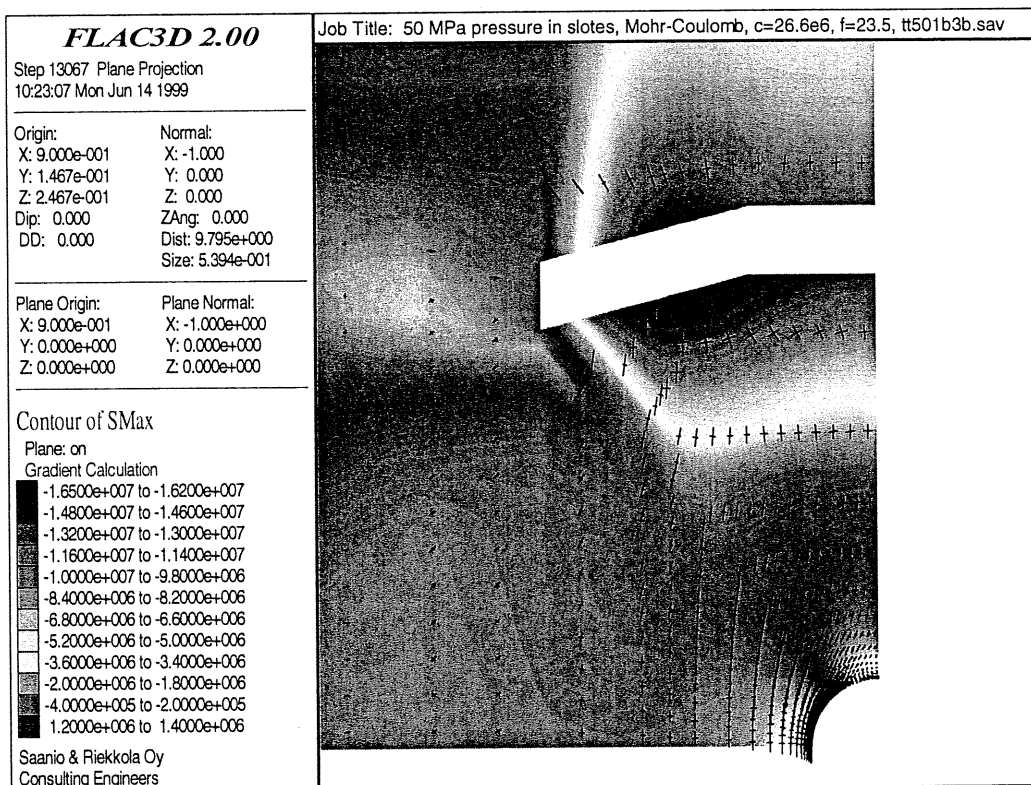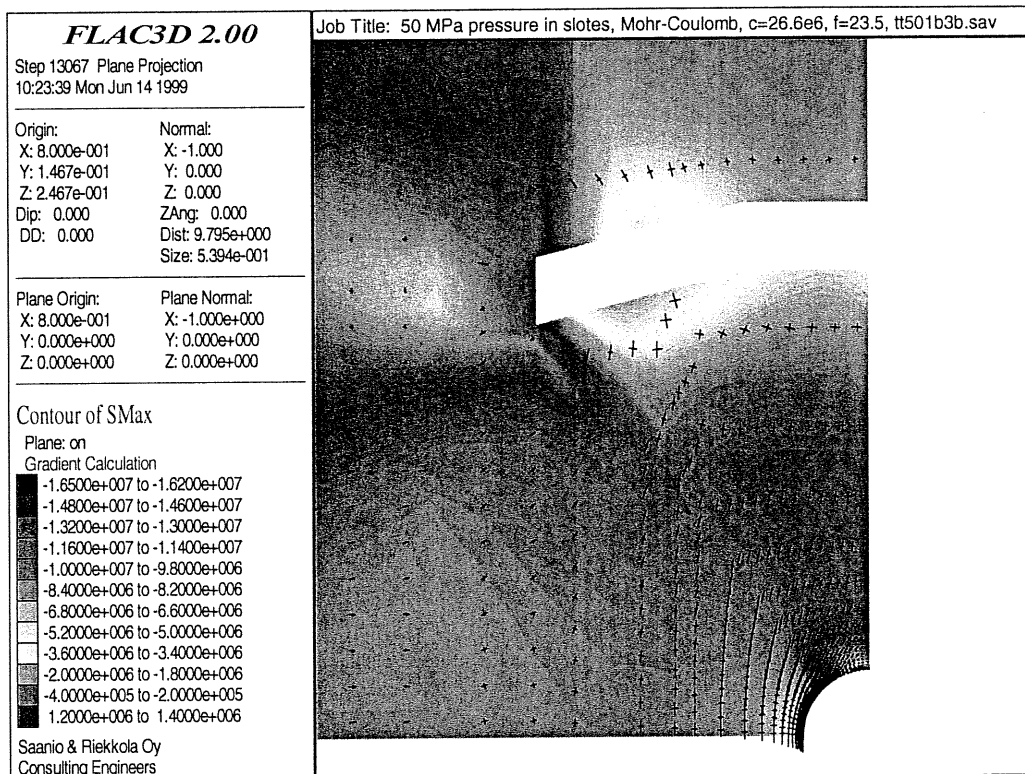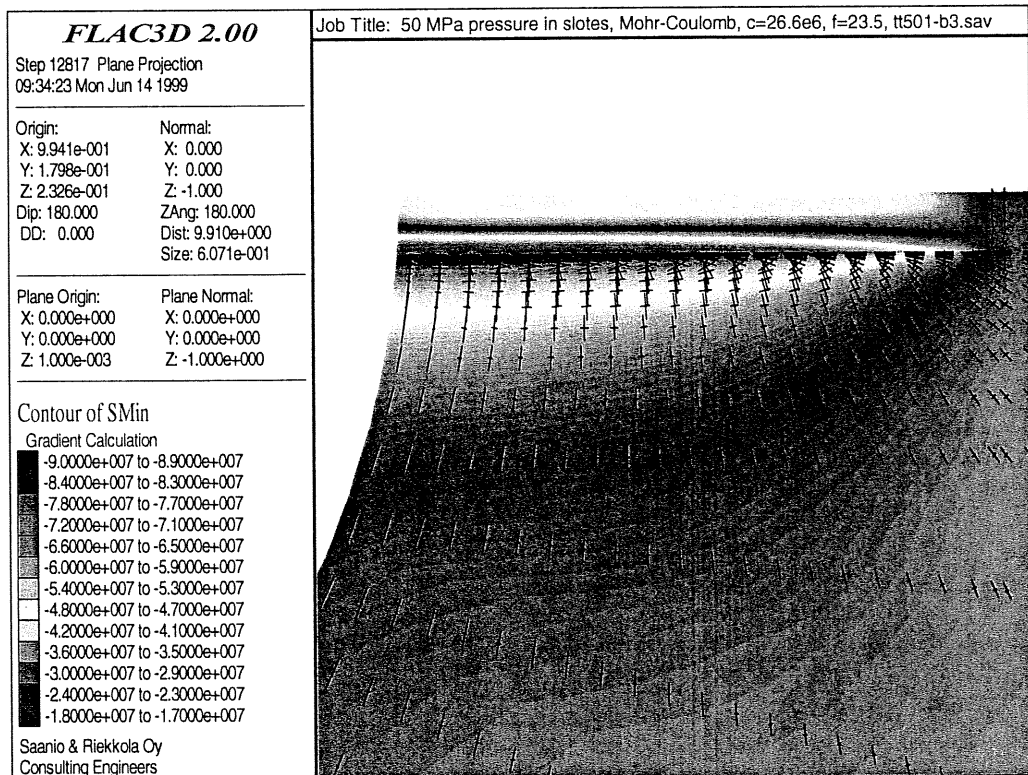
FLAC3D 2.00
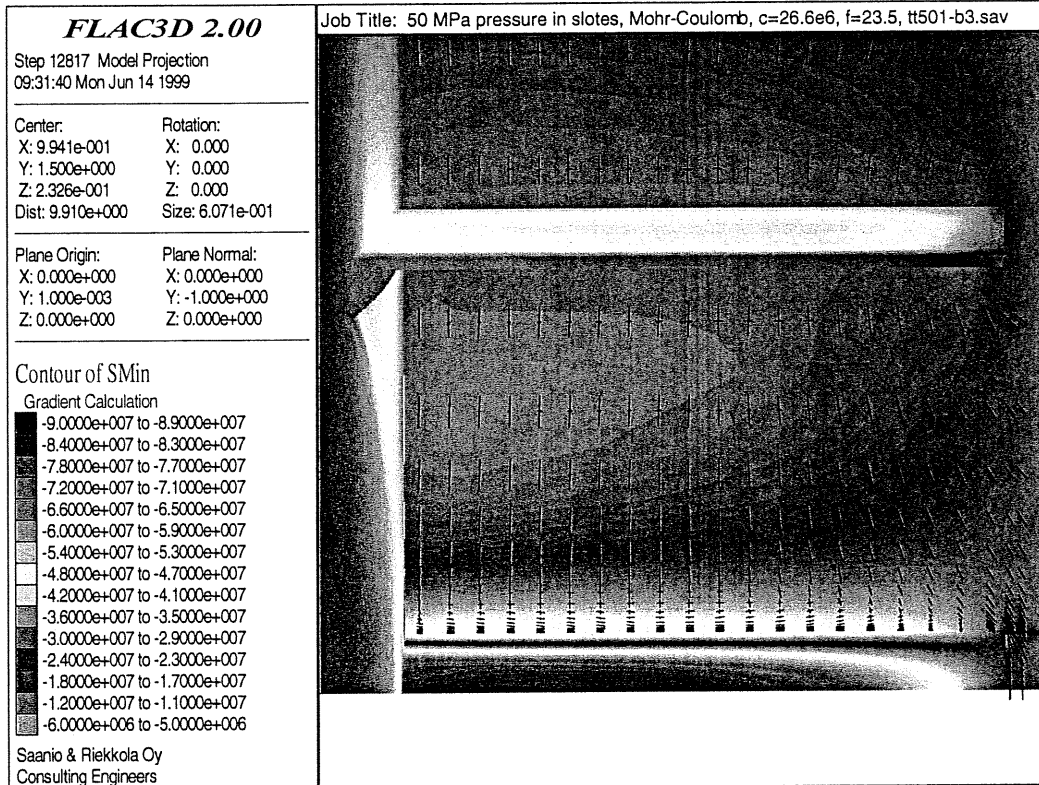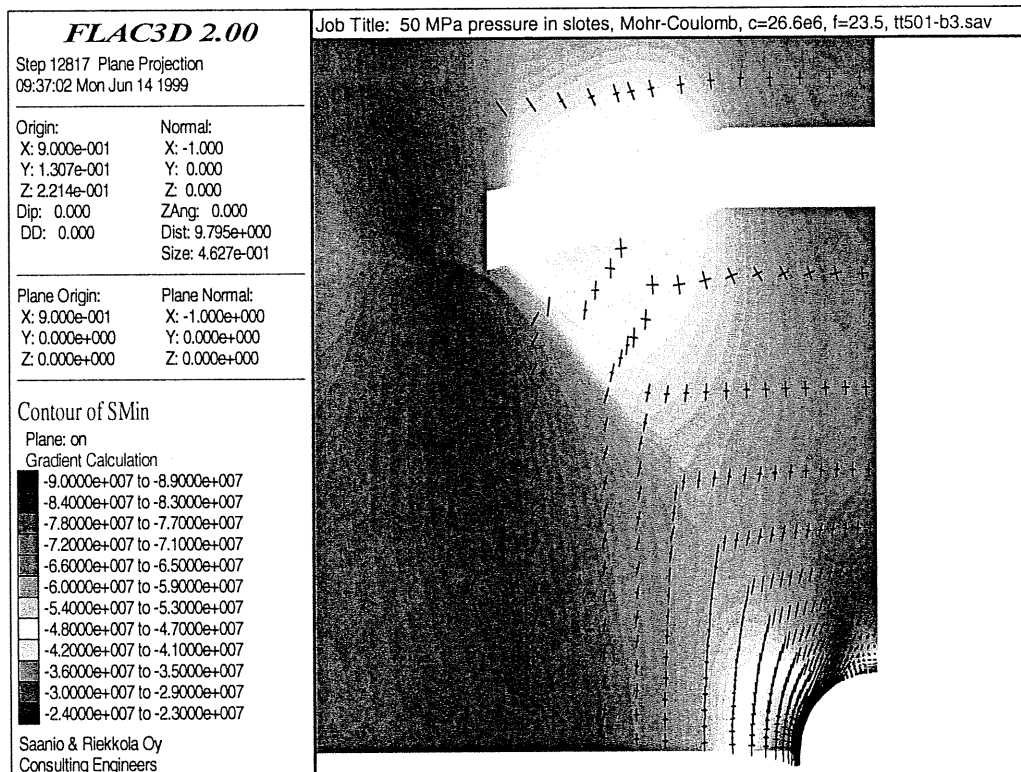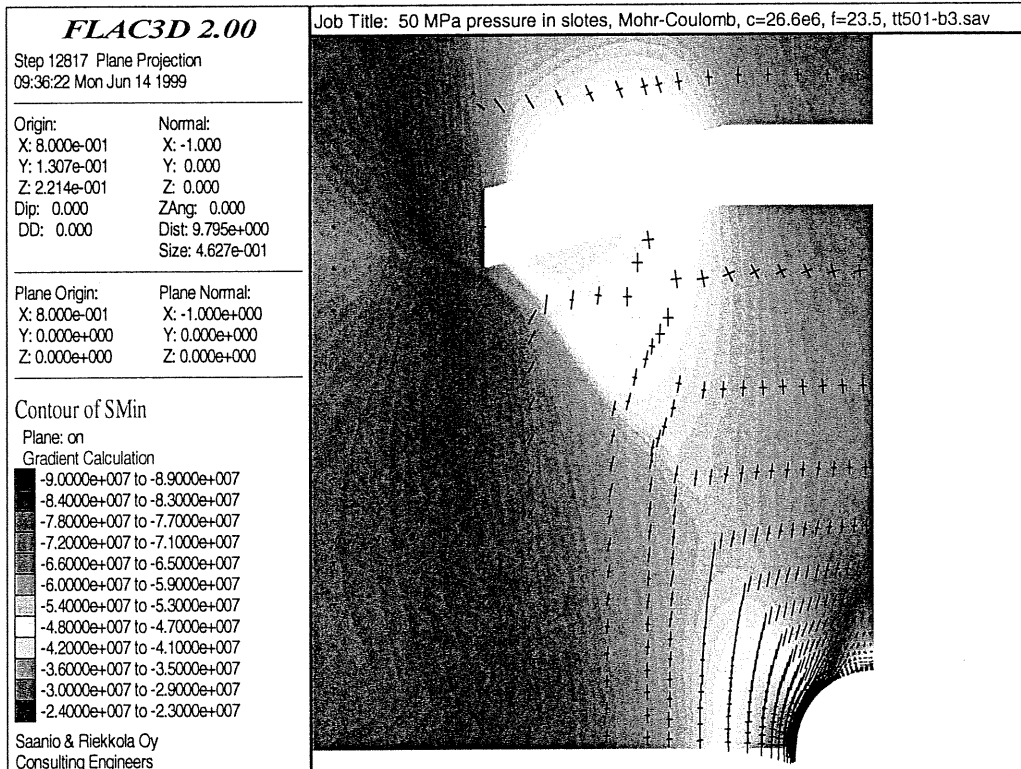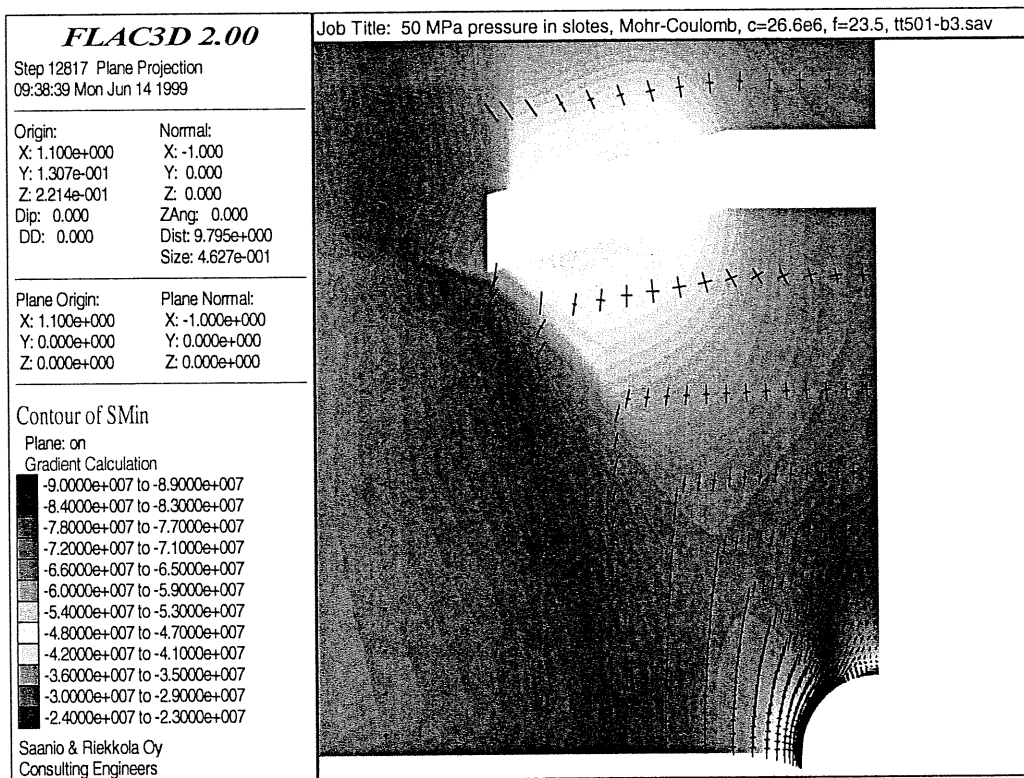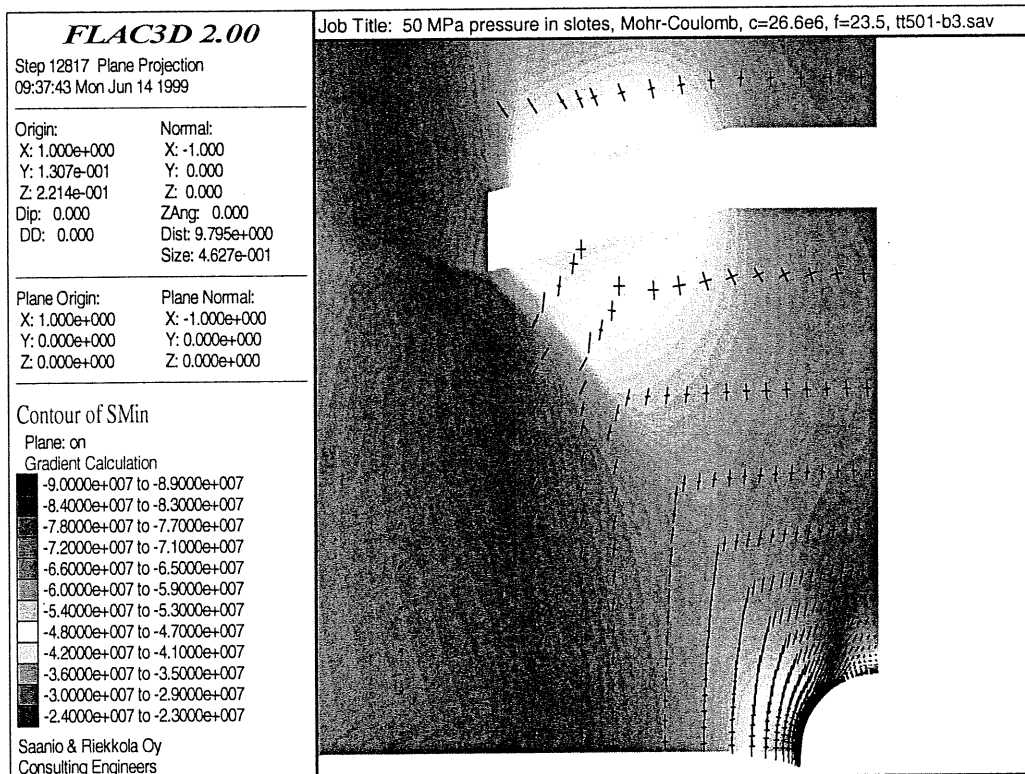
Step 12817 Plane Projection
09:37:43 Mon Jun 14 1999

Origin:	Normal:
X: 1.000e+000	X: -1.000
Y: 1.307e-001	Y: 0.000
Z: 2.214e-001	Z: 0.000
Dip: 0.000	ZAng: 0.000
DD: 0.000	Dist: 9.795e+000
	Size: 4.627e-001

Plane Origin:	Plane Normal:
X: 1.000e+000	X: -1.000e+000
Y: 0.000e+000	Y: 0.000e+000
Z: 0.000e+000	Z: 0.000e+000

Contour of SMin
  Plane: on
  Gradient Calculation
  -9.0000e+007 to -8.9000e+007
  -8.4000e+007 to -8.3000e+007
  -7.8000e+007 to -7.7000e+007
  -7.2000e+007 to -7.1000e+007
  -6.6000e+007 to -6.5000e+007
  -6.0000e+007 to -5.9000e+007
  -5.4000e+007 to -5.3000e+007
  -4.8000e+007 to -4.7000e+007
  -4.2000e+007 to -4.1000e+007
  -3.6000e+007 to -3.5000e+007
  -3.0000e+007 to -2.9000e+007
  -2.4000e+007 to -2.3000e+007

Saanio & Riekkola Oy
Consulting Engineers

Job Title: 50 MPa pressure in slotes, Mohr-Coulomb, c=26.6e6, f=23.5, tt501-b3.sav

FLAC3D 2.00

Step 12817 Plane Projection
09:38:39 Mon Jun 14 1999

Origin:	Normal:
X: 1.100e+000	X: -1.000
Y: 1.307e-001	Y: 0.000
Z: 2.214e-001	Z: 0.000
Dip: 0.000	ZAng: 0.000
DD: 0.000	Dist: 9.795e+000
	Size: 4.627e-001

Plane Origin:	Plane Normal:
X: 1.100e+000	X: -1.000e+000
Y: 0.000e+000	Y: 0.000e+000
Z: 0.000e+000	Z: 0.000e+000

Contour of SMin
  Plane: on
  Gradient Calculation
  -9.0000e+007 to -8.9000e+007
  -8.4000e+007 to -8.3000e+007
  -7.8000e+007 to -7.7000e+007
  -7.2000e+007 to -7.1000e+007
  -6.6000e+007 to -6.5000e+007
  -6.0000e+007 to -5.9000e+007
  -5.4000e+007 to -5.3000e+007
  -4.8000e+007 to -4.7000e+007
  -4.2000e+007 to -4.1000e+007
  -3.6000e+007 to -3.5000e+007
  -3.0000e+007 to -2.9000e+007
  -2.4000e+007 to -2.3000e+007

Saanio & Riekkola Oy
Consulting Engineers

Job Title: 50 MPa pressure in slotes, Mohr-Coulomb, c=26.6e6, f=23.5, tt501-b3.sav

Figure 6.6-13. Vertical sections taken perpendicular to the axis of the test hole showing the state of major σ_1 stresses at depth of 250 mm (top) and 350 mm (bottom) from the surface of the full-scale hole with a swelling pressure of 50 MPa. Slot width and depth 500 mm, diameter of center hole 100 mm, no frontfilling.
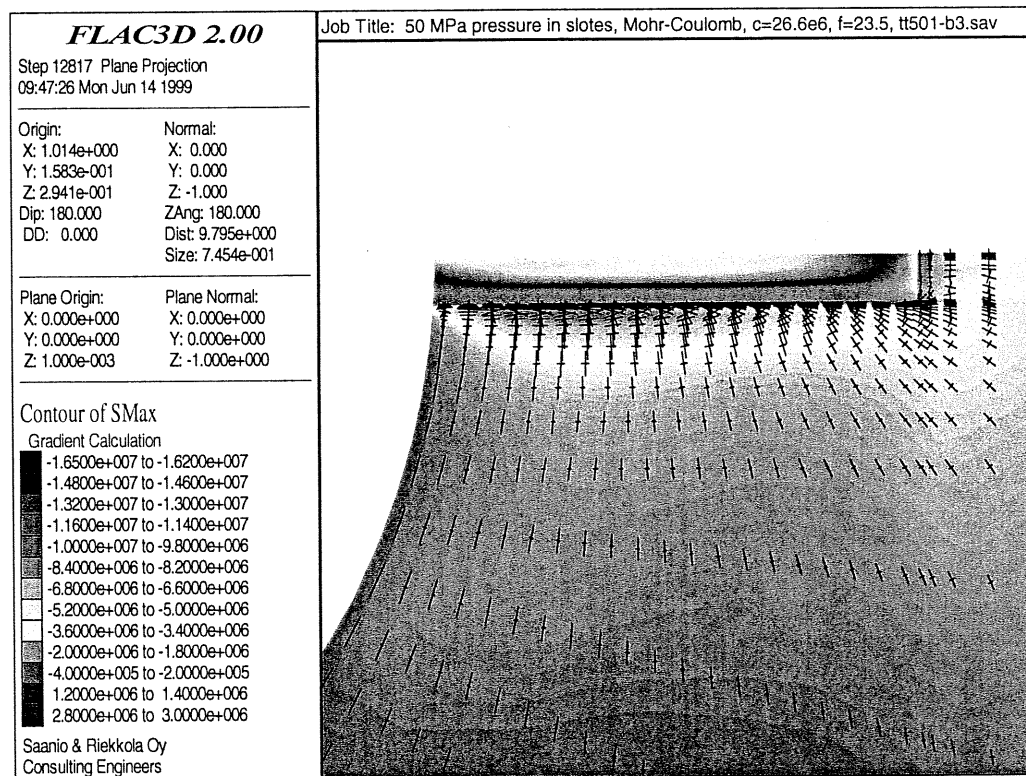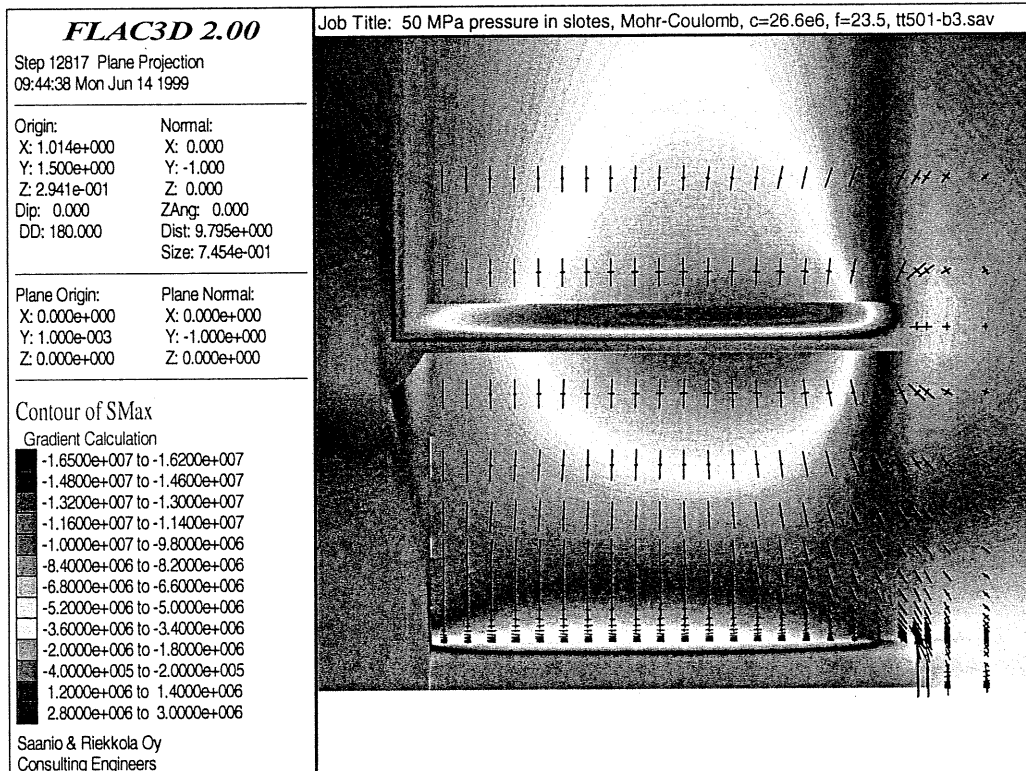
Figure 6.6-14. *A vertical (top) and horizontal (bottom) section taken parallel to the axis of the test hole showing the state of minor σ_3 stresses with a swelling pressure of 50 MPa. Slot width and depth 500 mm, diameter of center hole 100 mm, no frontfilling.*
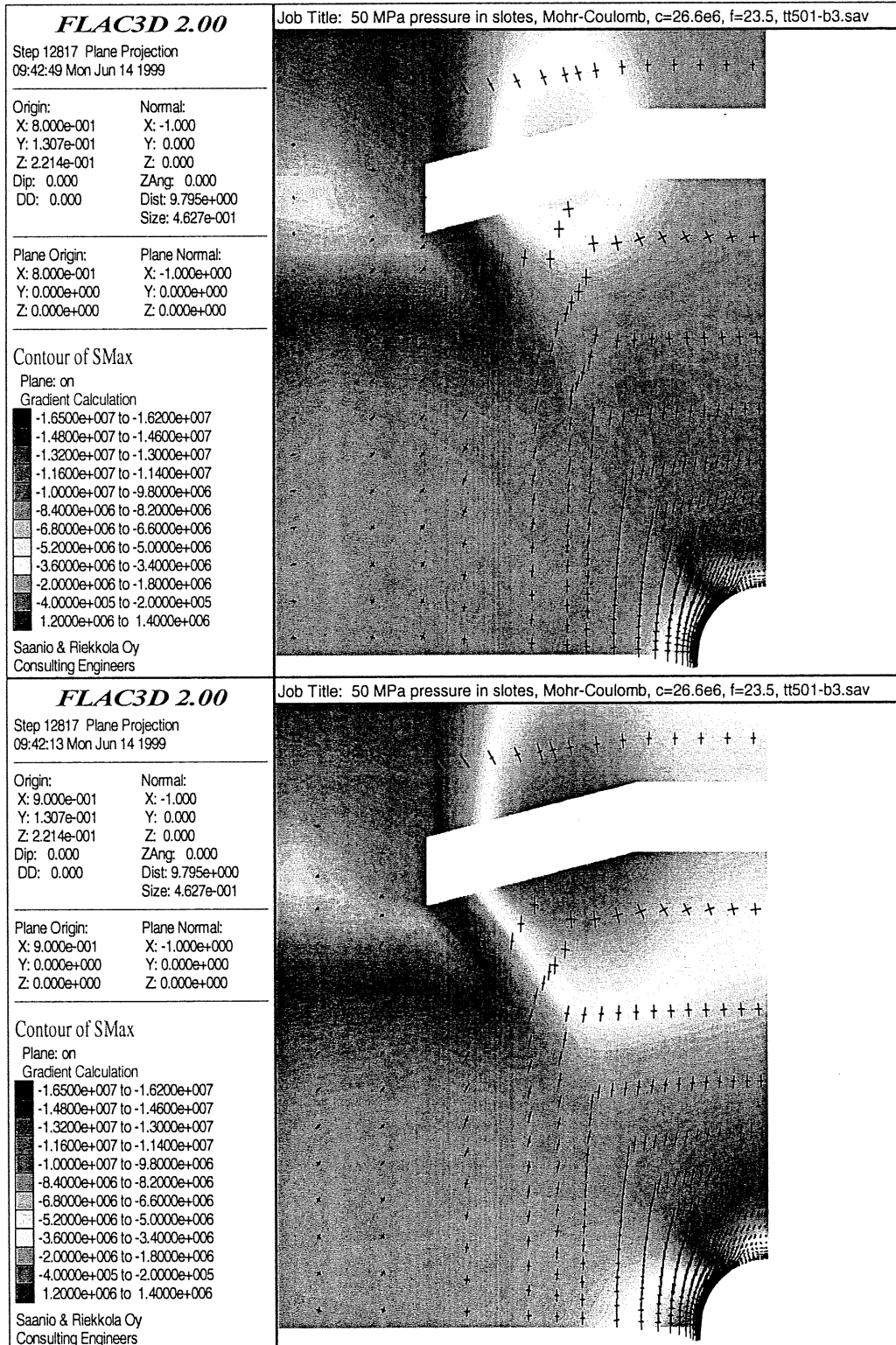
Figure 6.6-15. *Vertical sections taken perpendicular to the axis of the test hole showing the state of minor σ_3 stresses at depth of 50 mm (top) and 150 mm (bottom) with a swelling pressure of 50 MPa. Slot width and depth 500 mm, diameter of center hole 100 mm, no frontfilling.*
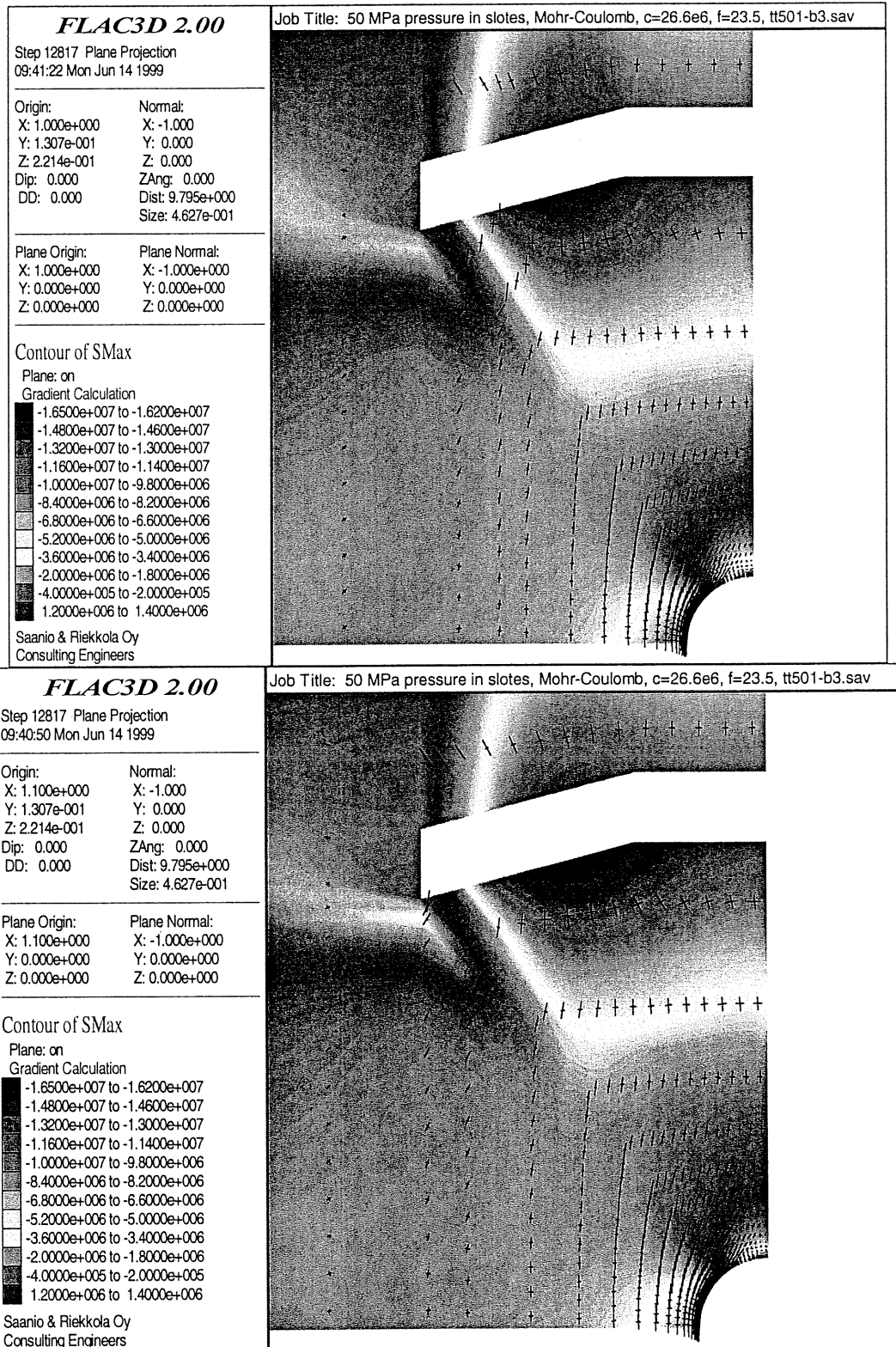
Figure 6.6-16. *Vertical sections taken perpendicular to the axis of the test hole showing the state of minor σ_3 stresses at depth of 250 mm (top) and 350 mm (bottom) with a swelling pressure of 50 MPa. Slot width and depth 500 mm, diameter of center hole 100 mm, no frontfilling*
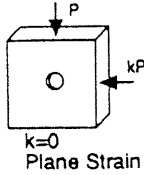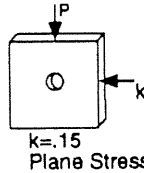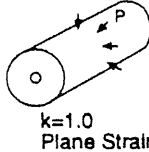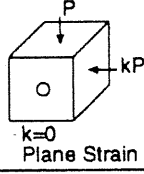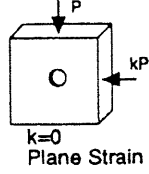
6.7 Litterature review of failure of circular openings

The failure strength of circular openings has been studied by many researchers and a summary of these presented by Martin (1994) is shown in Figure 6.7-1.

Test Set Up	Rock Properties	Sample and Hole Dimensions (mm)	(1) Failure Stress in terms of σ_c	Reference
k=0 Plane Strain	Tyndall Limestone $\sigma_c = 41$ MPa E = 4.2 GPa v = 0.31	305 x 305 x 89 5 to 61 mm φ	For 5 mm φ 2.4 σ_c For 61 mm φ 1.5 σ_c	Carter, 1991
k=.15 Plane Stress	Chert $\sigma_c = 579$ MPa E = 82 GPa v = 0.2	127 x 127 x 3 19 mm φ	1.19 σ_c	Hoek, 1966
k=1.0 Plane Strain	Sandstone $\sigma_c = 44 - 74$ MPa E = 20 GPa v = 0.26	O.D. = 89 I.D. =25.4	2-3 σ_c	Ewy and Cook, 1990
k=0 Plane Strain	Alabama Limestone $\sigma_c = 43$ MPa E = ? GPa v = ?	180 x 130 x 130 25 to 110 mm φ	For 25 mm φ 2.6 σ_c For 110 mm φ 0.81 σ_c	Haimson and Herrick, 1989
k=0 Plane Strain	Sandstone $\sigma_c = 44 - 74$ MPa E = 20 GPa v = 0.26	203 x 203 x 89 45 mm φ	For 45 mm φ 1.84-1.9 σ_c	Mastin, 1984

(1)Failure is defined as the first indication of hole sidewall instability.

Figure 6.7-1. Summary of the various boundary conditions used to investigate failure around circular openings (Martin 1994).

Carter and Haimson&Herrick studied the behaviour of limestone and found out that as the size of the circular opening increases, the failure strength of the rock in the sidewall becomes lower and approaches the uniaxial compressive strength of the rock which is reached at a diameter of about 75 mm or larger.

The strength of similar small circular openings ranging in diameter from 20 to 103 mm in eleven Lac du Bonnet granite blocks was also studied in a laboratory at the

University of Manitoba (Martin 1994). An example of the largest experimental arrangement, which actually is quite close to the proposed geometry for the in-situ failure test, is shown in Figure 6.7-2 (Martin 1994) and a summary of the results obtained, including results by Carter (1992) and Haimson&Herrick (1989), is shown in Figure 6.7-3.
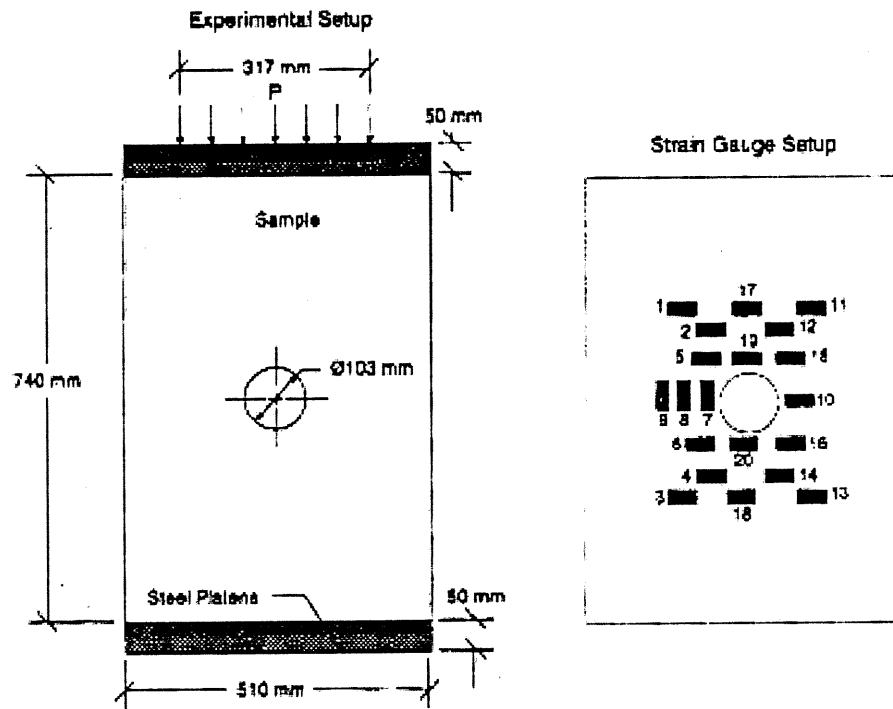

Figure 6.7-2. An example of the largest experimental arrangement used to study the failure strength of circular openings in Lac du Bonnet granite (Martin 1994).
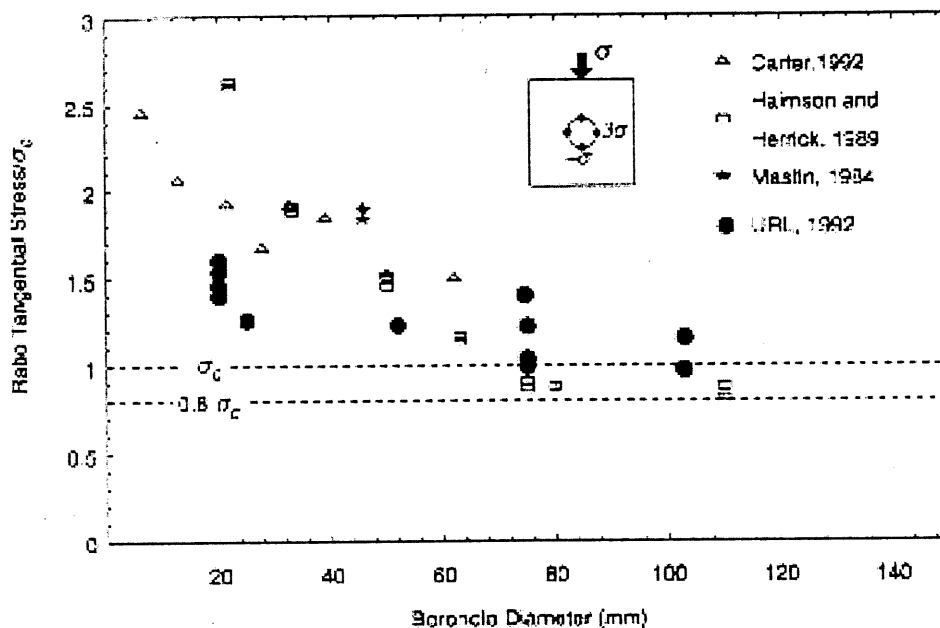

Figure 6.7-3. Summary of studies on the failure strength of circular openings in rock blocks (Martin 1994).

The results of testing Lac du Bonnet granite agreed with the other results shown in Figure 6.7-3 and showed that the sidewall strength was reduced when the diameter of the opening was increased, becoming equal to the uniaxial compressive strength of the rock at diameters between 75 and 103 mm. More interesting was the observation by Martin (1994) that at larger diameters than about 100 mm the scale effect disappeared, and this was supported by field evidence from URL showing similar spalling in 3.5 m and 75 mm diameter openings subjected to the same stress conditions.

According to modelling results a tangential stress large enough to cause sidewall failure of the centre hole in the proposed in-situ test should be close to the uniaxial compressive strength and this (approximately 90 MPa) should be achieved since an expanding agent pressure of 50 MPa produces tangential stress of about 100 MPa. Before this state is reached, some tensile fracturing may also have occurred on the roof and bottom sections of the hole.

The three types of fractures shown in Figure 6.7-4. have been identified as occurring when the rock around a circular opening fails. The most common type found in both the field and in the laboratory is spalling caused by high compressive stress which results in a v-notch shaped failure zone. Other types of fracture found in laboratory tests are tensile fractures and remote fractures which are also given the names of primary and secondary fractures respectively. The failures observed in a laboratory test (see Figure 6.7-5 for the dimensions) carried out on a circular opening with a radius of 30.3 mm in a block of Lac Du Bonnet granite employing a configuration that resembles the proposed in-situ failure test in its geometry, scale and loading are of interest. The block was loaded by increasing the axial and confining loads simultaneously until the confining stress was 15 MPa. The confining stress was then maintained at 15 MPa and the axial load was increased (Martin 1994).
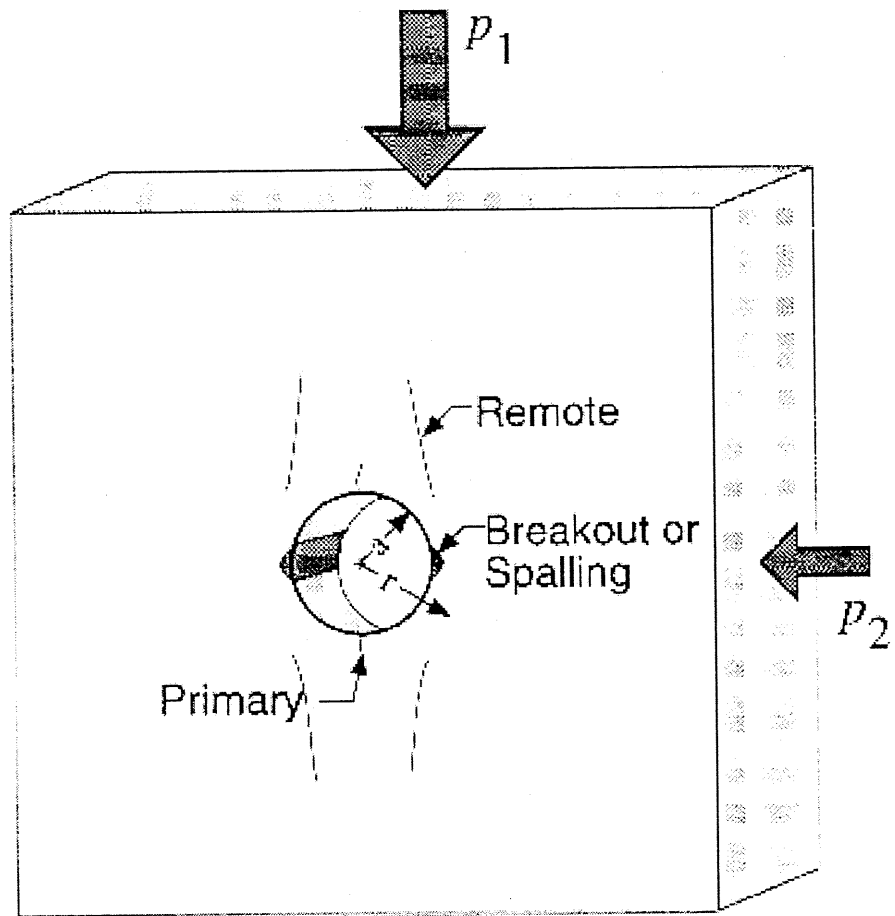
Figure 6.7-4. *Three different types of fractures around circular openings in rock blocks (Martin 1994).*
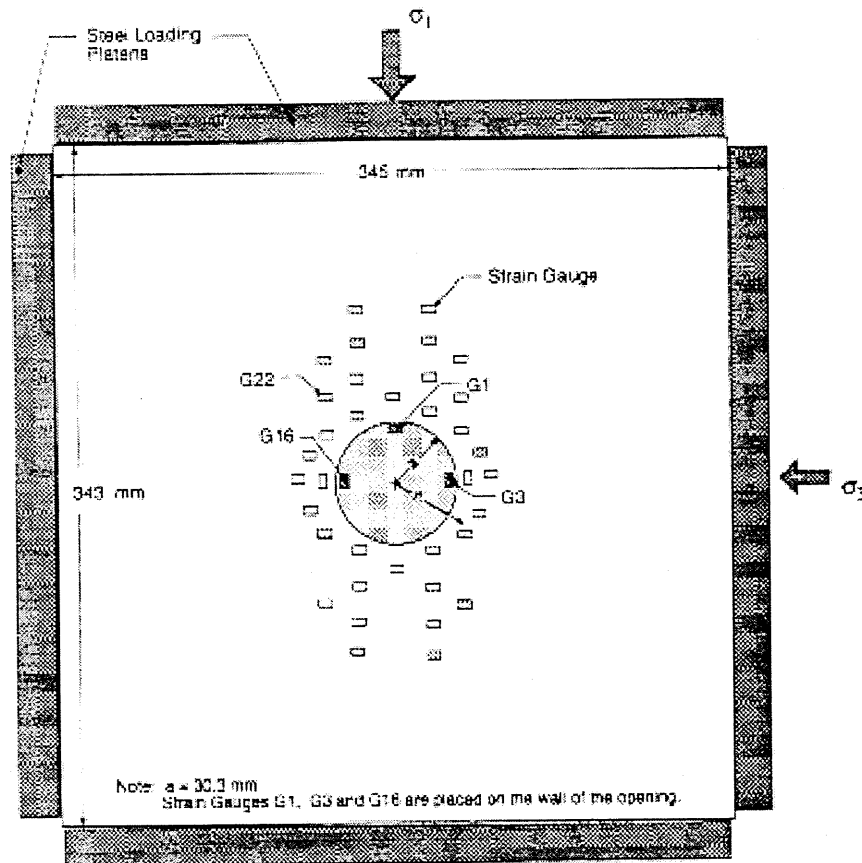
Figure 6.7-5. An experimental arrangement used to study the failure strength of circular openings in Lac du Bonnet granite (Martin 1994).

In this test, the first fractures observed were primary fractures of length equal to one radius of the circular opening at a relatively-low applied stress of between 10 and 20MPa. The second type of fracture was sidewall spalling at an applied stress of approximately 60 MPa and this was followed by the occurrence of remote fractures at an applied stress of approximately 100 MPa.

7 MONITORING AND INSTRUMENTATION

The objective of the monitoring process is to confirm the functioning of the test (i.e. the pressure development in the slots), to provide information about when to stop pressure generation, to provide accurate input data on stresses and failure for later modelling of the test and to provide general information about the failure process.

All the instrumentation must be installed so that it does not interfere with the test. According to the preliminary plans, the following acitivities will be monitored:

a)   Slots:
        -pressure
        -temperature.

b)   Centre hole:
        -macroscopic fracturing
        -strains
        -temperature in different parts of the surface.

c)   Test area:
        -acoustic emission.

Acoustic emissions will be monitored to track fracture generation around the centre hole and at the corners of slots. The preliminary plan is to drill four small diameter (30-60 mm) holes around the test configuration in the full-scale deposition hole for the installation of acoustic emission transducers. The suggested length of the holes is 1.0 to 1.5 m.

Deformation at the surface of centre hole will be measured by installing several rings of strain gauges at different depts from the mouth of the centre hole. The surface of the hole will also be monitored using video to detect macroscopic fractures. In principle, the technique to be used will be very similar to that used to execute the in-situ stress measurements presented in Chapter 4.2.

Pressure and temperature in the expanding agent will be monitored using thermocouples and pressure transducers. Pressure generation will be stopped after failure occurs around the central hole.

8   CONCLUSIONS

The modelling presented in Chapter 6 provides an estimation of the distribution of stresses when the state of stress is less than the strength of the rock. The earlier input data used for numerical modelling didn't differ significantly from the average of latest data presented in Chapter 3 and 4 and therefore the results are representative the main difference being the anisotropy of rock which was not included in the model. After failure appears and fractures start to propagate the results of modeling are not valid and a description of the fracturing can be obtained from the results of reported laboratory tests (see Chapter 6.7) of similar size of circular openings. The failure patterns associated with primary and spalling fractures in the in-situ test are expected to be very similar but it is possible that remote fractures will not be not generated.

Since the rock in the in-situ test has a clear orientation and the orientation also clearly affects the strength properties of the rock, it is evident that the generation of fractures and failure patterns will be guided by the most favourable orientation for crack propagation. The most favourable direction for primary tensile fractures is along the schistocity planes.

An illustration of the preliminary geometry of the test with respect to orientation is shown in Figures 8-1 and 8-2. The test hole is parallel to the schistocity plane and therefore the experimental arrangement is as close to two dimensional as possible.

The main results predicted by the work described are as follows:
- that failure will occur around the central hole of the test configuration in the form of primary tensile fractures and sidewall spalling,
- that failure will be initiated at what are technically relatively-low pressure levels (50 MPa) produced by the expanding agent,
- that the areas in which failure will take place will be the top, the bottom and the sides of the holes (see Figure 6-1 and 6-2),
- that failure will also take place at the corners of the slots,
- that failure on the surface of the full-scale deposition hole and at the corners of the slots will cause local unloading and stress re-distribution, and
- that slight curvature of the slots, which is beneficial from the experimental point of view, does not have a significant effect on the stress distribution around the central hole of the test configuration,
- the properties of the expanding agent were tested in laboratory scale. The heat generation during expansion was significant and may result in blow out. The technique used to create the required high stress is critical and cannot be easily replaced. Therefore the technique has to be tested in a real scale before execution of the test.
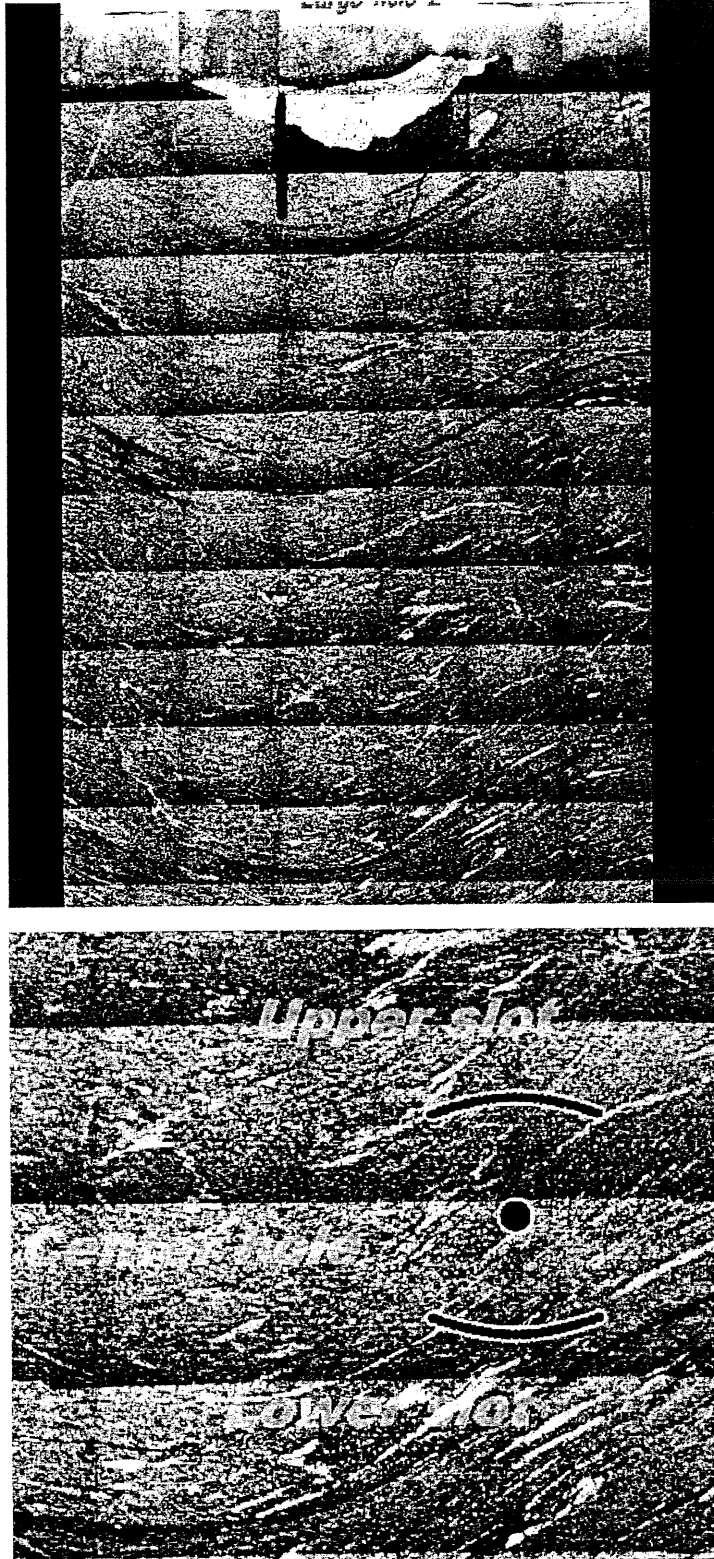
Figure 8-1. *Preliminary experimental arrangement for the in-situ failure test with respect to the orientation of the gneissic tonalite in full-scale experimental deposition hole 2. Photomosaic of the surface of hole (top) and close-up of the preliminary test arrangement (bottom).*
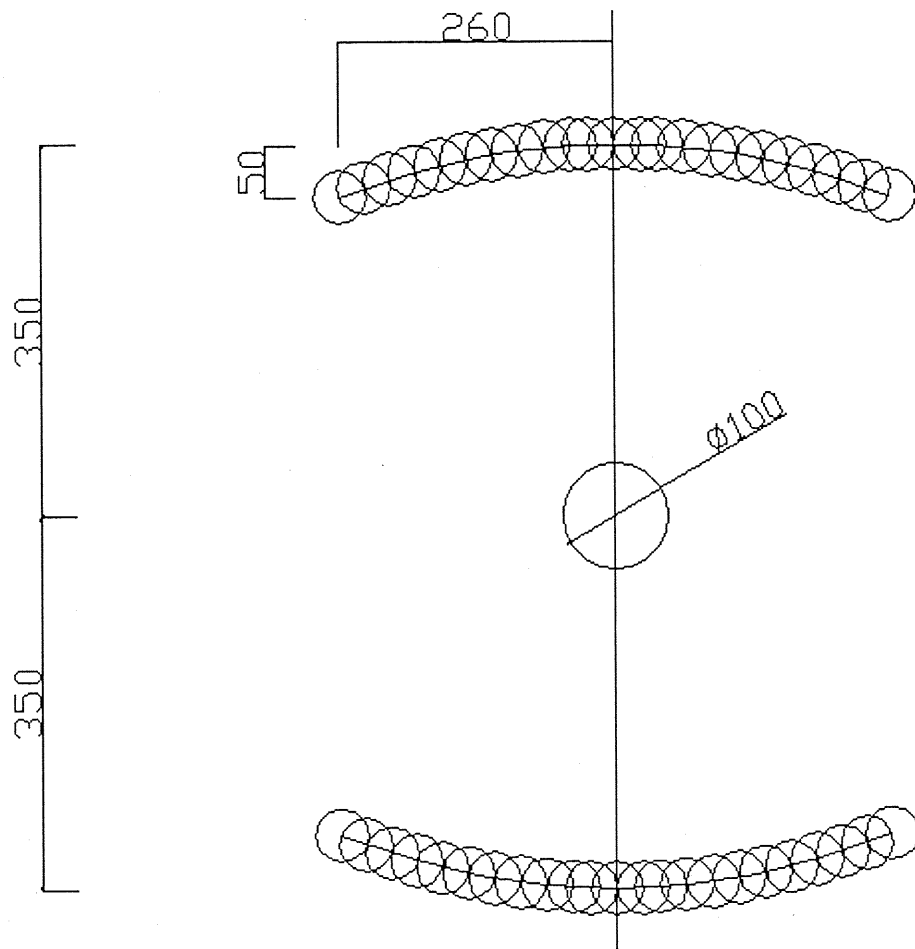
Figure 8-2. Preliminary dimensions of the experimental arrangement for the in-situ failure test shown in Figure 8-1.

REFERENCES

Amadei, B. 1983. Rock Ansisotropy and the Theory of Stress Measurements. Lecture notes in engineering edited by C.A. Brebbia and S.A. Orszag. Springer-Verlag Berlin, Germany. pp. 50-52.

Andreev, G. 1995. Brittle Failure of Rock Materials, Test Results and Constitutive Models. Balkema, Rotterdam.

Autio, J. 1996. Characterization of the excavation disturbance caused by boring of the experimental full scale deposition holes in the Research Tunnel at Olkiluoto. Report POSIVA-96-09, POSIVA Oy, Helsinki and and similar report PR D-96-030 in SKB's (Svensk Kärnbränslehantering AB, Stockholm) report series.

Autio, J., Äikäs, T. & Kirkkomäki T. 1995. Coring and description of samples from the full scale experimental deposition holes at TVO/Research Tunnel. Helsinki. Teollisuuden Voima Oy. Work Report TEKA-95-02 and similar report AR D-95-003 in SKB's (Svensk Kärnbränslehantering AB) report series.

Autio, J., Kirkkomäki, T., Siitari-Kauppi, M., Timonen, J, Laajalahti, M., Aaltonen, T. & Maaranen, J. 1999. Use of the ^{14}C-PMMA and He-gas methods to characterize excavation disturbance in crystalline rock. Report Posiva- 99-22, Posiva Oy, Helsinki and similar report IPR-99-18 in SKB's (Svensk Kärnbränslehantering AB, Stockholm) report series.

Carter, B. 1992. Size and stress gradients effects on fracture around cavities. Rock Mech. and Rock. Engnin., 25(3): 167-186.

Chandler, N., Read, R. & Wan, A. 1996. Implications of the Results of URL experiments on the Design of Repository Seals in Granite. Proc. Int. Conf. On Deep Geological Disposal of Radioactive Waste, Sept. 16-19, 1996, Winnipeg, Canada. Canadian Nuclear Society, Toronto, Canada, pp. 7-1 – 7-10.

Donath, F. 1964. Strength variations and deformational behaviour in anisotropic rock. In State of Stress in the Earth's Crust, ed. W.R. Judd. Elsevier, Newe York, 1964, pp. 281-297.

Eloranta, P. & Hakala, M. 1998. Laboratory testing of Kivetty porphyritic granodiorite in borehole KI-KR10. Working Report 98-49, Posiva, Helsinki.

Haimson, B. & Herrick, C. 1989. Borehole breakouts and in situ stress. In proc. 12th Annual Enenrgy Sources Technology Cof.&Exhibition, Drilling Symp., pages 17-22. American Soc. Mechanical Eng., New York.

Haimson, C.B. & Song I. 1995. A new borehole failure criterion for estimating in situ stress from breakout span. proc. of 8th Int. Congr. on Rock Mechanics. AA Balkema, Rotterdam.

Hakala M. 1996. Stress-Strain Behaviour of Crystalline Rock - Literature Study and Development of Test Program. Work Report TEKA-96-08e. Posiva Oy, Helsinki.

Hakala, M. 1998. Particle mechanical aspect of stress-strain behaviour in rock. Posiva report 98-77, Posiva, Helsinki.

Hakala, M. & Heikkilä, E. 1997. Development of Laboratory Tests and the Stress-Strain Behaviour of Olkiluoto Mica Gneiss, Summary report. Report 97-04, Posiva, Helsinki.

Hakala, M. & Somervuori, P. 1997. Numerical simulation of Expansive Agent Configuration. Espoo, Gridpoint Finland Oy, Work Report. 17 p.

Hakala, V-A. 1998. Measuring of rock strain in the Research Tunnel at Olkiluoto. Helsinki University of Technology, Structural Engineering Research Laboratory, Report RKH-106-98. 26 p.

Heikkilä, E. 1997. Pressure and temperature development of expansive agent Demex. Helsinki University of Technology, Laboratory of Rock Engineering, Test Report Mak-Kal 10/97. 22 p.

Heikkilä, E. & Hakala, M. 1998. Laboratory testing of Romuvaara tonalite gneiss in borehole RO-KR10. Working Report 98-06e, Posiva, Helsinki.

Helsinki University of Technology 1998. Report RKH-106-98. Measuring of Rock Strain in the Research Tunnel at Olkiluoto. 15 p.

Hoek, E. & Brown E. T. 1980. Underground excavations in rock. The Institutuion of Mining and Metallurgy, London England. pp. 159-162.

Itasca Consulting Group 1994. 3DEC, Three Dimensional Distinct Element Code. Version 1.5 manual. Itasca Consulting Group, Minneapolis.

Itasca Consulting Group 1995a. FLAC^{2D}, Fast Lagrangian Analysis of Continua in Two Dimensions. Version 3.3-manual. Itasca Consulting Group, Minneapolis.

Itasca Consulting Group 1995b. FLAC^{3D}, Fast Lagrangian Analysis of Continua in Three Dimensions. Version 1.0 manual. Itasca Consulting Group, Minneapolis.

Jaeger, J. C. & Cook, N.G.W. 1979. Fundamentals of rock mechanics, 3rd edn.,. Chapman and Hall, London.

Johansson, E. 1994. Rock Mechanical Properties of Intact Rock in TVO's Test Boring Site in Boliden, Sweden. Helsinki. Teollisuuden Voima Oy. Work Report TEKA-94-15.

Johansson, E. & Autio, J. 1993. Rock Mechanical properties of intact rock in TVO's research tunnel. August 1993, TEKA-93-05

Johansson, E. & Autio, J. 1995. Properties of rock in TVO research tunnel and investigation sites. Work Report TEKA-95-10, Teollisuuden Voima Oy (TVO), Helsinki.

Kuula, H. & Johansson, E. 1991. Rock mechanical stability of the VLJ-repository. Helsinki, Nuclear Waste Commission of Finnish Power Companies, Report YJT-91-03. (In Finnish).

Lajtai, E., Schmidtke, R. & Bielus, L. 1987. The effect of Water on the Time-Dependent Deformation and Fracture of a Granite. Int. J. Rock Mech. Min. Sci. & Geomech. Abstr., Vol. 24, No. 4, pp. 247-255.

Landolt & Börnstein 1982. Numerical Data and Functional Relationships in Science and Technology, Vol. V/1a, Physical properties of rock, Springer Verlag 1982.

Lau, J., Gorski, B. & Jackson, R. 1996. Some rock mechanics testing related to the construction and operation of AECL's Underground Research Laboratory (URL). Proc. of Int. Conf. on Deep Geological Disposal of Radioactive Waste, Winnipeg, Manitoba, Canada. p. 7-37.

Lockner, D. 1993. The Role of Acoustic Emission in the Study of Rock Fracture. Int. J. Rock Mech. Min. Sci.&Geomech. Abstr. Vol.30, No.7, pp. 883-899. Pergamon Press Ltd, Great Britain.

Martin C. D. 1994. TVO/SKB/AECL Workshop on Rock Strength - Proceedings. Work Report TEKA-94-07. Teollisuuden Voima Oy, Helsinki.

Martin, C. D. 1994. Brittle Rock Strength. TVO & SKB Workshop April 1994 at Helsinki . AECL Research, Pinawa, Manitoba, Canada.

Moore, D. E. & Lockner, D. A. 1995. The role of microcracking in shear-fracture propagation. J. of Structural Geology, Vol.17, No.1, pp. 95 –114. Elsevier Science Ltd, Great Britain.

Nykyri, M., Riekkola, R., Äikäs, K., Johansson, E. & Kuula, H. 1991. Underground repository for low and intermediate level radioactive waste at Olkiluoto, Finland. Proc. of 7th Inr. Congr. on Rock Mechanics. AA Balkema, Rotterdam.

Nykyri, M., Helenius, J., Johansson, E. & Nieminen, J. 1994. Monitoring of the bedrock in the VLJ Repository in 1992. Work report VLJ 94-02. Teollisuuden Voima Oy, Helsinki (in Finnish).

Optiroc 1996. Instructions of use for Demex. Optiroc Oy Ab. Helsinki 2.

Pirhonen, V. &Laaksonen, R. 1997. Porosity and Water content Measurments by Water Immersion. Research Report No. YKI 701/97, Technical Research Centre of Finland (VTT), Espoo, Finland, 29 p.

Pollock, A. 1989. Acoustic Emission Inspection. Metals Handbook 9th edition, Vol. 17, ASM international. pp 278-294.

Read, R. & Martino B. 1996. Effect of Thermal Stresses on Progressive Rock Failure at AECL's Underground Research Laboratory. Proc. Int. Conf. on Deep Geological Disposal of Radioactive Waste, Sept. 16-19, 1996, Winnipeg, Canada. Canadian Nuclear Society, Toronto, Canada, pp. 7-43 – 7-53.

Salminen, P. & Viitala, R. 1985. Rock Drillability Study. Technical Report 1985/1. Helsinki University of Technology, Laboratory of Mining Engineering, Espoo.

Zalesski, B. V. 1964. Physical and mechanical properties of Rocks. Academy of Sciences of the USSR, Institute of geology and Ore Deposits, Petrography, Mineralogy and Geochemistry. Moskau. Translated from Russian by Israel program for Scientific Translations, IPTS Cat. No. 1858.

Äikäs, K. & Sacklén, N. 1993. Fracture mapping in the Research Tunnel. Work Report 93-01, Teollisuuden Voima Oy, TVO/Research Tunnel, Helsinki.